Master Thesis

Czech
Technical
University
in Prague

F4

Faculty of Nuclear Sciences and Physical Engineering
Department of Physics

L-H transition in tokamak plasma: study of local parameters in the edge plasma

Bc. Ondřej Grover

Supervisor: Ing. Martin Hron, Ph.D.
Field of study: Physics and Thermonuclear Fusion Technology
May 2017

ČESKÉ VYSOKÉ UČENÍ TECHNICKÉ V PRAZE
FAKULTA JADERNÁ A FYZIKÁLNĚ INŽENÝRSKÁ
PRAHA 1 - STARÉ MĚSTO, BŘEHOVÁ 7 - PSČ 115 19

Katedra: fyz *Akademický rok:* 2016/2017

ZADÁNÍ DIPLOMOVÉ PRÁCE

Student: Bc. Ondřej Grover

Studijní program: Aplikace přírodních věd

Obor: Fyzika a technika termojaderné fúze

Název práce: (česky) L-H přechod v tokamakovém plazmatu: studium lokálních parametrů okrajového plazmatu

Název práce: (anglicky) L-H transition in tokamak plasma: study of local parameters in the edge plasma

Pokyny pro vypracování:

Zaměřte se na charakterizaci vybraných lokálních parametrů okrajového plazmatu tokamaku COMPASS, u nichž se předpokládá možná souvislost s L-H přechodem - zonální toky a jejich předpovídaný hnací mechanismus, Reynoldsovo napětí (Reynolds stress).

1. Pomocí sondové hlavice na měření Reynoldsova napětí (RS sonda) proveďte měření v plazmatu v blízkosti L-H přechodu, které vykazuje charakteristiky tzv. I-fáze pozorované na tokamaku ASDEX-Upgrade [1]

2. Charakterizujte fázový posun mezi intenzitou radiálního elektrického pole a fluktuací elektronové hustoty; ověřte, zda pozorované oscilace vykazují charakter tzv. limitních cyklových oscilací (LCO) známých z tokamaků ASDEX-Upgrade a HL-2A [2].

3. Srovnejte profil Reynoldsova napětí získaného a základě dat z Langmuirových sond a z ball-pen sond [3] a diskutujte vliv fluktuací elektronové teploty.

4. Zaměřte se na hledání stacionárních struktur (na škále cca 1 cm) na radiálním profilu elektrického pole (ev. dalších veličin měřených RS sondou), o nichž se předpokládá, že mají souvislost s přítomností zonálních toků [4].

Doporučená literatura:

[1] G. Birkenmeier, et al.: Magnetic structure and frequency scaling of limit-cycle oscillations close to L- to H-mode transitions, Nuclear Fusion 56 086009 (2016)

[2] Y. Xu, et al.: Dynamics of low–intermediate–high-confinement transitions in the HL-2A tokamak, Plasma Phys. Control. Fusion 57 014028 (2015)

[3] J. Adámek, et al.: A novel approach to direct measurement of the plasma potential, Czechoslovak Journal of Physics 54:C95-C99 (2004)

[4] J. C. Hillesheim, et al.: Stationary Zonal Flows during the Formation of the Edge Transport Barrier in the JET Tokamak, Phys. Rev. Lett. 116 065002 (2016)

Jméno a pracoviště vedoucího diplomové práce:

Ing. Martin Hron, Ph.D., pracoviště Tokamak, Ústav fyziky plazmatu, AV ČR, v.v.i.

Datum zadání diplomové práce: 20.10.2016

Termín odevzdání diplomové práce: 05.05.2017

Doba platnosti zadání je dva roky od data zadání.

……………………………………..
vedoucí katedry

………………………………..
děkan

V Praze dne 20.10.2016

Acknowledgements

I would like to thank my supervisor Ing. Martin Hron, Ph.D. for his unending patience, cheerful support and helpful discussions and suggestions; Mgr. Jakub Seidl, Ph.D. for the supervision and support during the LCO campaigns and interesting discussions about data analysis methods and plasma turbulence; Mgr. Jiří Adámek, Ph.D. for the productive discussions about the probe head design and positive support during the article submission process and finally the whole COMPASS team, especially operators and technicians, for the barrier-breaking dedication to the experiment and diagnostics design, preparation and maintenance.

This work was supported by the Czech Science Foundation Project No. GA16-25074S and by the Grant Agency of the Czech Technical University in Prague, grant No. SGS15/164/OHK4/2T/14, Research of the Magnetic Field Confinement in Tokamak.

Prohlášení

Prohlašuji, že jsem svou diplomovou práci vypracoval samostatně a použil jsem pouze podklady (literaturu, projekty, SW, atd.) uvedené v přiloženém seznamu.

Nemám závažný důvod proti použití tohoto školního díla ve smyslu § 60 Zákona č. 121/2000 Sb., o právu autorském, o právech souvisejících s právem autorským a o změně některých zákonů (autorský zákon).

V Praze dne

Abstract

Oscillations during the L-H transition from the low to high confinement modes and Reynolds stress profiles were investigates using two multi-pin probe heads designed and used on the COMPASS tokamak. The probe heads consisting of both Langmuir and ball-pen probes enable fast, simultaneous measurements of the radial and poloidal electric fields with either probe type and the electron temperature up to several mm inside the last closed flux surface. The radial Reynoldss stress profiles show a significant impact of the electron temperature fluctuations on the Langmuir probe measurements in comparison to the ball-pen probe measurements. The oscillations during the L-H transition were identified through probe measurements as type-J limit cycle oscillations during which the turbulence intensity grows after the velocity shear driven by the pressure gradient decreases. The oscillations were found to be different from edge-localized modes (ELM).

Keywords: COMPASS tokamak, L-H transition, ball-pen probe, Reynolds stress, limit cycle oscillations

Supervisor: Ing. Martin Hron, Ph.D.
Tokamak department
Institute of Plasma Physics of the Czech Academy of sciences

Abstrakt

Oscilace v průběhu L-H přechodu z módu nízkého do vysokého udržení a profily Reynoldsova napětí byly zkoumány pomocí dvou mnoho-hrotových sondových hlavic navrhnutých a použitých na tokamaku COMPASS. Tyto sondové hlavice obsahující Langmuirovy i ball-pen sondy umožnují rychlé, současné měření radiálních a poloidálních elektrických polí oběma typy sond a elektronové teploty až 5 mm uvnitř posledního uzavřeného povrchu. Na radiálních profilech Reynoldsova napětí byl nalezen významný vliv fluktuací elektronové teploty na meření s Langmuirovými sondami v provnání s ball-pen sondami. Oscilace během L-H přechodu byly identifokovány sondovými měřeními jako limitní cykolvé oscilace typu J, během kterých intenzita turbulence roste po snížení střihu rychlosti hnané gradientem tlaku. Tyto oscilace byly odlišeny od nestabilit lokalizovaných na okraji (ELM).

Klíčová slova: tokamak COMPASS, L-H přechod, ball-pen sonda, Reynoldsovo napětí, limitní cyklové oscilace

Překlad názvu: L-H přechod v tokamakovém plazmatu: studium lokálních parametrů okrajového plazmatu

Contents

Introduction

The transition from the low to high confinement regime (L-H transition) in tokamaks is a key area of active research highly relevant for the success of the ITER tokamak and other future machines. Even though most currently active tokamaks routinely operate in the high confinement mode (H-mode), a robust and fully predictive theory of the L-H transition remains elusive.

One promising model of the L-H transition is the predator-prey model where shearing zonal (small radial scale) poloidal flows (predator) decorrelate turbulence (prey) to such an extent until the pressure gradient in the state of partially reduced turbulence grows to levels sufficient to decorrelate turbulent structures itself and creates a transport barrier at the plasma edge which results in the high confinement mode. However, the precise interaction between the turbulence, zonal flows and mean flows is still not known and is being actively investigated. Of particular interest is the role of the Reynolds stress force related to the Reynolds stress tensor through which the turbulent structures are predicted to drive the zonal flows. Since the zonal flows are damped by secondary instabilities, this interaction can lead to so called limit cycle oscillations between states of fully developed turbulence in which the zonal flows begin to grow and states of turbulence partially suppressed by zonal flows after which the zonal flows are damped in the absence of turbulence and turbulence can develop again.

One common method of measuring the Reynolds stress tensor is to measure fluctuations of electric fields with arrays of Langmuir probes. However, such measurements may be influenced by the fluctuations of the electron temperature. Similar probe head arrangements have been also used to investigate the dynamics of density fluctuations and electric fields during limit cycle oscillations. For these reasons, two similar probe heads equipped with both Langmuir and ball-pen electrostatic probes were designed, constructed and used in the scope of this thesis. The fast, simultaneous measurement of floating voltages by Langmuir and ball-pen probes enables the estimation of electric fields and the electron temperature on a fast time scale. The purpose of these probe heads was to investigate the role of temperature fluctuations on the measurement of the Reynolds stress tensor and to investigate oscillations observed during the L-H transition on the COMPASS tokamak which are suspected of being limit cycle oscillations. This thesis reports on the results of these measurements and their analysis.

This thesis is split in two parts: Part I describes the theoretical and experimental background for the performed measurements. Part II presents results from the performed measurements and their analysis. In chapter 1 the tokamak is introduced in the wider scope of thermonuclear fusion and important tokamak terminology and coordinate systems relevant to this thesis are briefly described. Chapter 2 explains the predator-prey model of the L-H transition in the framework of electrostatic turbulence and shearing poloidal flows and introduces important quantities, such as the Reynolds stress tensor and drift velocities. Chapter 3 describes the experimental setup of the COMPASS tokamak and focuses in detail on electrostatic Langmuir and ball-pen probes and their arrangement on the probe heads mentioned above. Chapter 4 begins Part II and presents the measurement properties of the probe heads and compares them with other diagnostics. In chapter 5 the influence of electron temperature on the Reynolds stress tensor is described. Chapter 6 presents the results of the investigations of the oscillations during the L-H transition. Chapter 7 briefly summarizes the progress in the search for stationary zonal flow structures.

Part I

Theoretical and experimental background

Chapter 1
Tokamak

The tokamak is currently the most advanced and most successful configuration in magnetically confined fusion experiments in terms of the obtained fusion power output and the $n\tau_E$ product [1]. All the experiments in this thesis were performed in a tokamak device, and therefore this chapter serves as an introduction of this configuration and contains definitions of important terminology and quantities used throughout the thesis.

First, the relevance of the L-H transition and tokamaks is established within the broad scope of thermonuclear fusion in section 1.1. Then the topology and generation of magnetic fields in a tokamak are described in section 1.2 and finally the coordinate systems used in this thesis are explained in section 1.3.

1.1 Thermonuclear fusion reactor

The literature on thermonuclear fusion is vast and plentiful [1, 2, 3, 4, 5, 6, 7] and a full and comprehensive summary is beyond the scope of this thesis. Therefore, this section will only summarize the motivation for the research in the topic of the L-H transition in tokamaks within the wider scope of thermonuclear fusion.

The search for new ever cheaper, more secure and universally accessible energy sources is driven by several factors, including but not limited to: The steadily rising energy demands of the human civilization, the finiteness of currently known energy resources and reserves in the face of the rising energy demands, the maintenance and investment costs of current energy sources and last but not least the various environmental and socio-economic impacts of usage of different energy sources. Controlled thermonuclear fusion promises to be one such energy source in the future, because the fuel – water and lithium in the simple case – is abundant, there is no risk of an uncontrollable explosion when confinement is lost and only very little hazardous and environmentally undesirable waste. These have been the primary motivations for research in this field for the last ~ 65 years.

Over the second half of the 20$^{\text{th}}$ century many different nuclear fusion reactor configurations and devices have been constructed and tested. Their goal was to confine the fuel at a sufficiently high density and temperature for a sufficient period of time for the nuclear fusion reactions to produce enough power to surpass the power needed to heat the fuel to the extreme temperatures, leading to so called “ignition”. Almost all the experiments focused on the fusion of hydrogen isotopes of deuterium and tritium, because their fusion reaction has a very high cross-section at temperatures in the range of tens of keV, whereas other nuclear fusion reactions typically have smaller maximum cross-sections at higher temperatures [1]. Furthermore, deuterium can be separated from abundant water and tritium, although toxic and radioactive, can be produced on-site from lithium. Such high temperatures of the whole fuel corresponding to 100×10^6 K are necessary to overcome the Coulomb barrier between nuclei to be fused. At such high temperatures the fuel is in the state of matter known as plasma, and therefore the field of thermonuclear fusion is traditionally closely tied with plasma physics.

The conditions necessary for achieving “ignition” can be summarized for a simplified case as the Lawson criterion which states that for a given temperature the product of the plasma density n and the energy confinement time τ_E must be higher than a function dependent on temperature. The energy confinement time is the characteristic time scale at which plasma energy W would be depleted by losses characterized by the loss power P_L in the absence of any input power: $\tau = \frac{W}{P_L}$.

In the past decades only several of the tested confinement devices concepts have managed to steadily progress towards the necessary $n\tau_E$ values. These different concepts have opted to optimize either one of the terms in the product. The inertial confinement fusion concept attempts to achieve high densities in the order of $n \sim 1 \times 10^{31}\,\mathrm{m}^{-3}$ by compressing the fuel by laser or laser-induced or particle-beam-induced radiation, while the confinement time is very small and only the inertia of the fuel itself “confines” it for a very short time. The magnetic confinement fusion went the other way and opted to achieve confinement time in the order of $\tau \sim 1\,\mathrm{s}$ at modest maximum densities $n \sim 1 \times 10^{20}\,\mathrm{m}^{-3}$ due to stability issues. The fuel is confined by electromagnetic fields which can entrap particles on long periodic orbits leading to a high value of τ_E. Various magnetic and electric field topologies have been tested in the past and the most promising and most widely used are toroidal topologies. The most successful devices with such topology have been tokamaks and stellarators. However, he progress of tokamaks in achieving higher $n\tau_E$ products has surpassed that of stellarators, mostly due to the simpler construction of tokamaks in comparison with stellarators and the optimization of complicated helical magnetic fields in stellarators. The recently completed Wendelstein 7-X stellarator [8] has the potential to make the stellarator concept catch up with tokamak performance.

The most successful tokamak experiment to date is the Joint European Torus (JET) in the United Kingdom which achieved a fusion gain ratio Q of the fusion power output to the heating power input close to 0.6 in 1997 [5]. Nevertheless, the achievement of break-even $Q > 1$ remains the goal of the ITER tokamak currently being constructed in France. The ITER tokamak will be the largest tokamak to have been ever built and should achieve at least $Q = 10$. And here lies the crucial role of the L-H (low to high confinement mode) transition described in greater detail in chapter 2 for the success of ITER: It must operate in the high confinement mode where τ_E is doubled in comparison to the standard low confinement regime in order to achieve at least $\tau_E = 3.7\,\mathrm{s}$. However, it was designed based on fitted scaling laws extrapolated from smaller machines and the achievement of the high confinement mode is not guaranteed. Therefore a better understanding of the L-H transition may open doors to even better confinement modes in future machines.

Altogether, a thorough understanding of the L-H transition is a key element for the success of magnetically confined thermonuclear fusion in tokamaks. Even though there have been many delays in milestones set for ITER and future demonstration power plant rectors DEMO in compariosn to the original European fusion roadmap [9], the ITER project continues to make progress steadily and the tokamak concept remains the most likely candidate for the future nuclear fusion power plant.

1.2 Magnetic field topology in a tokamak

A tokamak configuration shown schematically in Figure 1.1 consists of three main magnetic field generation coil systems: The toroidal and poloidal field coils and the central solenoid. The toroidal field coils enclose the torus-shaped vacuum vessel (chamber) and produce a so called toroidal magnetic field $\vec{B}_\phi$. Its field lines are concentric circles with their centers on the central tokamak axis. The toroidal direction of the $\vec{B}_\phi$ field within the vessel torus gives rise to the toroidal angle ϕ. This then leads to a natural definition of a cylindrical coordinate system (R, Z, ϕ) with the central axis serving as the axis of the system. In tokamaks, B_ϕ is typically quite strong, usually in the order of a few tesla $B_\phi \sim 1 \times 10^1\,\mathrm{T}$. Due to the toroidal field coils being closer to each other in the region closer to the central axis the strength of the toroidal magnetic field has the following dependence [1] within the torus enclosed by the coils

$$B_\phi \propto \frac{1}{R} \tag{1.1}$$

For this reason the region close to the central axis has a higher toroidal field and is called the high field side (HFS) and the region on the opposite edges of the vessel further away from the central axis is called the low field side (LFS).

The central solenoid is used to induce (at least in the initial stages of a discharge) a current in the plasma I_{pl} contained in the vessel. The net current flows also in the toroidal direction (possibly counter to the direction of $\vec{B}_\phi$) and through Ampere's law gives rise to a poloidal magnetic field $\vec{B}_p$ encircling the current flow. The superposition of the toroidal and poloidal magnetic field results in total a helical magnetic field which stabilizes the plasma against instabilities driven by the radially inhomogeneous magnetic field as further discussed in section 2.2.

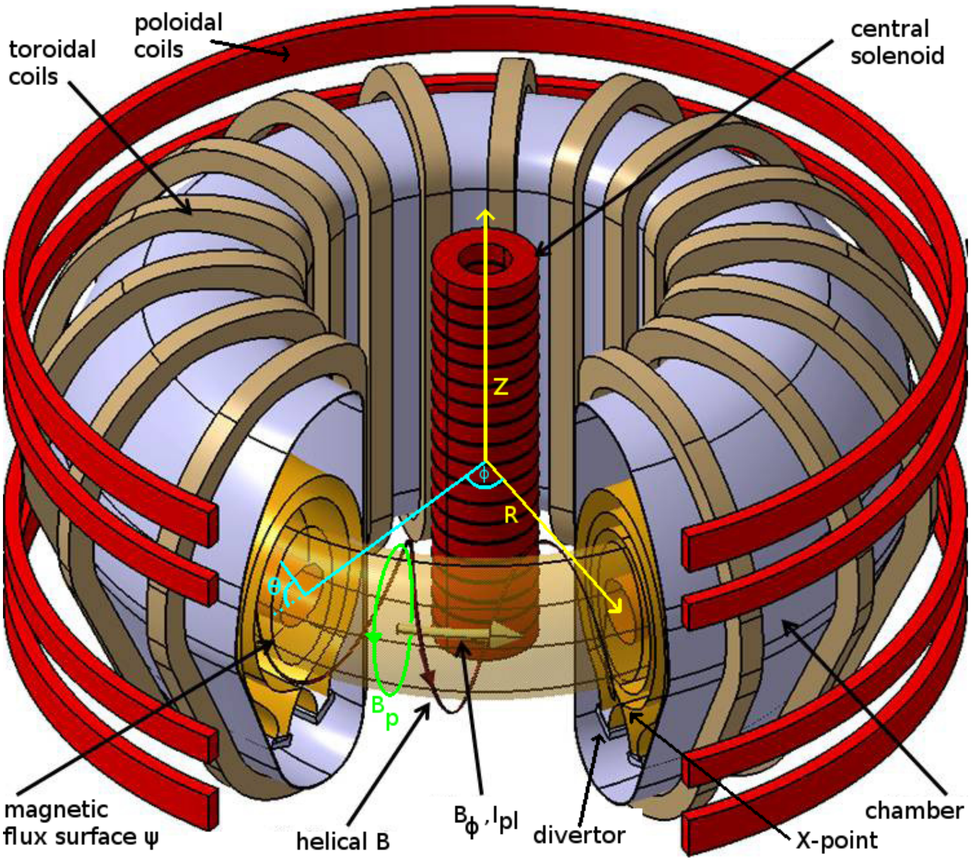

Figure 1.1: Schema of a tokamak configuration with labeled magnetic coil systems and magnetic field lines and topology. Reproduced from [5] and edited.

The magnetic field lines form magnetic flux surfaces as shown in Figure 1.1. Under the assumption of axis-symmetry (symmetry about the central axis) where quantities are independent of ϕ it is convenient to define the poloidal magnetic flux function $\psi(R, Z)$ of the flow of the poloidal magnetic field $\vec{B}_p$ through a surface perpendicular to it

$$\psi(R, Z) = \frac{1}{2\pi} \int \vec{B}_p \cdot \mathrm{d}\vec{S} \tag{1.2}$$

The factor 2π is not always used, but it will be assumed further on unless stated otherwise. ψ is constant on a magnetic surface and thus is used to label the flux surfaces.

The additional poloidal field coils are used for generating external magnetic fields which are added to $\vec{B}_p$ and thus are used for stabilizing or elongating the plasma into a requested shape at a requested position. In fact, a certain external vertical magnetic field is always necessary to balance the expansion of plasma caused by the larger surface on the LFS. This leads to the magnetic surfaces being closer to each other on the LFS in comparison to the HFS, a phenomenon known as the Shafranov shift.

A special poloidal field coil is often put below the plasma and a current of a similar strengths as I_{pl} is driven in the same direction which cancels out B_p at a given point called the X-point. The flux surface in which the X-point lies is called the last closed flux surface (LCFS) or separatrix, because inside this flux surface all field lines are closed within the vessel. Outside the LCFS the field lines are not closed within the vessel and intersect the wall of the vessel near the coil used to create the X-point, i.e. they are diverted towards the so called divertor plates. These field lines are often called "open field lines", even though they close outside the vessel since they too must satisfy $\mathrm{div}\vec{B} = 0$. This so called divertor configuration leads to a greater isolation of the closed magnetic surfaces confining the core plasma from material surfaces of the vessel in comparison to only limiting the material surface interaction by a poloidal or toroidal limiter as is done in the early stages of a discharge. The region of flux surfaces with open field lines is called the scrape-off-layer (SOL). The SOL together with a narrow region of flux surfaces just inside the LCFS comprises the so called edge region of the plasma.

1.3 Used coordinate systems

There are various coordinate systems used for describing a position in a tokamak configuration, each having different use cases according to the advantages or disadvantages of the given coordinate system.

For describing positions of diagnostics and measurements in the machine a simple cylindrical system (R, Z, ϕ) mentioned in the previous chapter is most often used as it is independent of the magnetic field topology and can be used directly in the laboratory frame. Here, R is the radial distance (radius) from the central axis (axis of the central solenoid), Z is the vertical distance from the midplane which is usually located close to the plane of symmetry between the top and bottom parts of the machine. The toroidal angle ϕ specifies a given (R, Z) half-plane (bounded by the axis of the central solenoid) called the poloidal cross-section. If a given quantity is assumed to be independent of ϕ, it is called axisymmetric as it is symmetric about the central axis.

If the magnetic topology is known and the location of the magnetic axis (where $B_p = 0$) is at a given radius $R = R_0$ and height $Z = Z_0$, a coordinate system with the same toroidal angle ϕ and a local polar-like coordinate system (r, θ) centered at $[R_0, Z_0]$ for a half-plane given by ϕ can be used. In this case, the radius r is also called the radial coordinate, but its lower case indicates it is tied to the magnetic axis. The angle θ is called the poloidal angle. However, this poloidal angle corresponds well to the direction of the poloidal magnetic field $\vec{B}_p$ only for configurations with a circular plasma cross-section. It is also only in these configurations that the radius r remains constant on a flux surface which also justifies the interpretation of quantities assumed to depend only on r as so called radial profiles. Nevertheless, the terminology of the radial and poloidal direction remains widely used even in plasmas with a non-circular cross-section. In these cases "radial" usually refers to the direction from the plasma core towards the edge and poloidal generally to the direction of the $\vec{B}_p$ field. Another term connected to simple circular cross-sections is the major and minor vacuum vessel radius. The major radius R is usually close to the magnetic axis radius, but is fixed with respect to the vacuum vessel. The minor radius a in a circular cross-section vacuum vessel is the r-like radius at which the vacuum vessel is located if $R = R_0$. However, modern tokamak configurations have a D-like vessel cross-section which enables plasma configurations with an elongated cross-section. In this case, usually either two values of a are given, one for the top vessel wall and one on the midplane, or an average value is given.

To accommodate non-circular plasma cross-sections the radial coordinate r is usually replaced by the poloidal magnetic flux function ψ which labels each magnetic flux surface. This gives better foundations for calculating profiles $q(\psi)$ of quantities q assumed to be constant on a flux surface. However, such profiles are usually still called "radial" profiles. Instead of the raw flux function ψ a normalized version ψ_n is often used with $\psi_n = 1$ fixed at the LCFS. This also enables the comparison of profiles between devices with different sizes and field strengths.

In simplified theoretical considerations often a so called plasma slab geometry is used where the (r, θ, ϕ) system is locally "unraveled" into corresponding Cartesian coordinates (x, y, z). This transformation makes sense only locally for a small region of the plasma. It is often used for simplified fluid calculations of plasma turbulence or for reasonably small diagnostics.

The coordinate systems described above are used most often in experimental work on tokamaks, but there exist many other systems used primarily in theoretical works where such systems may have useful properties, e.g. the magnetic field lines are straight, or more general systems used in non-axisymmetric configurations, e.g. stellarators. However, in this thesis only the coordinate systems described above in detail will be used.

Chapter 2

Theory of the L-H transition

From a theoretical perspective the L-H transition from a mode of low to high confinement is a dynamic process leading to the quenching of turbulent transport. There are two ways to perceive such a process:

- A physical mechanism destroys/decorrelates the turbulent structures, thereby preventing them to contribute to radial cross-field transport
- Energy is transferred from the turbulent processes to some energy sink

While both perceptions describe the same process and are equivalent, each offers different insights into the dynamics of the process which merits a study of both. The likely energy sink and physical mechanism decorrelating turbulent structures is considered to be sheared poloidal flows.

In order to present a clear model of the L-H transition process, first, the high confinement mode (H-mode) is briefly described in section 2.1 in order to present the motivation for the study of the L-H transition and to describe the properties of the end state to which the L-H transition leads. In section 2.2 the characteristics of turbulence and the basis of electrostatic treatment of plasma turbulence theory in the plasma edge are presented. Then the properties and possible generation mechanisms of sheared poloidal flows are discussed in section 2.3. Finally, the interaction between the turbulence and sheared flows is described by a predator-prey-like model of the L-H transition in section 2.4.

2.1 H-mode

One of the early lures of tokamaks was the predicted scaling of the cross-field diffusion coefficient D with the strength of the magnetic field B as $D \sim \frac{1}{B^2}$ which suggested that a strong magnetic field will greatly reduce cross-field transport flow $\Gamma = -D\nabla n$ which should lead to a long confinement time τ_E as suggested even by a simple random walk argument $D \sim \frac{l^2}{\tau_E}$ where l is a characteristic mean free path of particle motions across the magnetic field lines.

However, experiments showed that the diffusion coefficient scaled only as $\sim \frac{1}{B}$ (Bohm scaling) and the high diffusion coefficients $D \approx 1\,\mathrm{m}^2/\mathrm{s}$ were several orders of magnitude higher than even those predicted by neoclassical theory which attempted to explain the enhanced transport through additional effects like particle trapping on banana orbits. Therefore, this enhanced transport was initially called anomalous. Later it was discovered that the enhanced transport is caused by turbulent structures which transport plasma radially outwards much faster than other effects. Therefore, the diffusion-based model of cross-field transport became less descriptive as turbulent structures lead to intermittent transport with no clear characteristic mean free path. Furthermore, the scaling of confinement time with heating power input promised a pessimistic outlook due to the confinement time deteriorating with heating power.

And then in the year 1982 the High confinement mode (H-mode) was unexpectedly discovered on the ASDEX tokamak while testing neutral beam injectors and increasing the heating power [10]. The H-mode is characteristic by a nearly sudden quenching of turbulence transport in the edge plasma leading to a roughly double confinement time. This also leads to a lower level of recycling of neutrals from the vessel wall which is observed as a sudden drop in the intensity of light emission on the H_α spectral line from the edge plasma as can be seen in Figure 2.1. Subsequently the mode of confinement preceding the H-mode has become known as the Low confinement mode (L-mode) in which enhanced turbulent transport dominates on the edge and the transition from low to high confinement as the L-H transition. The quenching of turbulent transport is understood to be caused by a formation of an edge transport barrier just inside the separatrix. This leads to steep pressure gradients across the barrier which shifts the pressure profile inside the barrier upwards which is referred to as "a pedestal forming" upon which the pressure profile is "placed" as shown in Figure 2.1. This enhanced pressure profile also means that the ratio between the plasma pressure and the magnetic pressure exerted by the poloidal field on the plasma known as the poloidal beta $\beta_p = \frac{\langle p \rangle}{\langle B_p^2 \rangle}$ also increases, often by a factor of 2-3.

However, the H-mode also has some disadvantages. If the transport barrier is maintained for a longer duration, impurities may accumulate in the plasma core as they cannot escape across the edge barrier and may lead to large radiation energy losses and possibly disruptions. Under certain conditions the transport barrier may quasi-periodically collapse due to an instability called edge-localized mode (ELM). Such modes may carry away a significant amount of the energy contained by the transport barrier, and therefore are of great concern since their interaction with plasma facing components (PFC) may lead to their melting. The collapse of the transport barrier and the subsequent release of hot plasma on the vessel wall leads to a surge in the recycling of neutrals from the wall which is observable as spikes in the light emission from the edge plasma.

Since its discovery, many tokamaks have achieved the H-mode, including the COMPASS tokamak [12], but so far the exact conditions under which the L-H transition occurs and their theoretical understanding is incomplete. The L-H transition is known to spontaneously occur when the input heating power

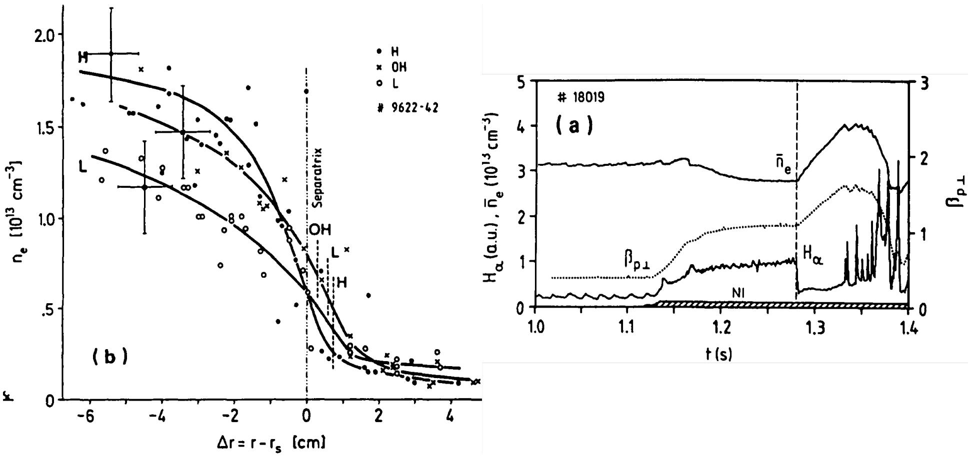

Figure 2.1: *Left:* Typical density profiles in L-mode and H-mode on ASDEX. The H-mode profile exhibits a steep gradient just inside the separatrix in comparison to the L-mode profile which leads to the H-mode profile being shifted upwards (the "pedestal") in the core. Reproduced from [11]. *Right:* Typical time evolution of quantities like the light emission on the spectral H_α line from the edge plasma and β_p during the L-H transition. A visible drop in the H_α emission intensity is seen which indicates the onset of the H-mode. Later, spikes in the signal indicate ELMs which temporarily increase the neutral recycling from the wall. Reproduced from [10].

exceeds some threshold power level P_{LH} which strongly depends on many parameters like the type of the working gas, density, the shape and position of the plasma including the position of the X-point, etc. Large databases of H-mode experiments were compiled and scaling laws were developed for the P_{LH} threshold which are expressions describing the dependence of P_{LH} on the various parameters which varied between the different experiments. These scaling laws were then used to extrapolate P_{LH} and the necessary heating power for future reactors like ITER and DEMO. However, these scaling laws often do not fully capture the more complicated dependence on parameters, e.g. the existence of a minimum threshold power with respect to the plasma density. The ITER design was based on the IPB-98 scaling [7], but since then many other experiments have been conducted and more rigorous analysis of the compiled databases [13] hint that the extrapolated ITER threshold power may be different from the original values used in the ITER design. This is one of the primary motivations for the detailed investigation of the L-H transition which is hoped to lead to its better theoretical understanding and improved control of the transition and quenching of edge turbulence.

2.2 Turbulence in the edge plasma

In the following an overview of the turbulence characteristics and terminology relevant to the results in this thesis is given. The description of turbulence given here is based on a simplified MHD electron and ion fluid electrostatic treatment of turbulence as presented in [14, 4] and neglects more complicated phenomena like electromagnetic turbulence due to magnetic field fluctuations and kinetic effects.

The quasi-neutrality of the plasma $n = Zn_i = n_e$ will be assumed with Ze being the ion charge for Z-times ionized atoms, n_i and n_e the ion and electron densities, respectively. In formulas generalized for both species the subscript α will refer to the particle species i or e and q_α to the particle species charge.

The density of the fluids are governed by the density continuity equation

$$\frac{\partial n}{\partial t} + \nabla(n\vec{v}_\alpha) = 0 \tag{2.1}$$

which can be rewritten in a conservative form by applying the product rule to the divergence of the density flow $n\vec{v}_\alpha$ representing advection of the fluid by the velocity

$$\frac{\partial n}{\partial t} + \vec{v}_\alpha \cdot \nabla n = \frac{\mathrm{d}n}{\mathrm{d}t} = -n\nabla\vec{v}_\alpha \tag{2.2}$$

where $\frac{\mathrm{d}}{\mathrm{d}t}$ is the total (or hydrodynamic) time derivative related to the local change in time $\frac{\partial}{\partial t}$ and the change brought by the flow of the fluid $\vec{v}_\alpha \cdot \nabla$, i.e. the advective part of the hydrodynamic derivative. It follows that the fluid is incompressible (the density does not locally change $\frac{\mathrm{d}n}{\mathrm{d}t} = 0$) if the fluid velocity has no divergence $\nabla\vec{v}_\alpha = 0$, i.e. there are no sinks or sources of the fluid velocity. The compressibility of the fluid velocity and the associated currents will play a major role further on.

Under the assumption of electrostatic turbulence in the edge plasma the most important quantities related to radial transport are fluctuations (denoted by a tilde) and background profiles (here denoted by a 0 subscript, i.e. they are considered zeroth order quantities) of the density $n = n_0 + \tilde{n}$ and the electrostatic plasma potential $\phi = \phi_0 + \tilde{\phi}$. The associated forces driving the turbulence are then given by the gradients of these quantities: The pressure gradient (since cold ions $T_i = 0$ and constant electron temperature T_e are assumed) $-T_e\nabla n$ and the electric field $\vec{E} = -\nabla\phi$. In the presence of an inhomogeneous background magnetic field $\vec{B} = \vec{B}_0$ with its curvature and decreasing strength related to (1.1) the turbulence may be also driven by the gradient of the magnetic field strength ∇B. The plasma potential and density is assumed to be smooth enough that partial derivatives are interchangeable.

In the following the dynamics will be described in a local slab geometry with the z-axis being co-linear with the background magnetic field $\vec{B} = B\vec{b} \propto \vec{z}$. The x and y axes correspond to the radial and poloidal direction, respectively.

The large magnetic field strength B is usually assumed to be constant or only slowly varying along the radial direction which is a reasonable approximation considering the strong toroidal magnetic field decreases on the scale of the machine size in the edge region on the LFS as given by (1.1). This results in the following turbulence description being strongly non-isotropic and two important directions arise: The direction parallel to the magnetic field (denoted by a $\parallel$ subscript) and the so called drift plane perpendicular to the magnetic field (denoted by a $\perp$ subscript) which is key to the cross-field transport.

Therefore, this treatment effectively reduces the 3D turbulence problem to 2D turbulence with additional parallel dynamics serving as corrections.

2.2.1 Important drift velocities

The drift plane leads to natural definitions of important drift velocities related to the forces mentioned above. These drift velocities contribute to the motions of the fluid in the drift plane described by the perpendicular velocity $\vec{v}_\perp$. The Navier-Stokes-like equation (where flow viscosity and collisional terms are neglected) governing the fluid flow velocities is

$$m_\alpha \frac{\mathrm{d}\vec{v}}{\mathrm{d}t} = -\frac{\nabla p_\alpha}{n} + q_\alpha \vec{E} + q_\alpha \vec{v}_\alpha \times \vec{B} \tag{2.3}$$

where the total time derivative of the flow inertia on the left-hand side balanced by the pressure gradient and the Lorenz force on the right-hand side. The various drift velocities can be formally derived by taking the cross product of the equation with $\times \frac{\vec{B}}{q_\alpha B^2}$ which results in $\vec{v}_\perp$ appearing in place of the last term with the magnetic field and all the other terms are the drifts corresponding to the change of inertia and pressure and plasma potential gradients, respectively. A more rigorous derivation is based on the averaging of the force balance equation for a single charged particle over its gyration period which leads to an equation for the velocity of the gyration guiding center and then again taking the cross product of the equation with $\times \frac{\vec{B}}{q_\alpha B^2}$ [15] to obtain the perpendicular component of that velocity. However, that approach will not recover the ∇p related drift as it is intrinsically a fluid-related phenomena. A brief overview of the most important drift velocities for the topic at hand and their properties follows.

The $E \times B$ drift velocity

The electric field force $q_\alpha \vec{E} = -q_\alpha \nabla \phi$ results in the so called $E \times B$ drift velocity

$$\vec{v}_E = \frac{\vec{E} \times \vec{B}}{B^2} = \frac{\vec{E} \times \vec{b}}{B} = \frac{\vec{b} \times \nabla \phi}{B} \tag{2.4}$$

Due to the absence of the charge or mass of either electrons or ions the $\vec{v}_E$ drift velocity is the same for both particle species and moves the plasma as a whole. This also results in a zero contribution to the electric current density $\vec{j}_E = Zen\vec{v}_E - Zen\vec{v}_E = 0$. In a homogeneous magnetic field $B = const$ the $\vec{v}_E$ drift is incompressible since $\nabla \cdot \vec{v}_E = 0$ due to the assumed smoothness of the plasma potential $\partial_x \partial_y \phi = \partial_y \partial_y \phi$.

In the simplified electrostatic treatment of turbulence $\vec{v}_E$ is considered the dominant velocity responsible for the advection of both fluids and hence only it is considered in the advective part of the hydrodynamic derivative $\vec{v}_E \cdot \nabla$.

Due to the orientation of $\vec{v}_E$ it represents the motion along the equipotential contours of $\phi = const$. This also means that a symmetric (e.g. 2D Gaussian) perturbation in the (x,y) plane will result in a circular $\vec{v}_E$ motion around this perturbation as shown in Figure 2.2 where an eddy (or velocity vortex) is formed around the perturbation. This leads to a natural definition of the vorticity of the fluid flow $\vec{\Omega} = \nabla \times \vec{v}$. In the electrostatic treatment only $\vec{v}_E$ is considered as the main contributor to vorticity, therefore, only the z-component of vorticity is considered. The vorticity is then defined as $\Omega_z = \Omega = \frac{\nabla_\perp^2 \phi}{B}$. Since the inverse perpendicular scale of change of the gradient is expected to be significantly larger than that of the change of the inverse magnetic field strength ($k_\perp >> k_\parallel$), the term proportional to $\nabla \frac{1}{B}$ is neglected in comparison to the $\nabla_\perp^2 \phi$ term.

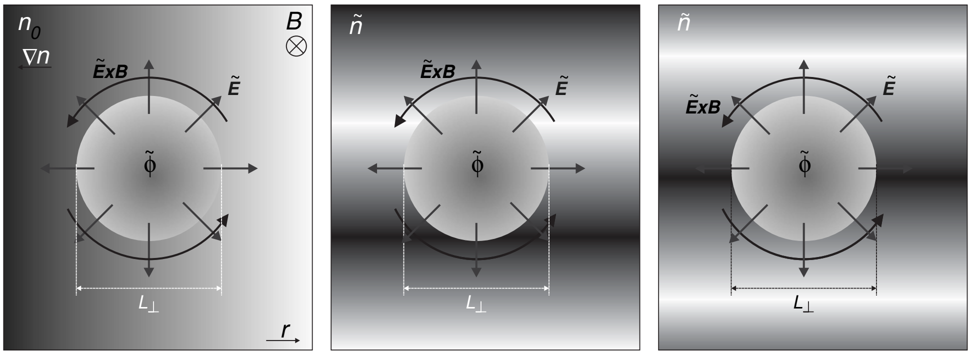

Figure 2.2: Reaction of a plasma with a background radial density gradient ∇n_0 to a symmetric plasma potential perturbation $\tilde{\phi}$. In the first picture the $E \times B$ drift creates an eddy around the $\tilde{\phi}$ perturbation which advects less dense (lighter) plasma to the left at the top and the more dense (darker) plasma to the right at the bottom. This leads to an out-of-phase density perturbation $\tilde{n}$ in the poloidal direction in the second picture. The electrostatic eddy then advects denser plasma at the bottom to the right and less dense at the bottom, resulting in net radial transport outwards. The third picture shows that if the perturbations are in phase in the poloidal direction, they do not result in net radial transport as the same density is advected at the top and bottom. Reproduced from [14].

Figure 2.2 also shows that the cross-phase between the density and potential perturbations determines the net radial transport. Quantitatively, the net radial transport due to such an eddy $\Gamma_r = \langle \tilde{n} \tilde{v}_{E,r} \rangle$ depends on the cross-phase $\Delta\varphi$ as $\Gamma_r \propto \sin(\Delta\varphi)$. Therefore, the net radial transport due to such eddies is most efficient when $\Delta\varphi = \frac{\pi}{2}$ and vanishes for $\Delta\varphi = 0$.

The polarization drift velocity

Another drift velocity also related to the electric field is the polarization drift velocity $\vec{v}_P$ which is caused by a time-varying electric field

$$\vec{v}_{P\alpha} = \frac{m_\alpha}{q_\alpha B^2} \frac{\mathrm{d}\vec{E}}{\mathrm{d}t} \tag{2.5}$$

This drift velocity is related to the time derivative of the inertia term $\frac{\mathrm{d}\vec{v}}{\mathrm{d}t}$ in (2.3). Therefore, the drift related to this term would in general contain derivatives of all drift velocities. However, in this simplified electrostatic treatment only the derivative of $\vec{v}_E$ which results in $\vec{v}_P$ is considered. Due to the small electron mass $m_e << m_i$ their inertia is also small in comparison to the ions. Therefore, the electron polarization drift will be neglected in turbulence considerations $\vec{v}_{Pe} \approx 0$. The difference in masses also results in a non-zero contribution to the electric current density $\vec{j}_P = Zen\vec{v}_{Pi}$.

The diamagnetic drift velocity

The pressure gradient force term $\frac{-\nabla p}{n}$ in (2.3) results in the diamagnetic drift velocity

$$\vec{v}_{*\alpha} = \frac{\vec{B} \times \nabla p_\alpha}{q_\alpha n_\alpha B^2} \tag{2.6}$$

As $\vec{v}_{*\alpha}$ depends on the particle species pressure it does present a contribution to the electric current density $\vec{j}_* = Zen\vec{v}_{*i} - eZn\vec{v}_{*e} = \frac{\vec{B}\times\nabla(p_i+p_e)}{B^2}$ which is related to the gradient of the plasma pressure.

In the case of a homogeneous magnetic field and the pressure gradients being determined by the density gradient the advection term in (2.1) vanishes $\nabla(n\vec{v}_{*\alpha}) = 0$ due to the assumed smoothness of the density $\partial_x\partial_y n = \partial_y\partial_y n$.

The ∇B drift velocity and magnetic field inhomogeneity

As mentioned in the previous cases of drifts, a homogeneous magnetic field results in the incompressibility of some of the drifts or fluid advection by them. In the case of an inhomogeneous magnetic field, the terms related to the divergence of the drift velocities or the advection term will due to the product derivation rule result in a secondary term proportional to $\propto \nabla\frac{1}{B}$ while the first term will have the same properties as if $\vec{B}$ was homogeneous. This term will represent both the curvature and inhomogeneous strength of the magnetic field. In [16] this term is called the curvature operator $\mathcal{C}(f) = \nabla\left(\frac{1}{B}\right)\cdot\left(\vec{b}\times\nabla f\right)$. With this notation the advection term (neglecting the polarization drift) in (2.1) becomes

$$\nabla\left(n(\vec{v}_E + \vec{v}_{*\alpha})\right) = \vec{v}_E\cdot\nabla n + \mathcal{C}(\phi) + -\mathcal{C}(p_\alpha) \tag{2.7}$$

therefore, the advective part of the hydrodynamic derivative is still dominated by $\vec{v}_E$ and $v_{*\alpha}$ does not explicitly advect the fluid, however, the two additional terms represent a contribution to the advection due to the inhomogeneity of the magnetic field. This contribution could be also in part attributed to inhomogeneity drift velocity of particles

$$\vec{v}_{\nabla B} = \frac{1}{2}m_\alpha v_\perp^2\frac{\vec{b}\times\nabla B}{q_\alpha B^2} \tag{2.8}$$

which is also proportional to $\propto \nabla\frac{1}{B}$ and due to the dependence on the particle species mass and charge also results in a contribution to the electric current which is represented by the curvature operator in (2.7).

2.2.2 The vorticity equation

Under the assumption of quasi-neutrality $n = Zn_i = n_e$ the total divergence of the electric current density is zero $-\frac{\partial(Zen_i - en_e)}{\partial t} = \nabla\vec{j} = en\vec{v}_i - en\vec{v}_e = 0$ due to the conservation of the electric charge. By using the drift velocities as the perpendicular components of the velocities in the current divergence the perpendicular part of the divergence $\nabla_\perp\vec{j}_\perp$ leads to a balance of the polarization and diamagnetic currents with the parallel current component $\nabla\vec{j}_P + \nabla\vec{j}_* = -\nabla\vec{j}_\parallel$. The divergence in the $\nabla\vec{j}_P$ term passes into the time derivative of the electric field $\vec{E} = -\nabla\phi$ in (2.5) and results in a term with $\nabla_\perp^2\phi$ which can be rewritten as the total time derivative of the vorticity Ω. This results in the so called vorticity equation

$$m_i n\left(\frac{\partial\Omega}{\partial t} + \vec{v}_E\cdot\nabla\Omega\right) = -\nabla\vec{j}_* - \nabla\vec{j}_\parallel \tag{2.9}$$

which shows that vorticity is generated due to the compressibility of either the diamagnetic or parallel electric currents. Either term gives rise to a different kinds of turbulent mechanisms which generate an electrostatic eddy. The compressibility of either current is equivalent to charge separation in the corresponding direction indicated by the divergence component direction.

The nonlinear term $\vec{v}_E\cdot\nabla\Omega$ is quadratic in ϕ. If the potential is transformed into spatial modes $\phi(\vec{x}) = \sum_{\vec{k}}\hat{\phi}(\vec{k})\exp(i\vec{k}\cdot\vec{x})$ this quadratic term will become proportional to $\sum_{\vec{k}}\left(\sum_{\vec{k}'}\hat{\phi}(\vec{k}')\hat{\phi}(\vec{k}-\vec{k}')\right)\exp(i\vec{k}\vec{x})$. This means that the $\vec{k}$ mode is determined by the interaction with modes $\vec{k}'$ and $\vec{k}-\vec{k}'$. This nonlinear scheme is called a three-wave interaction and permits energy transfer between different scales.

This description of plasma turbulence is very similar to the vorticity equation used to describe 2D turbulence in an ideal (incompressible, inviscous) hydrodynamic fluid. For such turbulence a dual cascade of energy and potential enstrophy transfer in the wavenumber space between self-similar turbulent scales develops [17]. If energy is injected into the fluid at some wavenumber k related to the characteristic turbulent structure length scale $l = \frac{k}{2\pi}$, the bulk of the kinetic energy $\propto v^2$ is transferred to lower wave numbers which results in an inverse energy cascade in wavenumber space. However, the bulk of the potential enstrophy, which is the energy contained in the vorticity of the turbulent structures $\propto \Omega^2$, is transferred to larger wavenumbers where such small scales dissipate and this results in a forward potential enstrophy cascade in the wavenumber space. Therefore, it is expected that as the enstrophy transfers towards smaller structures, large eddies break up through a cascade into smaller and smaller eddies which eventually dissipate, while the kinetic energy transfers towards towards large scale structures, forming large-scale sheared flows in the fluid.

2.2.3 Important linear instabilities

Although the instabilities described in the following are linear in nature, the fully turbulent state retains their characteristics, such as the cross-phase between density and plasma potential fluctuations, if the driving mechanism remain the same as in the linear case [14]. The two important linear instabilities described below are the interchange and resistive drift wave instabilities related to the compressibility of the diamagnetic and parallel electric currents, respectively.

The interchange instability

The interchange instability is a Rayleigh-Taylor type instability which in general is driven by a pressure gradient ∇p which has an opposite direction in comparison to some force field [2]. In the case of the tokamak geometry, this force is taken to be the centrifugal and field inhomogeneity force due to the curvature of the magnetic field represented by the gradient of the magnetic field strength ∇B. The general Rayleigh-Taylor mechanism leads to flute-like filaments of dense plasma escaping radially outwards while they are replaced by less dense plasma.

In the vorticity-based description outlined above, the interchange instability develops as follows: First the compressibility of the diamagnetic current $\vec{j}_*$ results in a local separation of charges in the poloidal direction. The perturbation is homogeneous in the magnetic field direction, i.e. $k_\| = 0$ and $\nabla \vec{j}_\| = 0$. This creates two potential perturbations like those in Figure 2.2 below each other, one negative and the other positive, corresponding to the separated charges. These potential perturbations then result in $E \times B$ advection outwards of the plasma between the perturbations and advection inwards of the plasma at the top and bottom which leads to the characteristic mushroom-like structure. This bipolar structure called a “blob” then continues to propagate radially outwards while it is replaced by less dense and colder plasma referred to as “holes”. At the same time the structure is elongated in the magnetic field direction, forming filaments. The cross-phase between the plasma potential and density is $\frac{\pi}{2}$.

The interchange instability has been extensively studied with the ESEL fluid code [16] which is based on equations similar to (2.2) and (2.9) with additional source and sink and dissipation terms and also an additional temperature (heat) transport equation with the assumption of cold ions $T_i = 0$. A typical result from an ESEL simulation run is shown in Figure 2.3 which displays the density and potential structure of a blob as was described above.

The magnetic field gradient ∇B always points towards the center of the tokamak, whereas the pressure gradient ∇p points towards the plasma center. Therefore, the gradients have an opposite sign on the LFS and the same sign on the HFS. For this reason the interchange instability can develop in the LFS region but is stabilized in the HFS region. This also leads to the regions being called that of unfavorable and favorable curvature, respectively.

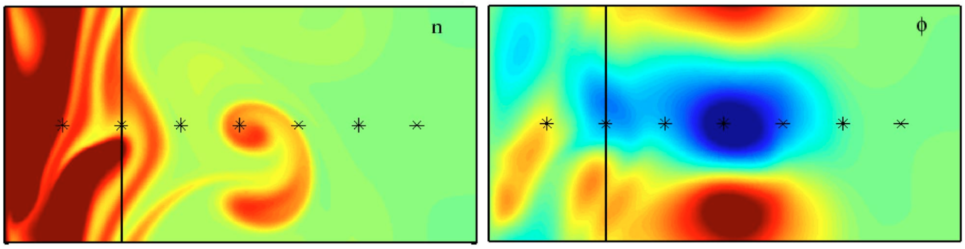

Figure 2.3: Example output of an ESEL simulation run. The x and y axes represent the radial and poloidal directions, respectively. The poloidal direction is periodic. The left picture shows the density n structure of a blob with the typical mushroom-like structure. The right picture shows the typical bipolar structure of the plasma potential ϕ in a blob structure. Reproduced from [16].

The turbulence intensity is greatly enhanced in a region of about 30° in the poloidal angle around the outer midplane on the LFS [18].

Drift wave instability

The drift wave instability is caused by the compressibility of the parallel current $\nabla \vec{j}_{\|}$. This implies that the modes have finite wavelength, or rather nonzero parallel wavenumber $k_{\|} > 0$. In general, this leads to the electrons being able to move along the magnetic field lines and establish a balance between density and electric potential perturbations [2]. A density (or more generally, pressure) perturbation on a background density gradient then leads to an electric potential perturbation due to the response of electrons. The motion of drift waves can be deduced from an assumed density perturbation of a wave-like pattern along the surface of the unperturbed density, i.e. the perturbation has a non-zero wavenumber perpendicular to a homogeneous magnetic field, usually along the poloidal direction while the background density gradient is in the radial direction. In the simple case with ideal plasma resistivity and no ion inertia (no polarization drift), an electric field perturbation would arise between regions with different densities in the parallel direction and the resulting poloidal $E \times B$ drift would propagate this drift wave density perturbation along the electric field direction with the diamagnetic drift velocity as the phase velocity and it would remain stable.

In the more complicated case of nonzero plasma resistivity $\eta > 0$ and ion inertia the drift wave becomes unstable, because the potential perturbation lags behind the density perturbation which leads to an unstable increase of the initial perturbation. Under the assumption of cold ions $T_i = 0$ the parallel electric current is governed by a generalized Ohm's law for electrons

$$\eta \vec{j}_{\|} = \nabla_{\|} p_e - en \nabla_{\|} \phi \tag{2.10}$$

which equates the parallel current with the balance between the pressure (or density in the case of isothermal electrons) and the plasma potential. The parallel velocity is then assumed to be $\vec{v}_{i,\|} \approx \frac{\vec{j}_{\|}}{Zen}$. The divergence of

$\vec{j}_{\parallel}$ and $\vec{v}_{i,\parallel}$ is then put into the right hand side of the equations (2.2) and (2.9), respectively, while the divergence of the diamagnetic current and the $E \times B$ drift is 0 due to the assumed homogeneous magnetic field. This set of coupled equations after linearization and normalization then leads to the Hasegawa-Wakatani model for drift wave turbulence.

The cross-phase between the density and the plasma potential in drift wave turbulence should be nonzero, but rather small in comparison to the interchange instability as the electrons attempt to maintain a balance between the quantities.

Presence of instabilities in regions of the edge plasma

The two regions of the plasma edge with closed and open magnetic field lines, respectively, have significantly different properties. This also influences the dominance of either of the modes described above.

In the core region and the edge region well inside the LCFS the interchange instability develops linearly faster than the drift wave in the initial stages of the turbulent state, but later the drift wave turbulence overcomes the interchange modes and dominates through nonlinear processes [19].

Just inside the LCFS and close to it the greater radial pressure gradient contributes to the growth of the interchange modes, but the drift waves also influence this region from the more inward regions. The dynamics of this region may become even more complicated by the presence of shearing poloidal flows which affect the turbulent structures. Therefore, in this region no mode clearly dominates [20].

In the region of open field lines any parallel perturbations quickly expand because of the contact of the field lines with the vessel wall which hampers the conditions for the drift wave turbulence. Furthermore, the radial transport due to interchange modes is faster than the growth rate of drift waves. Therefore, in the SOL the interchange modes are expected to dominate unless collisionality is low.

2.3 Sheared poloidal flows in the plasma edge

If the poloidal plasma fluid velocity is roughly constant at some radial position along the poloidal coordinate, this structure is called a poloidal flow. When the poloidal flow velocity changes significantly along the radial coordinate with some radial wavenumber k_r it is called a sheared poloidal flow, because a structure (with a size smaller than the shearing wavelength $1/k_r$) passing through such a flow pattern would be sheared or torn apart by the different poloidal velocities moving it at different positions in the structure which would result in the structure becoming tilted and possibly eventually breaking up into smaller-scale structures as shown by the schematic in Figure 2.4. Therefore, sheared poloidal flows can decorrelate turbulent structures and reduce turbulent transport [21].

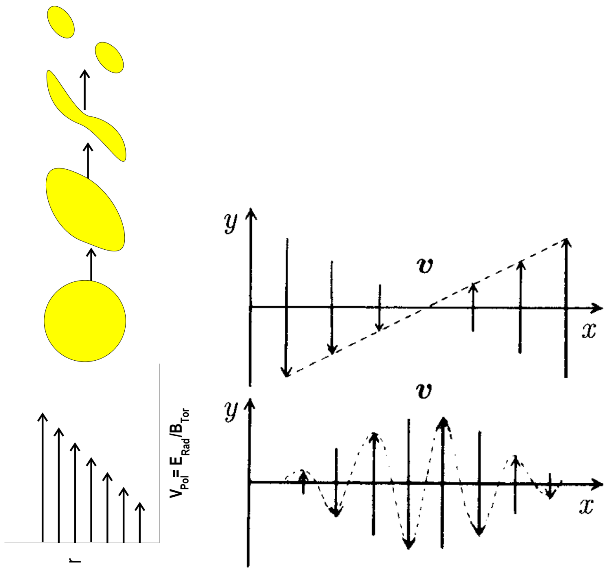

Figure 2.4: *Left:* Schematics of shearing and breaking up of a turbulent structure by a sheared flow. *Right:* Schematic comparison of a mean shear flow at the top and a a zonal flow at the bottom. Reproduced from [22].

Poloidal flows in the edge plasma are treated in a similar setting as electrostatic drift wave turbulence, and therefore the poloidal velocity is assumed to be dominated by the $E \times B$ drift velocity and the diamagnetic drift velocity. For this reason the radial component of the electric field which determines the poloidal $E \times B$ drift and the radial pressure gradient is a very important quantity in relationship to poloidal flows. Additionally, a locally homogeneous magnetic field is assumed which leads to the incompressibility of $E \times B$ and diamagnetic drift turbulent flows. Inverse radial shear of the magnetic field strength also acts to stabilize the pressure gradient, but that is beyond the scope of this thesis and only the electric field shear will be discussed.

There are two distinct sheared poloidal flow patterns present in the edge plasma: a mean flow related to the pressure gradient and zonal flows generated by turbulence itself. The mean flow has a radial wavelength (the characteristic length scale of variation, quantifiable e.g. by the inverse of the radial wavenumber component or $\frac{v_p}{\nabla_r v_p}$) on the macroscale and is stationary on the time scale of the pressure profile stationarity.

The zonal flow has a shorter wavelength in comparison with the mean flow, but it still significantly larger than the characteristic turbulence scale (microscale), therefore, it is a structure on the mesoscale. The zonal flows form radially-localized layers or zones (hence the naming “zonal”) of alternating flow directions, and therefore represent a limiting case of convective cells. As the flow velocities are assumed to be dominated by the $E \times B$ velocity, they in effect represent bands of poloidally and toroidally symmetric plasma potential surfaces with alternating polarity. The schematic in Figure 2.4 shows the difference between zonal flows and mean shear flows.

The short radial wavelength also results in a high shearing rate of the flow velocities. The zonal flow may vary in time with a very low frequency, usually a frequency in the order of ~ 1 kHz is observed in most experiments [23]. Recent Doppler backscattering measurements on JET [24] have even found stationary zonal flow structures on the radial profile of the radial electric field near its minimum inside the LCFS. The low-frequency zonal flow has a potential structure poloidally and toroidally symmetric and thus has mode numbers $n, m = 0$. If this potential structure becomes coupled through toroidal effects (geodesic curvature) to a $m = 1, n = 0$ density perturbation a geodesic acoustic mode (GAM) can develop [22]. This mode is therefore not poloidally completely symmetric in density. One common signature of a GAM is its frequency scaling where the GAM frequency ω_{GAM} scales with the sound velocity c_s [22]

$$\omega_{GAM}^2 \propto \left(\frac{c_s}{R}\right)^2 \tag{2.11}$$

This scaling property has been used to identify GAMs in several experiments [23], the frequency is usually in the order of ~ 30 kHz.

Zonal flows dissipate through collisional damping and secondary Kelvin-Helmholtz instabilities, and therefore cannot be sustained without the lack of a generation mechanism.

2.3.1 Generation mechanisms of poloidal flows

The different properties of the mean and zonal flows arise mostly from the different mechanisms which generate them.

The sheared mean flow is generated dominantly due to the balance of forces acting on the plasma in the radial direction [3], i.e. if the time derivative in (2.3) is neglected

$$E_r \approx B_p v_\phi - B_\phi v_p + \frac{1}{Zen_i}\frac{\mathrm{d}p_i}{\mathrm{d}r} \tag{2.12}$$

If the radial component of the $B \times v$ product does not significantly vary in the radial direction, the radial variation of the pressure gradient will be responsible for a radial shear of the radial electric field. As the pressure gradient may become quite large and negative (since the pressure decreases in the radial direction) around the narrow transport barrier inside the LCFS associated with the H-mode, the mean E_r may reach large negative values of several tens of kV/m in that region.

The typical radial profile of E_r is connected with (2.12) through the pressure gradient. In the SOL the pressure gradient is not very large and the plasma potential is determined mostly by the potential sheath formed at the vessel wall due to which the plasma potential gradually rises towards the LCFS by $\sim \frac{3k_BT_e}{e}$ with respect to the potential of the vessel wall [25]. The potential sheath is discussed in greater detail in section 3.2. This corresponds to a positive E_r in the SOL. Just inside the LCFS the pressure gradient is quite large and negative due to the substantial difference between the core and SOL plasma. This makes the E_r fall into negative values according to (2.12).

Therefore, the radial location of $E_r = 0\,\mathrm{V/m}$ and the associated maximum of the plasma potential roughly corresponds to the radial location of the LCFS. This fact is often used for the estimation of the radial location of the LCFS when its location given by .e.g. magnetic reconstruction is unreliable [26]. Further inside the LCFS the pressure gradient is not as large as just inside the LCFS and E_r becomes less negative. The region of the largest negative E_r values is often referred to as the E_r well .

The zonal flows are generated dominantly by the turbulent structures themselves through the so called Reynolds stress force [27]. The Reynolds stress tensor arises in Navier-Stokes type fluid equations like (2.3) when velocities $\vec{v}$ are separated into a mean $\langle\vec{v}\rangle$ and fluctuating component $\tilde{\vec{v}} = \langle\vec{v}\rangle - \vec{v}$ due to turbulence where $\langle\rangle$ denotes an average over a layer of stable flux surfaces [28]. After substitution of these components into the fluid momentum balance equation each term is averaged over $\langle\rangle$ again while terms linear in $\tilde{\vec{v}}$ average to 0, but quadratic terms do not. This means that average of the advective term in the total time derivative splits into two components $\langle\vec{v}\cdot\nabla\vec{v}\rangle = \langle\vec{v}\rangle\cdot\nabla\langle\vec{v}\rangle + \langle\tilde{\vec{v}}\cdot\nabla\tilde{\vec{v}}\rangle$. Due to the assumed incompressibility of the turbulent flow $\nabla\tilde{\vec{v}} = 0$ the second term can be rewritten as $\nabla\langle\tilde{\vec{v}}\otimes\tilde{\vec{v}}\rangle$ where $R_{kj}\left(\langle\tilde{\vec{v}}\otimes\tilde{\vec{v}}\rangle\right)_{kj} = \langle\tilde{v}_k\tilde{v}_j\rangle$ is the Reynolds stress tensor. The Reynolds stress tensor represents the correlation of velocities in different directions and corresponds to a shearing stress exerted on the plasma. The diagonal components representing plasma the pressure of turbulent structures is assumed to be negligible. If this term is put on the right hand side of the averaged fluid velocity equation it can be understood as a force which contributes to the total time derivative of the mean velocity through shear stress. For the poloidal component this will be

$$\frac{\mathrm{d}\langle v_p\rangle}{\mathrm{d}t} = -\partial_r\langle\tilde{v}_r\tilde{v}_p\rangle + \dots \tag{2.13}$$

because the term $-\partial_p\langle(\tilde{v}_p)^2\rangle$ is assumed to be negligible [28]. The radial-poloidal component of the Reynolds stress tensor $R_{rp} = \langle\tilde{v}_r\tilde{v}_p\rangle$ expresses the radial transport by turbulence fluctuations of poloidal momentum of the turbulence fluctuations. The radial gradient of R_{rp} term in (2.13) then represents an unequal radial transport of poloidal momentum which leads to an influx or loss of poloidal momentum at a given radial position on the left-hand side of the equation.

2.4 Predator-prey model of the L-H transition

As was explained in the previous sections, the turbulence is mostly driven by the pressure gradient and acts to reduce it. The zonal flows are generated dominantly by the turbulence itself whereby they drain energy from it and without it they dissipate. Initial models similar to predator-prey models therefore perceived turbulence as the prey upon which the zonal flows as predators feed. In Fourier-transformed wavenumber space the process could be described as a diffusion of the energy contained in the turbulence towards larger wavenumbers, i.e. smaller scales, where it dissipates, while due to the conservation of energy the zonal flow energy increases through an inverse energy cascade and drives the sheared flows. The process is very similar to the general process predicted for 2D turbulence as described in subsection 2.2.2.

However, such a simplified model cannot fully describe the evolution of the mean sheared flow which is necessary to achieve the H-mode. Without it the zonal flows may initially quench the turbulence, but without their turbulent drive they would dissipate through secondary instabilities and collisional processes and then the turbulence could grow again. Therefore, the evolution of the pressure gradient which is related to the mean sheared flow must be also taken into account.

These features have been put together into a 0D model by Kim and Diamond [29] where the system is described by the level of turbulence ϵ which is driven by the pressure gradient $N \propto \nabla_r p_i$ and damped by the zonal flows $V_{ZF} = \partial_r \tilde{v}_E$ and mean sheared flows $V = \partial_r \langle v_E \rangle$ decorrelating the turbulence structures. This model is considered one of the most likely to explain the L-H turbulence [28]. The zonal flows grow due to the energy transfer from the turbulence, but their growth is limited by the mean sheared flow and they damp by collisional processes and secondary instabilities. The pressure gradient is reduced by the turbulence and grows with the heating power input Q. A simplified closure between the mean sheared flows and the pressure gradient $V = dN^2$ is assumed. The models can be expressed in the following way

$$\partial_t \epsilon = a_1 \epsilon N - a_2 \epsilon^2 - a_3 V^2 \epsilon - a_4 {V_{ZF}}^2 \epsilon \tag{2.14}$$

$$\partial_t V_{ZF} = b_1 \frac{\epsilon V_{ZF}}{1 + b_2 V^2} - b_3 V_{ZF} \tag{2.15}$$

$$\partial_t N = -c_1 \epsilon N - c_2 N + Q \tag{2.16}$$

These simple equations can model the qualitative features of the L-H transition quite well. In Figure 2.5 a simulated evolution of the quantities is presented under the assumption that the heating input power is linearly increased in time $Q \propto t$.

It is evident that the intensity of turbulence first dramatically rises until the zonal flows start to develop and reduce the level of turbulence. However, once the turbulence is suppressed, the zonal flows are not driven by it anymore and dissipate due to damping, enabling the turbulence level to rise again. This is repeated several times in what is called limit cycle oscillations (LCO) which are characteristic by the zonal flow intensity lagging by $\sim \pi/2$ behind the turbulence intensity. Meanwhile, the pressure gradient and the associated mean sheared flow slowly increases while also oscillating. Once it is strong enough the turbulence intensity is all but suppressed and the pressure gradient then continues to increase as the heating power is increased.

In experiments the Intermediate phase (I-phase) with LCO is often observed as a modulation of the H_α light emission intensity due to the periodic

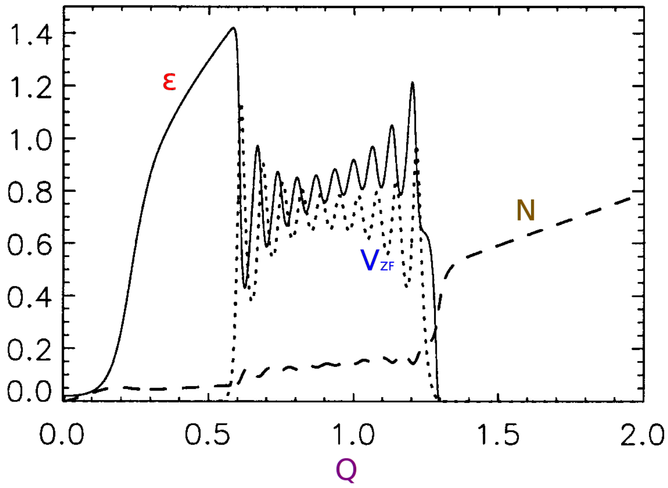

Figure 2.5: Qualitative prediction of the L-H transition from the Kim-Diamond model. Reproduced from [29] and edited.

transition between the state with reduced turbulence and reduced recycling of neutrals from the vessel wall and the state of enhanced turbulence with higher recycling rates which lead to increased light emission. The modulation frequency is usually in the order of a few kHz [30]. Measurements on ASDEX Upgrade [31] have showed that the LCO frequency scales as $f \sim \frac{\sqrt{B_\phi I_{pl}^3}}{p_{ped}}$ where I_{pl} is the plasma current, B_ϕ the toroidal magnetic field and p_{ped} the pedestal plasma pressure. However, the measurements suggested that the LCO dynamics are similar to those of type-III ELMs.

Probe measurements on HL-2A [32] show that this modulation is also visible on the evolution of the fluctuation intensity of the density and the strength of the radial electric field E_r. The cross-phase between these modulations is close to $\frac{\pi}{2}$ during the early phases of the I-phase which indicates that while the density fluctuations are the largest in the turbulent state, zonal flows grow and later they act to reduce the intensity of the density fluctuations, consistent with the LCO characteristics. These fluctuations were called type-Y LCO. In later stages of the I-phase the cross-phase changed to $-\frac{\pi}{2}$, i.e. the turbulence intensity lagged behind the E_r evolution. The E_r modulation seemed to be closely related to the modulation of the pressure gradient rather than to the Reynolds stress force in this type of LCO called type-J LCO. Closely before the transition to clear H-mode the cross-phase changed to $-\pi$, i.e. the E_r strength and turbulence intensity became anti-correlated.

Chapter 3

Experimental setup and diagnostics

3.1 The COMPASS tokamak

The COMPASS tokamak [12] is a device with major radius $R = 0.56\,\mathrm{m}$ and minor radius $a \approx 0.2\,\mathrm{m}$. It is capable of operating with an ITER-like divertor plasma cross-section (about 1:10 scale) which makes it an important device for multi-machine scaling experiments relevant to ITER physics. Its smaller size (in comparison to e.g. ASDEX Upgrade) has many benefits: The small size and shape contributes to the L-H transition power threshold being low enough for sufficiently high pure ohmic heating power to trigger the L-H transition. Two neutral beam injection systems (NBI) can be used to deliver even higher plasma heating power, but they were not used for the discharges presented in this thesis. The moderate typical heating power in the range of several hundred kW enables detailed studies of the plasma edge with electrostatic probes and beam emission spectroscopy, because the typical edge plasma temperatures are below 200 eV.

It is capable of operating with a plasma current up to $I_{pl} = 400$ kA, but most of the results presented in this thesis were obtained in discharges with I_{pl} in the range 150-250 kA. The toroidal magnetic field strength at the major radius in these discharges was $B_\phi(R) = 1.15\,\mathrm{T}$. The COMPASS tokamak can operate with various plasma cross-sections, from simple limited circular to divertor D-shape elongated plasma. All the presented results come from discharges of the latter type. The large energy demands of COMPASS are satisfied by two flywheel generators which accumulate the energy necessary to sustain all power sources and other supporting systems during the discharge.

The COMPASS tokamak is capable of using several types of working gasses: deuterium (D), hydrogen (H) and helium (He). However, only deuterium is routinely used in most discharges and it was also used in all the discharges presented in experimental results unless stated otherwise. While the working gas selection is fixed, other influences may change the actual gas mixture in the vessel, for instance there may be residual helium from glow-discharge wall conditioning procedures. The glow discharge aims to destabilize and remove impurities adsorbed on the vessel wall. The procedure usually takes ~ 15 minutes before each discharge.

The condition of the wall can be further improved by so called boronization of the vessel wall and plasma facing components by a thin layer of boron which acts as a “getter” and captures impurities and neutral gas which would otherwise adsorb on the vessel wall with lower binding energies. This improves the recycling dynamics of the wall as there are less impurities released due to contact with the plasma and this prevents large radiation losses and cooling. Boronization also stabilizes the condition of the vessel wall which helps to find a reproducible L-H transition threshold. Boronization is usually performed only before a stretch of several experimental campaigns, i.e. several weeks of experimental time.

The COMPASS tokamak is equipped with a broad range of diagnostics covering both core and edge plasma physics [33]. One of the routinely used diagnostics is the high resolution Thomson scattering system (TS) which can measure radial profiles of the electron temperature T_e and density n_e with a sampling frequency 60 Hz given by the repetition rate of the laser system. The line-averaged electron density can be measured with a high temporal resolution with a microwave interferometer. The plasma current is measured with a set of partial Rogovski coils. A set of several hundred magnetic Mirnov pick-up coils and several dozen saddle coils enable a detailed analysis of magnetic MHD modes and the plasma position. A diamagnetic flux loop is used to measure the perpendicular energy of the plasma. The magnetic and current measurements are synthesized by the EFIT program into a reconstruction of the poloidal magnetic flux surface function ψ, X-point position and other associated plasma parameters such as plasma shape, volume, surface, energy, etc. This collection of reconstructed signals will be referred to as the magnetic reconstruction signals in this thesis. Several photo-multipliers with spectral filters measure light radiation from the plasma at important spectral lines corresponding to the main plasma species and also impurities. Of particular interest is the H_α spectral line (wavelength $\lambda = 656.28\,\mathrm{nm}$ [34]) which corresponds to the light radiation from the main plasma content in hydrogen discharges. Since all the discharges presented in this thesis used deuterium as the working gas, the D_α spectral line ($\lambda = 656.104\,\mathrm{nm}$ [34]) is more appropriate. However, the filter for the H_α measurement includes the D_α line, and therefore this diagnostic will be referred to as the H_α signal in this thesis. The H_α signal used throughout this thesis was measured on the HFS, roughly tangential to the plasma flux surfaces. There are also several sets of Langmuir and ball-pen electrostatic probes embedded in divertor tiles or probe heads mounted on the horizontal midplane and vertical reciprocating manipulators. This thesis focuses on these probe heads mounted on the horizontal reciprocating manipulator and they are described in greater detail in subsection 3.2.3 and subsection 3.2.4

The different diagnostics are digitized by means of fast data acquisition systems with typical sampling frequencies in the order of several MS/s up to GS/s for diagnostics with special needs like the Thomson scattering system [35]. The digitized signals are then saved to a centralized database COMPASS database (CDB) from which they can be later retrieved using software bindings for common data analysis languages [36].

An example of a COMPASS discharge evolution is shown in Figure 3.1.

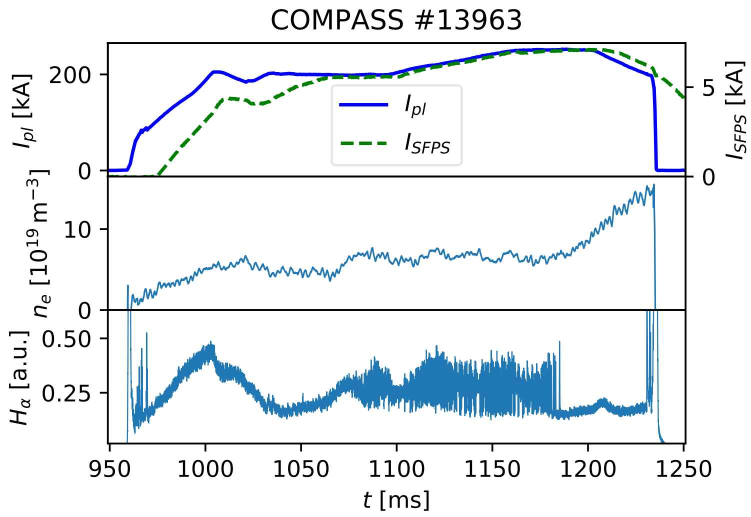

Figure 3.1: Evolution of COMPASS discharge #13963. The temporal evolution of the plasma current I_{pl} and the current in the shaping field coils I_{SFPS} is shown in the first plot. The second plot shows the evolution of the electron density as measured by the microwave interferometer. The last plot shows the evolution of the H_α signal which indicates the transition from the initial L-mode to the oscillations during the L-H transition and finally to the ELM-free H-mode.

The discharge begins by ramping up the toroidal magnetic field at $t = 0$ s. Near $t = 950$ ms the working gas is introduced into the vessel at a predefined low pressure. Around $t = 960$ ms the neutral gas breaks down into a circular plasma which is further ionized and heated by ramping up the plasma current induced in the plasma column. The current in the shaping field coils is ramped up accordingly in order to achieve the requested plasma shape up to $t = 1070$ ms. Once this initial phase is complete the real-time feedback system [37] maintains the plasma at the requested conditions in terms of I_{pl} and electron density n_e, plasma position, etc. For instance, a flat-top constant I_{pl} and n_e can be requested or a current ramp-up can be requested in the form of an arbitrary waveform. In the example discharge in Figure 3.1 a constant $n_e = 5.7 \times 10^{19}\,\mathrm{m}^{-3}$ and current ramp-up from 170 kA at 1100 ms to 250 kA at 1160 ms was requested. The feedback system uses several actuators, for instance changes in the currents in transformers and shaping and stabilizing coils or the valve opening level to regulate the gas-puff rate, in response to real-time measured key plasma parameters such as I_{pl} from Rogovski coils, line-averaged electron density n_e from a microwave interferometer and position and its change from magnetic pick-up coils [35]. It is evident that the current in the shaping field coils I_{SFPS} ramps-up as well in order to match the rise in I_{pl}. The H_α signal evolution shows that during the current ramp-up the plasma wen through a L-H transition and a clear ELM-free H-mode developed after 1190 ms. Due to this H-mode the density grows uncontrollably which results in a disruption around 1240 ms before the current has fully ramped down, otherwise the ramp-down after 1200 ms would have ended the plasma several tens of milliseconds later.

3.2 Electrostatic probes

One of the most common diagnostics used for plasma edge measurements are electrostatic probes. They are often used for the investigation of electrostatic turbulence since they can be used to measure electric fields, density and temperature with a high temporal resolution necessary for measuring turbulent phenomena.

They are partially invasive in the sense that they locally (only within the distance of several Debye shielding lengths) perturb the plasma. A local equilibrium between the probes and the plasma develops and from it several local properties of the surrounding plasma can be deduced. They are usually constructed from durable, conducting materials like graphite, tungsten or stainless steel since they are fully or partially exposed to the edge plasma. Their sizes are usually in the order of several mm and they usually have simple geometric shapes, e.g. cylinders or disks which enable analytic theoretical treatment of the particle currents incident on their surface. However, their size and shape can become more complicated when they are intended to be used under higher heat loads. In this thesis two types of electrostatic probes are used: Langmuir and ball-pen probes. A brief theoretical description of their measurement properties is given in subsection 3.2.1 and subsection 3.2.2.

The results presented in this thesis were obtained by probes located on more complicated arrangements called probe heads described in subsection 3.2.3 and subsection 3.2.4. These probe heads were mounted on the horizontal midplane reciprocating manipulator (HRCP) which enables inserting the probe head into the plasma for ~ 100 ms in a “harpoon-like, in-and-out” manner. The reciprocation trajectory prevents excessive heat loads on the probe head while obtaining measurements at different radial positions, thereby enabling the measurement of radial profiles of various quantities.

3.2.1 Langmuir probe

The Langmuir probes used in this thesis are of one of the most common designs used in the edge plasma, they are simple graphite, cylindrical rods with a diameter ~ 1 mm and a length of ~ 1.5 mm of the part which directly protrudes into the plasma.

When dealing with electrostatic probes, potentials and voltages are measured with respect to some reference electrode, usually the vessel wall. This was also the case in this thesis. Therefore, the electrostatic plasma potential ϕ is in general positive with respect to the reference electrode, because the more mobile electrons are accumulated on the vessel wall in the initial stages of the plasma discharge and the vessel wall becomes negatively charged. A so called “sheath” layer is then formed around the vessel wall where electron and ion densities vary in such way so as to shield the bulk plasma from the negative charge of the vessel wall [25]. This dynamic equilibrium between electrons and ions leads to the total electric current incident on the vessel wall to be 0 A. Similar sheath layers form around electrostatic probes exposed to the plasma. The following is a brief introduction to the classical theory of Langmuir probes based on [38].

If a negative biasing voltage V_B sufficiently smaller than the plasma potential $V_B << \phi$ is applied between the probe and the reference electrode, the electrons are repelled from the probe while the ions are attracted. The electric current of particles incident on the probe then constitutes mostly of ions and tends to saturate at the so called ion saturation current I^+_{sat} when the biasing voltage is further decreased. In practice, the sheath around the probe may expand when the biasing voltage is further decreased and for small probes this leads to the current following a linear trend rather than fully saturating.

Symmetrically, when the biasing voltage is sufficiently positive $V_B >> \phi$, the ions are repelled from the probe while the electrons are attracted. However, the electron saturation current I^-_{sat} is much higher than the ion saturation current due to the high mobility of electrons for commonly used working gases and may damage the probe. Furthermore, sheath expansion may occur and the linear trend may lead to even higher electron currents with large biasing voltages. Therefore, the electron saturation current usually is not measured with biasing voltages as large in absolute value as is the case with I^+_{sat}.

Both saturation currents are proportional to the respective particle charge, density, speed at which the particles enter the sheath and the probe collection area A where the subscript q indicates the type of the particle. For electrons the entry speed is their thermal speed $v_{e,th} \propto \sqrt{\frac{k_B T_e}{m_e}}$ where T_e and m_e are the electron temperature and mass, respectively and k_B is the Boltzmann constant. The electron saturation current then is $I^-_{sat} = -e n_e v_{e,th} A$ where e is the elementary charge. For ions the entry speed is the sound speed $c_s = \sqrt{k_B \frac{T_e + Z T_i}{m_i}}$ where T_i and m_i are the ion temperature and mass, respectively for Z-times ionized ions. Therefore, the measurement of I^+_{sat} can give an estimate of the plasma density n further away from the rpobe(assuming quasineutrality) using the formula [25]

$$I^+_{sat} = AZe\frac{1}{2}nc_s \tag{3.1}$$

Under the assumption of quasi-neutrality $n_i = n_e$ and comparable temperatures $T_e \approx T_i$ the ratio of the electron and saturation currents $\Re = \frac{-I^-_{sat}}{I^+_{sat}}$ is proportional to the square root of the temperature and mass ratios $\Re \propto \sqrt{\frac{m_i}{m_e}} \frac{1}{\sqrt{1+\frac{T_i}{T_e}}}$. Due to $m_i >> m_e$ the ratio may be in the range of $\sim 10^1$. This simple dependence holds only for simplified conditions and does not account for more complicated phenomena like secondary emission of electrons. Nevertheless, the $\Re$ coefficient remains a function of these square roots of ratios.

When the probe is isolated from the reference electrode, the electrons in the plasma are collected on the probe in the initial stages of the plasma exposure as the electrons have higher thermal speeds than ions due to their smaller mass, and the probe becomes negatively charged and a sheath layer develops in a similar way as was the case with the vessel wall. Due to this equilibrium the probe "floats" at a so called floating potential V_{fl} lower than the plasma potential ϕ with respect to the reference electrode while the total electric current incident on the probe is $I(V_{fl}) = 0\,\mathrm{A}$.

If the biasing voltage V_B is close to the floating potential and not too positive or too negative to reach the saturation currents range, the total electric current $I(V_B)$ incident on the probe constitutes of the electron and ion currents $I = I_e + I_i$. For a Maxwellian distribution these current contributions have exponential forms

$$I_e = I_{sat}^{-} \exp\left(\frac{e(V_B - \phi)}{k_B T_e}\right) \qquad I_i = I_{sat}^{+} \exp\left(\frac{-e(V_B - \phi)}{k_B T_i}\right) \tag{3.2}$$

Since $V_{fl} < \phi$ and $I_{sat}^{+} << |I_{sat}^{-}|$ it is assumed that $I_i(V_{fl}) \approx I_{sat}^{+}$, and therefore $I(V_{fl}) = 0 \approx I_{sat}^{+} + I_{sat}^{-} \exp(\frac{e(V_{fl}-\phi)}{k_B T_e})$ from which the floating potential can be related through a quasi-linear formula to the plasma potential as

$$V_{fl} = \phi - \alpha \frac{k_B}{e} T_e \tag{3.3}$$

where $\alpha = \ln(\Re)$. In principle, α depends also on T_e and T_i, but since the temperature dependence is through the logarithm of a square root, it is assumed that a temperature variation has negligible effect on the α coefficient. In experiments on tokamaks COMPASS and ASDEX Upgrade in deuterium plasmas with a strong magnetic field the for graphite Langmuir probes of a 0.9 mm diameter and 1.5 mm length was found to be close to $\alpha_{LP} \approx 2.8$ [26]. Therefore, such Langmuir probes measure a floating potential significantly differing from the plasma potential. This difference is even more important when analyzing fluctuations

When T_e is expressed in eV units in the formula, the factor $\frac{k_B}{e}$ is included in the eV unit, and therefore is not written explicitly anymore.

The properties of the $I(V_B)$ dependence is often measured as a so called $I - V$ characteristic of the probe by measuring the electric current on the probe while the biasing voltage is swept within some voltage range with a frequency sufficient to obtain enough data points of the $I(V_B)$ dependence. From the measured $I - V$ characteristic the local plasma properties can be deduced by fitting the theoretical dependence (3.2) to the measured data under the assumption that the sweeping frequency is higher than the inverse of the time-scale on which plasma parameters change. In practice, the current measurements in the plasma edge are distorted by coherent structures flowing over the probe, so a statistical average of several characteristics obtained from several sweeps is used for the fitting.

3.2.2 Ball-pen probe

The ball-pen probe [39] was designed with the goal of reducing the α coefficient to a value as low as possible. As suggested by (3.3), the floating potential measured by such a probe would be very close to the plasma potential.

The reduction of the electron current contribution is achieved by the probe collector being retracted into a tunnel perpendicular to magnetic field lines until the tip of the collector is below the top entry tunnel hole. The retraction depth of the collector pin is set to a depth comparable to the electron gyroradius ρ_e. Therefore, electrons which enter the tunnel gyrate around the magnetic field lines but should not reach the collector pin, while ions with a significantly larger ion gyroradius ρ_i can still reach the collector. An appropriate retraction depth setting can thus limit the number of electrons collected by the probe and thereby balance the electron and ion current contributions and approach $\Re \sim 1$.

The collector is usually manufactured from stainless steel and has a conical tip. The inner tunnel surface is made of an insulating material, usually corundum or boron nitride.

Experiments [40, 39] and recent simulation efforts [41] paint a more complicated picture of the transport mechanisms responsible for the balancing of the ion and electron current contributions. The exact retraction depth was found to affect the α coefficient very little beyond a certain depth of several ρ_e. Simulations suggest that this is due to a $E \times B$ field transporting the electrons deeper into the tunnel. The electric field responsible for this transport arises from the currents of particles hitting the tunnel walls which charges the opposite sides of the tunnel with opposite charges and this charge imbalance then leads to an electric field between these opposite sides of the tunnel. Simulations suggest that the α coefficient is influenced by the diameter of the tunnel as well since it can limit entry of ions with a gyroradius comparable with the tunnel diameter.

While the ball-pen probes designed and used in previous experiments have not been able to achieve $\alpha = 0$, it was experimentally observed that the coefficient α of a ball-pen probe (BPP) is reduced to $\alpha_{\text{BPP}} = 0.6$ in deuterium plasmas with strong magnetic fields in the COMPASS [12] and ASDEX Upgrade (Axially Symmetric Divertor EXperiment Upgrade) tokamaks [26]. Therefore, the floating potential measured by a ball-pen probe $\phi^{\text{BPP}} = \phi - 0.6T_e$ according to (3.3) is assumed to be close to the true plasma potential ϕ.

This also enables fast and local measurements of T_e from the difference of closely positioned ball-pen and Langmuir probes [42, 43]. Recent simulation efforts [41] support this empirical evidence. When a Langmuir probe measures a floating potential V^{LP} and a close-by ball-pen probe measures a plasma potential ϕ^{BPP}, the electron in eV units can be estimated with the formula

$$T_e = \frac{V_{fl}^{\text{LP}} - \phi^{\text{BPP}}}{\alpha_{\text{LP}} - \alpha_{\text{BPP}}} \tag{3.4}$$

where the coefficients α_{LP} and α_{BPP} are the α coefficients for the Langmuir and ball-pen probe, respectively. The formula results from the two linear equations based on (3.3) with T_e in eV units: $V_{fl}^{\mathrm{LP}} = \phi - \alpha_{\mathrm{LP}} T_e$ for the Langmuir probe and $\phi^{\mathrm{BPP}} = \phi - \alpha_{\mathrm{BPP}} T_e$ for the ball-pen probe.

3.2.3 Reynolds stress multi-pin probe head

An appropriate geometric arrangement of electrostatic probes enables the approximation of electric fields by the difference of potentials measured by spatially separated probes. This method offers a high temporal resolution for the electric field measurements and its accuracy is limited mainly by the spatial separation between the probes. Turbulence investigation requires the simultaneous measurements of the plasma potential and associated electric fields and density and temperature. Therefore, complex probe arrangements called probe heads (since they are usually placed on the end of a reciprocating manipulator) with multiple probes have been constructed for experiments on various machines [44, 45, 46, 47, 48] in order to facilitate such measurements.

Such probe heads almost exclusively use Langmuir probes for floating potential measurements which are then used to calculate electric fields. However, the gradient of the floating potential is a superposition of the gradients of the electron temperature and the plasma potential as suggested by (3.3). This is especially of great importance when the fluctuations of ϕ and related electric fields are of interest for the estimation of the Reynolds stress and other quantities related to transient phenomena, because the Langmuir probe measures both electrostatic and thermal fluctuations. For these reasons a new multi-pin probe head was designed and used at the COMPASS tokamak with the intention of comparing Reynolds stress measurements obtained with ball-pen and Langmuir probes. The probe head consists of both Langmuir and ball-pen probes in similar geometric configurations which enables simultaneous measurements of the radial and poloidal electric fields using the two different probe types in order to study the covariance of the fields (i.e. the Reynolds stress) measured with and without the influence of the electron temperature T_e. While Reynolds stress measurements were on of the primary motivations for its design and construction, another motivation was to use the probe head to investigate in general transient phenomena related to L-H transition physics such as LCO and zonal flows described in chapter 2.

The probe head consists of ball-pen and Langmuir probe tips in nearly the same spatial configurations in order to perform a direct comparison of the electric fields (and derived quantities like the Reynolds stress) obtained from the plasma and floating potential, respectively. The potentials are measured with a high temporal resolution (data acquisition systems with 5 MS/s). The electric fields are calculated as the negative of the difference of plasma or floating potentials of appropriately situated probes divided by their distance. Figure 3.2 shows a schematic of the probe head with labeled probes. The probe head is installed on a horizontally reciprocating manipulator on the midplane [33] which enables measurements of radial profiles of various quantities [26]. The radial electric field E_r is calculated from the difference

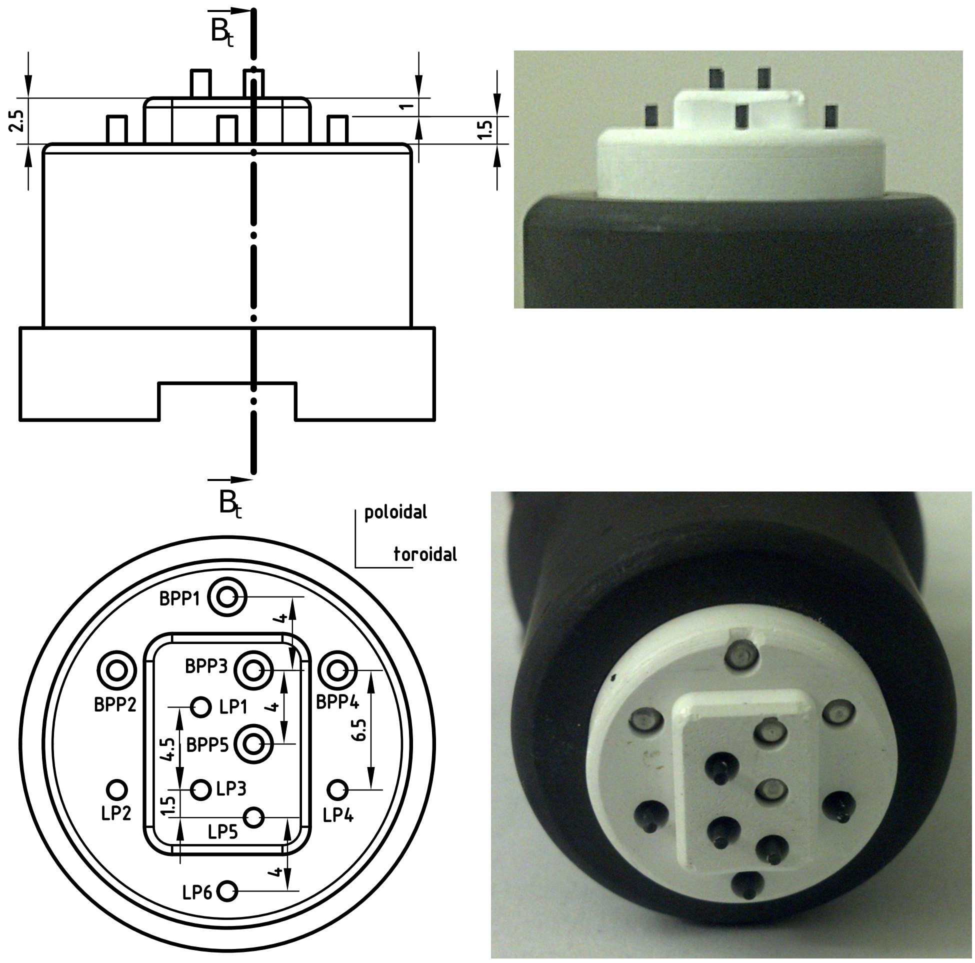

Figure 3.2: Schematic figure of the multi-pin probe head with ball-pen probes (BPP) and Langmuir probes (LP). All distances are in mm.

of plasma potentials of probe `BPP3` and virtual probe `BPP2_4` (from here on referred to as the probe-difference method). The plasma potential of virtual probe `BPP2_4` is obtained by averaging plasma potentials from probes `BPP2` and `BPP4` ($\phi^{BPP2\_4} = (\phi^{BPP2} + \phi^{BPP4})/2$) and is located between them, putting it radially 2.5 mm below probe `BPP3`. The same technique is used to create a virtual probe `LP2_4` from probes `LP2` and `LP4` and it is located 2.5 mm radially below probe `LP3`. The averaging is also assumed to mitigate effects of the partial shielding which likely plays a role due to the different upstream/downstream (with respect to the magnetic field lines) ratios of particle fluxes for the two probes on either side which was observed to shift the potential by some offset on either side, but left the fluctuation characteristics unchanged. This correction is therefore mostly useful only for comparing average radial profiles. Any toroidal displacement is assumed to be negligible due to the high conductivity along the field lines in the toroidal direction. The radial electric field in kV/m from ball-pen probes is then calculated as $E_r^{BPP} = (\phi^{BPP3} - \phi^{BPP2\_4})/2.5$ and analogously for Langmuir probes

$E_r^{LP} = (V_{fl}^{LP3} - V_{fl}^{LP2\_4})/2.5$. The corresponding poloidal electric field E_p in kV/m is calculated from the difference of plasma potentials of probes BPP3 and BPP5 as $E_p^{BPP} = (\phi^{BPP3} - \phi^{BPP5})/4$ or floating potentials of probes LP1 and LP3 as $E_p^{LP} = (V_{fl}^{LP1} - V_{fl}^{LP3})/4.5$.

The calculated electric fields are located at the points between the probes used in the difference. Due to construction and material constraints the points at which the electric fields are measured are not exactly the same for E_r and E_p for either probe type. This slight displacement might introduce some phase shift. Nevertheless, the displacement is the same for each of the probe types, and therefore the comparison should remain valid.

Boron nitride was chosen as the main material for the probe head support, because one of the goals of this multi-pin probe design was to make the distance between probes as small as possible in order to get accurate values of radial and poloidal gradients in measured quantities. The second goal was to minimize the overall dimensions of the probe head in order to limit the perturbation of the edge plasma by the inserted probe head. A graphite probe head bulk would have required extra shielding between the probes and the conductive graphite head bulk which would increase the distances between the probes. Furthermore, a graphite probe head support might pose the risk of locally short-circuiting magnetic flux surfaces.

The graphite Langmuir probes have the same geometry as used on ASDEX Upgrade [26] with a diameter of 0.9 mm. Each Langmuir probe protrudes 1.5 mm above the surface of the probe head as shown in schematic on Figure 3.2. The ball-pen probe collector is made of a stainless-steel rod with a 2 mm diameter and is retracted by 0.5 mm within a 3 mm deep hole in the boron nitride support which poses as a shielding tube with a 2 mm diameter. The exact retraction depth of the collector does not need to be calibrated beyond a minimum depth of several electron gyro-radii ρ_e as long as the probe performs with the expected α_{BPP} coefficient as shown in previous experiments [39, 40] and also found in simulations [41].

The top probe level (containing e.g. BPP3, inserted radially most inwards) is 2.5 mm radially above the bottom probe level (containing e.g. BPP2). Any of the Langmuir probes can work in the floating regime or can be biased in order to measure either the floating potential V_{fl}^{LP} or the ion saturation current I_{sat}^{+} which makes it possible to locally measure fluctuations of density, temperature and plasma potential simultaneously.

The whole probe head is rotated on the reciprocating manipulator around the radial axis (clockwise in Figure 3.2) by 5° in order to align it with the magnetic field lines. In the discharges presented in this thesis the pitch angle was close to $\sim 10°$ and varied by $\sim 1°$ over the reciprocation range. However, such misalignment of $\sim 5°$ results in a reduction of poloidal distances by $1 - \cos(5°) \sim 0.4\%$, i.e. tens of μm for scales of several mm which is negligible in comparison to the probe sizes in the order of a few mm. The triangle-like placement of probes on the top level enables very close placements of neighboring probes while maintaining minimal poloidal separation between them necessary to avoid shadowing between them. However, the smallest poloidal separation is ~ 0.5 mm between e.g. probes LP1 and BPP3 and may become comparable with the estimated ion gyroradius further beyond the last close flux surface (LCFS) for the typical edge electron temperatures $\sim 10-50$ eV and toroidal field $B_\phi \sim 0.9$ T (1.15 T at the major radius) at the radial positions which the reciprocating probe may encounter far beyond the LCFS. Therefore, this probe head design limits its viability to the SOL and core plasma just inside the LCFS.

3.2.4 Modified Reynolds stress multi-pin probe head

The design of the probe head was later (after the Reynolds stress profile measurements) modified in order to account for the misalignment between the locations of the E_r and E_p estimates which might lead to some phase shift between them as discussed in subsection 3.2.3. This was achieved by adding another toroidally-aligned series of 3 BPPs similar to BPP2, BPP3, BPP4 in Figure 3.2 poloidally below them. The E_r estimates obtained from either of these series then can be averaged in the poloidal direction to the same poloidal location as that of the E_p estimates, while the E_p estimates from the top and bottom can be averaged in the radial direction to the same radial location as the E_r estimates. Due to space constraints, it was not possible to add a similar series of LPs. The resulting design schematic is shown in Figure 3.3. Additionally, a different type of purer boron nitride was used for the construction of this probe head. The new material is supposed to have a lower concentration of impurities and a higher density. The lower impurity content is likely to decrease the interaction between the probe head and the plasma and to prevent plasma cooling due to out-gassing of impurities. The top level extrusion was extended in the poloidal direction to the very

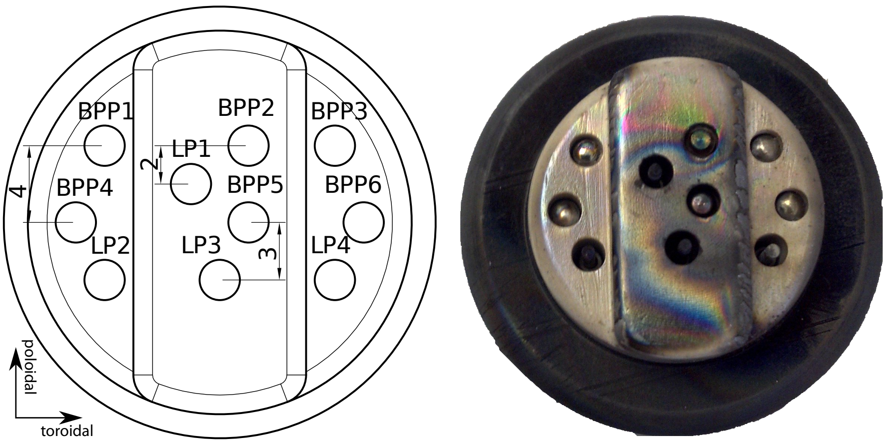

Figure 3.3: Schematic of the modified Reynolds stress multi-pin probe head design with ball-pen (BPP) and Langmuir (LP) probes and the corresponding picture of the probe head. The schematic orientation is the same as the bottom-left schematic in Figure 3.2. All distances are in mm. The picture shows the probe after it was used in the experiment, hence the shiny coating resulting from interactions with plasma.

ends of the bottom level. The extrusion height in the radial direction remains 2.5 mm. This change ensures that probes on either side of the extrusion are completely shielded from one side even in the case of large magnetic field misalignment.

This extension was possible due to the removal of probes `BPP1` and `LP6` (as labeled in the original design). The removal was necessary, because the probes in the center (e.g. `LP1`) had to be secured with screws from the sides of the probe head, but the inclusion of new probes `BPP4` and `BPP6` meant that such screws had to be inserted from the top and bottom in Figure 3.3. Furthermore, the removed probes turned out to be of little use for measurements.

The Langmuir probes `LP1` to `LP4` have kept their original labels and use, however, the distance from `LP1` to `LP3` has increased by 0.5 mm to 5 mm due to space constraints. Probe `LP5` was removed for the same reason for which `LP6` was also removed.

The labeling and use of ball-pen probes has changed significantly. The probes labeled `BPP1, BPP2, BPP3` are the probes `BPP2, BPP3, BPP4` in the original design. Their use remains similar: Potentials measured by probes `BPP1` and `BPP3` are averaged to a probe potential of virtual probe `BPP1_3`. The difference between the probe potentials measured by probes `BPP2` and `BPP1_3` is then used as an estimate of E_r at their poloidal location and a radial location halfway between them. A similar averaging and difference scheme is used for probes `BPP4, BPP5, BPP6`. Probes `BPP4` and `BPP6` are shifted slightly toroidally outwards in order to satisfy material thickness constraints. This toroidal shift is assumed to be negligible.

Thanks to this setup, the E_r calculated from the differences of potentials measured by probes `BPP2`,`BPP1_3` and `BPP5`, `BPP4_6`, respectively, can then be averaged in the poloidal direction to a poloidal location halfway between them. Similarly, the E_p calculated from the differences of potentials measured by probes `BPP2`,`BPP5` and `BPP1_3`, `BPP4_6`, respectively, can then be averaged in the radial direction to a radial location halfway between them. Therefore, the final averaged E_p and E_r estimates are located at the same poloidal and radial locations halfway between all the BPP probes and no phase shift should be observed. These corrected electric fields can then be compared to the uncorrected fields as was done in the case of the original design and the presence of a phase shift and its effect on e.g. Reynolds stress calculation can be investigated.

Part II

Results

Chapter 4

Measurement characteristics of the Reynolds stress multi-pin probe head

The measurement properties of the new probe head described in subsection 3.2.3 (the original design in Figure 3.2) were inspected in order to asses the validity of the results derived from the measurements conducted with the probe head. In section 4.1 the measurement characteristics of the 2 mm ball-pen probe are described, in particular the α_{BPP} coefficient is estimated. This coefficient is further used to compare the temperature calculated from the differences of potentials measured by ball-pen and Langmuir probes and by the Thomson scattering system in subsection 4.1.1.

The method for calculating E_r from differences of radially separated probes is compared with E_r estimated from radial profiles of probe potentials in section 4.2 and the fluctuation characteristics of electric field components calculated from ball-pen and Langmuir probes are compared in subsection 4.2.1.

Typical time traces of raw signals of potentials measured by nearby probes and differences between potentials measured by radially separated probes which are proportional to the calculated radial electric fields are shown in Figure 4.1. The traces of the plasma potential measured by `BPP5` are similar to the floating potential measured by `LP3`, but the floating potential measured by the Langmuir probe is lower and exhibits more fluctuations, presumably due to the electron temperature. The calculated radial differences have similar characteristic in that respect. The differences between `BPP3` and either `BPP2` or `BPP2_4` are very similar in terms of fluctuations and differ mostly by some stationary value. Thus this averaging does not affect Reynolds stress calculation from fluctuations.

4.1 Characteristics of the 2 mm ball-pen probe

The small distances between probes have been achieved in part by the use of small 2 mm ball-pen probes which are substantially smaller than the BPP used in previous experiments [26] which may in principle have different measurement properties. Therefore, the measurement properties of these new 2 mm BPP, particularly their α_{BPP} coefficient, were analyzed by measuring their I-V characteristic with a voltage-sweeping frequency of 1 kHz with

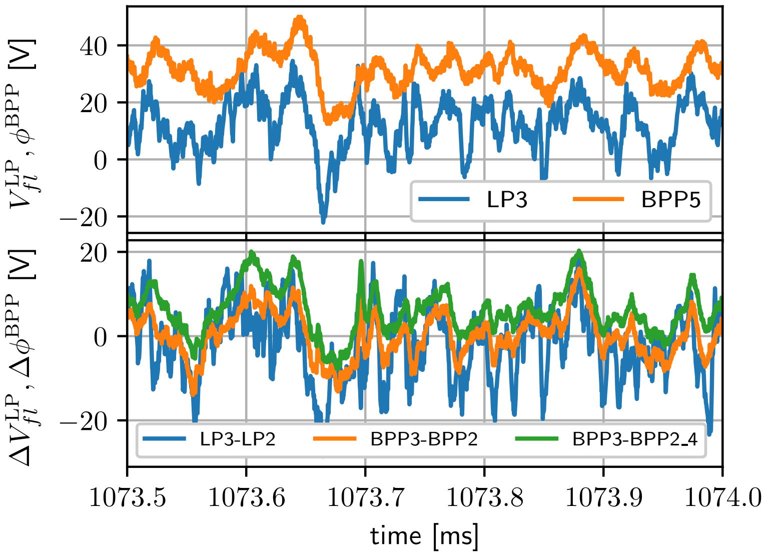

Figure 4.1: Example time traces of potentials measured by nearby probes and differences of measured potentials between radially separated probes in COMPASS discharge #13685.

voltages in the range $V \in (-180, 180)$ V. The relatively high sweeping frequency was necessary due to the fast reciprocation of the probe head. Two $I - V$ characteristics for BPP5 in L-mode COMPASS discharge #13681 from different reciprocation positions $\Delta R = R - R_{\mathrm{LCFS}}$ are shown in Figure 4.2. The displayed data was obtained by averaging voltage bins over 2 ms, i.e. 4 sweeps.

Before the actual bin-averaging, several pre-processing steps were taken: Firstly, the measured sweeping voltage signals was lowpass filtered to 10 kHz in order to remove noise which would complicate the placement of data into voltage bins. The cutoff frequency 10 kHz was chosen based on the cross-coherence with the measured current signals, which showed a high level of coherence from 1 kHz (the sweeping frequency) and decreased to 0 up to 1 kHz. Voltage offset was also removed, which was necessary to obtain correct V_{fl} values in the $I - V$ characteristics.

Secondly, the capacitive current I_C superimposed on the probe current was removed. This capacitive current I_C arises due to the finite capacity C of the cables connecting the probe and the data acquisition system input. The current is related to the time-derivative of the sweeping voltage $I_C = C\frac{\mathrm{d}V}{\mathrm{d}t}$. In principle, I_C may be slightly shifted with respect to the voltage signal due to the cables acting as an RC-filter. However, for this relatively low sweeping frequency (in comparison to the RC-filter characteristics) the phase shift is negligible, which was checked in the raw data. The capacity C of the circuit was estimated by performing a linear least-squared regression of the measured current signal (lowpass filtered to 10 kHz) before the plasma (up to 950 ms) on the sweeping voltage signal (also filtered). The regression also provided a current offset I_0. The modeled capacitive current $\hat{I}_C = C\frac{\mathrm{d}V}{\mathrm{d}t} + I_0$

was then removed from the raw measured and unfiltered current signal. This correction is necessary in order to resolve the correct 0-crossing of the current on the $I-V$ characteristic corresponding to V_{fl}.

The position of the LCFS obtained from the magnetic reconstruction R_{LCFS} is about 2 cm radially inwards compared to the maximum of the plasma potential associated with the LCFS velocity-shear layer as was also observed in [26]. Therefore, the first plot shows the $I-V$ characteristic measured quite far in the SOL while the second was measured just before the reciprocating probe passed the LCFS. Due to the small size of the BPP the measured current

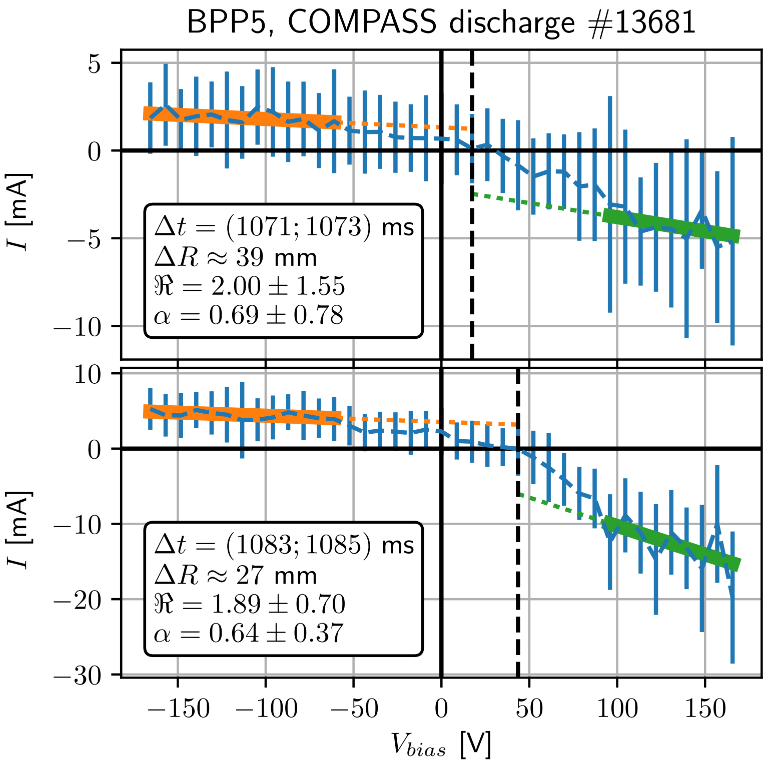

Figure 4.2: $I-V$ characteristics of BPP5 in COMPASS discharge #13681 at two different radial positions $\Delta R = R - R_{\mathrm{LCFS}}$ averaged over 2 ms, i.e 4 sweeps. Each data point represents a voltage bin of which the median and standard deviation was taken. The thick line segments show the domain of the linear fits of the current saturation trends. The dotted lines depict the extrapolation of the current saturation trend to the floating voltage V_{fl} where the ratio of the extrapolated values $\Re$ and coefficient $\alpha = \ln(\Re)$ are evaluated.

is quite low, in the order of several mA. This greatly complicates the analysis of the I-V characteristics due to the high noise amplitude, particularly in the electron-saturation branch, and results in large errors in estimated saturation current ratios. Figure 4.2 shows the IV-characteristics which exhibited the least noise. Neither branch of the I-V characteristic exhibits a clear saturation current, but rather a linear current saturation trend as was also observed in previous experiments [26]. The saturation trends were extrapolated to the floating potential V_{fl} (where the current is 0 A) where their ratio $\Re$

was calculated and from it the coefficient $\alpha_{\text{BPP}} = \ln(\Re)$ was obtained. The coefficient α_{BPP} is close to the value 0.6 for larger BPP [26] regardless of the radial position, although the large noise in the current measurements results in high errors in the estimate.

4.1.1 Comparison of T_e measured by probes and by Thomson scattering

The coefficient $\alpha_{\text{BPP}} = 0.6$ was also used for the comparison of the electron temperature T_e radial profiles obtained from the difference of potentials measured by `BPP3` and `LP1` with the temperature profiles measured with the Thomson scattering (TS) diagnostic [33]. The electron temperature was calculated from the probe potentials using formula (3.4) with the coefficients $\alpha_{\text{LP}} = 2.8$ and $\alpha_{\text{BPP}} = 0.6$. Figure 4.3 shows a comparison of the measured T_e radial profiles. The radial coordinate is relative to the LCFS location R_{LCFS} taken from the magnetic reconstruction. However, the position of the velocity shear layer associated with the LCFS, i.e. the maximum of the plasma potential profile measured by `BPP3` was shifted outwards by ~ 2 cm and is denoted by `LCFS(BPP3)` in Figure 4.3. Because the TS radial profiles are measured vertically and are mapped to the midplane according to the magnetic reconstruction, the TS profile had to be shifted by ~ 2 cm outwards to align with `LCFS(BPP3)` as was also done in [26]. The TS profile measured

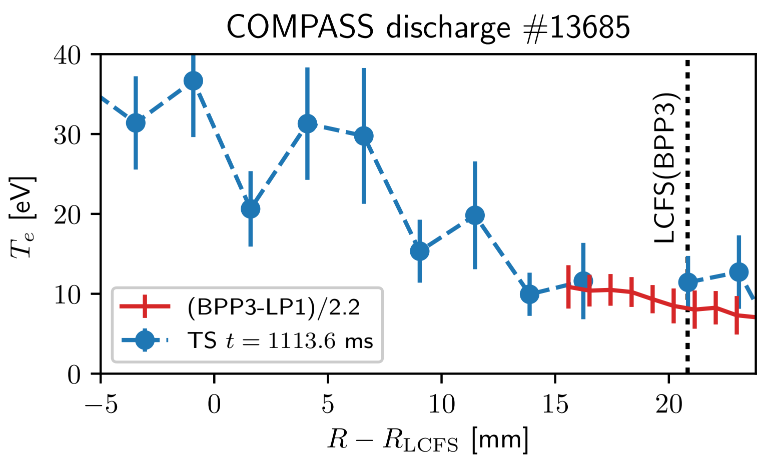

Figure 4.3: Comparison of electron temperature T_e radial profile as measured by the Thomson scattering (TS) diagnostic and calculated from the differences of probes `BPP3` and `LP1`. The x-axis is the radial midplane coordinate relative to the LCFS location R_{LCFS} taken from the magnetic reconstruction. The LCFS(BPP3) position denotes the maximum of the plasma potential measured by `BPP3`.

at $t = 1113.6$ ms agrees well with the T_e measured with the probes while they were inside `LCFS(BPP3)`, more outwards the TS measurement is unreliable and does not correspond to the time of the probe measurements at that location. The TS profile shows quite low temperatures due to the plasma cooling down while the probe is deep inside the LCFS as was observed on preceding and subsequent TS profiles. This is likely due to the interaction of the plasma with the probe head which was also observed on fast camera recordings.

Based on the I-V characteristics and the comparison to the TS profile it was concluded that the smaller 2 mm BPP has the same measurement properties at the larger BPP and the coefficient $\alpha_{\mathrm{BPP}} = 0.6$ will be used from here on.

4.2 Analysis of the probe-difference method of measuring E_r

The method for estimating E_r from the difference of floating potentials measured by radially separated probes described in subsection 3.2.3 was compared with other methods used for estimating E_r in order to validate the measurement method.

One method to obtain the slow component of the radial electric field $\langle E_r \rangle$ is to perform a differentiation of the radial profile of the plasma potential. The differentiation is performed on the slow component of the floating or plasma potential $\langle V_{fl} \rangle$, $\langle \phi^{\mathrm{BPP}} \rangle$ in the time domain and then it is divided by the reciprocation speed $\frac{\mathrm{d}r}{\mathrm{d}t}$ which follows from the chain derivation rule $\frac{\mathrm{d}\langle V_{fl} \rangle}{\mathrm{d}r} = \frac{\mathrm{d}\langle V_{fl} \rangle}{\mathrm{d}t} \frac{\mathrm{d}t}{\mathrm{d}r}$. The division by the reciprocation speed is performed after the high frequencies of the passing turbulence are suppressed by a 100 Hz lowpass filter, otherwise the division would result in a very high electric field for fast fluctuations of the potential. In the top panel in Figure 4.4 the radial profiles of plasma potentials ϕ^{BPP} measured by BPPs and floating potentials V_{fl}^{LP} measured by LPs from the inward reciprocation of the probe head in COMPASS discharge #12554 are shown. The radial profiles are plotted with respect to the radial distance from the last closed flux surface (LCFS) on the midplane $\Delta R = R - R_{\mathrm{LCFS}}$. The position of the LCFS is obtained from the magnetic reconstruction, but its position does not correlate well with the maximum of the plasma potential which is around $\Delta R = 15$ mm. Such a shift of 15-20 mm is observed in most typical COMPASS diverted discharges and is similar to observations in ASDEX Upgrade [49]. The average potential and its standard deviation within segments of 1 mm width are shown for clarity. The method of averaging ϕ^{BPP2} and ϕ^{BPP4} into $\phi^{\mathrm{BPP2\_4}}$ is in good agreement with the radial profile of ϕ^{BPP3} in the region near the maximum of the ϕ^{BPP} potentials. In the region more outwards close to $\Delta R = 33$ mm a secondary local maximum is present which could be caused by other plasma facing components creating a secondary limiter which would cast an asymmetric shade which may also be the cause of the slight discrepancy in the probe potential profiles in this region. The difference between the profiles of ϕ^{BPP3} and V_{fl}^{LP1} corresponds to the electron temperature T_e which increases towards the LCFS [26].

The estimated radial profile of the slow component of E_r is shown in the bottom panel in Figure 4.4 without errorbars as the lowpass-filtering removes

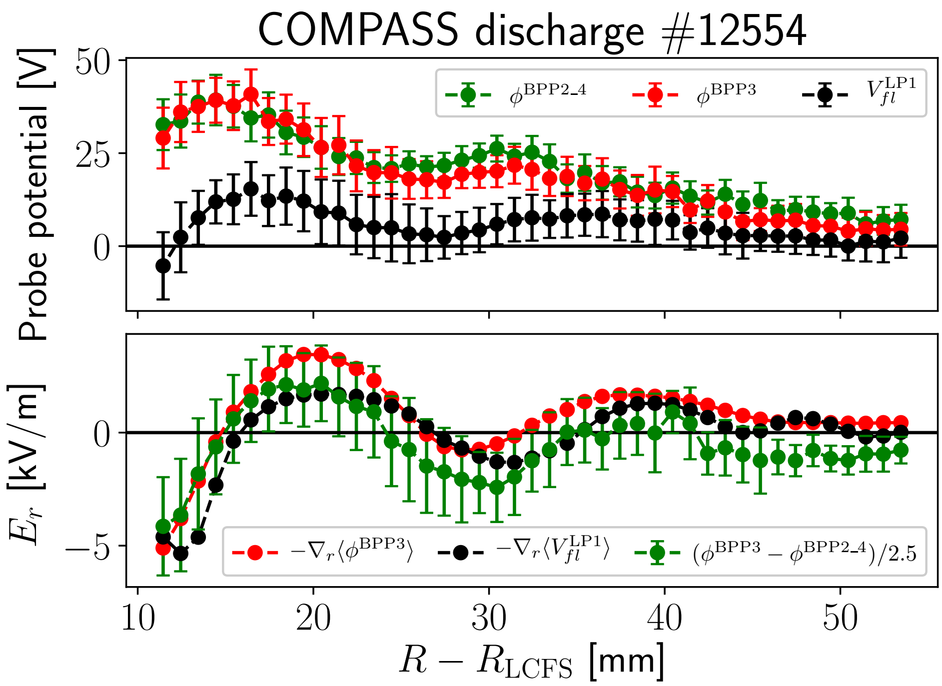

Figure 4.4: Floating potentials measured by LPs and plasma potentials measured by BPPs on the probe head in COMPASS discharge #12554 and calculated slow components of E_r. The x-axis is the radial distance on the midplane the from the last closed flux surface (LCFS).

fluctuations. The E_r estimate obtained from the difference of $\phi^{\mathrm{BPP2\_4}}$ and ϕ^{BPP4} (in the time domain) appears to correspond very well to the estimate obtained from the radial derivative of the slow component of ϕ^{BPP3} at least in the region close to the velocity shear layer near $\Delta R = 15$ mm. In the region more outwards close to $\Delta R = 33$ mm the E_r estimates suggest a presence of a secondary velocity shear layer related to the secondary potential profile maximum mentioned above, but the E_r estimates in this region are not reliable due to the discrepancy in the potential profiles in that region as discussed above. The estimate obtained from ϕ^{BPP3} is larger around $\Delta R = 20$ mm which may be due to E_r changing rapidly in that region which the probes separated radially by 2.5 mm may not be able to measure, because the probe-difference method assumes a constant gradient between them. This results in a limit of the spatial resolution of the probe-difference method.

The radial electric field obtained from the differentiation of V_{fl}^{LP1} is systematically lower by ~ 1 kV/m than the estimate obtained from ϕ^{BPP3}. This is due to the radial gradient of the electron temperature which corresponds to the growing difference between radial profiles of V_{fl}^{LP1} and ϕ^{BPP3}.

4.2.1 Comparison of the radial profiles of electric field fluctuations

The fluctuations of the radial E_r and poloidal E_p electric fields calculated from the probe-difference method are compared in Figure 4.5 in the top and bottom panel, respectively. The fluctuation level is quantified by the standard deviation of the fast measurements of E_r and E_p in each segment corresponding to segments in Figure 4.4, i.e. for E_r the displayed fluctuations correspond to the error bars in the bottom panel in Figure 4.4. The fluctuations of the radial electric fields std(E_r) in the top panel in Figure 4.5 are nearly the same for both ball-pen and Langmuir probes and they increase further inwards for either probe type.

However, the fluctuations of the poloidal electric fields std(E_p) in the bottom panel in Figure 4.5 are systematically lower for ball-pen probes in comparison with the Langmuir probes. The difference increases further inwards into the plasma, possibly due to the higher temperature and its fluctuations. Further experiments and simulations, which are beyond the scope of this thesis, will be necessary to fully investigate the reason for these differences.

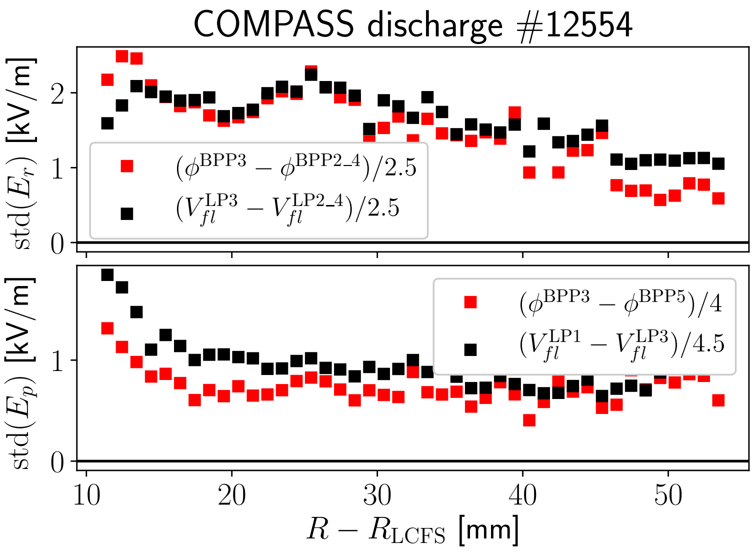

Figure 4.5: The radial profiles of the fluctuations of the radial and poloidal electric fields obtained from differences of ball-pen and Langmuir probes in COMPASS discharge #12554. The x-axis is the radial distance on the midplane the from the last closed flux surface (LCFS).

Chapter 5

Comparison of Reynolds stress profiles measured by Langmuir and ball-pen probes

As was already stated in subsection 3.2.3, on of the motivations for the construction of the new Reynolds stress probe head was to compare radial Reynolds stress profiles simultaneously measured by Langmuir probes (LP) and ball-pen probes (BPP). The differences and similarities between the profiles measured by either probe type are described in section 5.1. These measurements were performed with the original design of the Reynolds stress probe head described in subsection 3.2.3. An attempt to explain the observed differences is made in subsection 5.1.1 on the basis of the spectral composition of the Reynolds stress and decomposition of the Langmuir probe measurements into spectral contributions coming from plasma potential and temperature fluctuations.

5.1 Radial profiles of the Reynolds stress

The Reynolds stress should be calculated as the average of the product of velocity fluctuations over a flux surface $\langle \tilde{v}_r \tilde{v}_p \rangle$. This flux-surface average will be replaced in the following by a time average under the assumption that the underlying processes are ergodic. The average will be performed over timespans of ~ 1 ms corresponding to a radial resolution of ~ 1 mm due to the reciprocation speed being close to ~ 1 mm/ms. Figure 5.1 shows a comparison of radial profiles of the Reynolds stress obtained from velocity fluctuations calculated as the $E \times B$ drift velocities using the fluctuations of the corresponding electric fields obtained from the differences of BPP or LP and the toroidal magnetic field at the given probe position. The mean electric field component was removed with a 1 kHz highpass filter.

It is evident that the profiles are different for either probe type, even though their shape has similarities, e.g. the presence of local maxima around $\Delta R = 14$ mm and local minima around $\Delta R = 21$ mm. However, the Reynolds stress measured with BPPs exhibits a generally higher value in comparison with the LP measurements. This means that BPPs measure a higher level of correlation between the velocity fluctuations in comparison to the LP measurements.

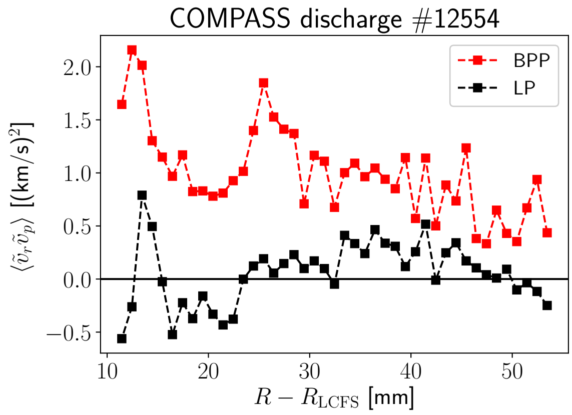

Figure 5.1: Comparison of radial profiles of the Reynoldds stress in COMPASS discharge #12554 obtained with BPP and LP.

The radial profiles of the Reynolds stress measured with LP multi-arrays on the ISTTOK tokamak [48] also show a positive peak of $\sim 1\,(\mathrm{km/s})^2$ several mm inside the LCFS and then they approach negative values further inside. Only a few values are shown outside the LCFS in the SOL, but they are also close to 0. Therefore, there is agreement between these profiles and the profiles measured by the LPs on the Reynolds stress probe head on COMPASS if the LCFS is taken at the maximum of the plasma potential. Similar agreement has been also found with radial profiles of the Reynolds stress measured with LPs on TEXTOR [44] where a peak of $\sim -1.5\,(\mathrm{km/s})^2$ was also found just inside the LCFS and the values in the SOL approached 0. The difference in the sign is probably due to a different velocity direction convention, otherwise the values and the profile shape generally agree with the COMPASS measurements. The peak (again with a different sign) near the LCFS was also observed on the IR-T1 tokamak [45] with LPs, but the lack of clear units in the article prevents a quantitative comparison.

5.1.1 Spectral composition of the Reynolds stress

Even though the velocities are calculated as the ratio of the poloidal or radial electric fields and the toroidal magnetic field B_ϕ, the magnetic field varies very little and thus contributes to the correlation of fluctuations negligibly and can be thought of as a multiplicative scaling factor for each point in the graphs. Therefore, only the correlations of electric field fluctuations and related quantities will be investigated in the following in order to simplify their interpretation.

The correlation of the velocity fluctuations over a given timespan $< t_1, t_2 >$ can be decomposed into a sum over their cross-spectral density components $C_{rp}(f) = \overline{V_r(f)} V_p(f)$ as defined in [50] with $V_r(f)$ being the Fourier image of $\tilde{v}_r(f)$ as can be seen by using the cross-correlation theorem for the 0-lag value of the cross-correlation function as detailed in [50]

$$\langle \tilde{v}_r(t)\tilde{v}_p(t)\rangle = \langle \tilde{v}_r(t)\tilde{v}_p(t+\tau)\rangle\Big|_{\tau=0} =$$
$$= \int \overline{V_r(f)} V_p(f)\exp(-i2\pi f\tau)df\Big|_{\tau=0} = \int C_{rp}(f)df$$

Only the real parts of $C_{rp}(f)$ are important for the result which is real, the imaginary part cancels out to zero (within numerical precision). The cross power spectra in each timespan are estimated by Welch's method [50] of averaging smaller sub-timespans, therefore, any noise with random phase cancels out to 0 and the estimated spectra contain only coherent frequency components. The mean spectral component $C_{rp}(0)$ is 0 due to the fluctuations having no mean value (it is removed by detrending each sub-timespan).

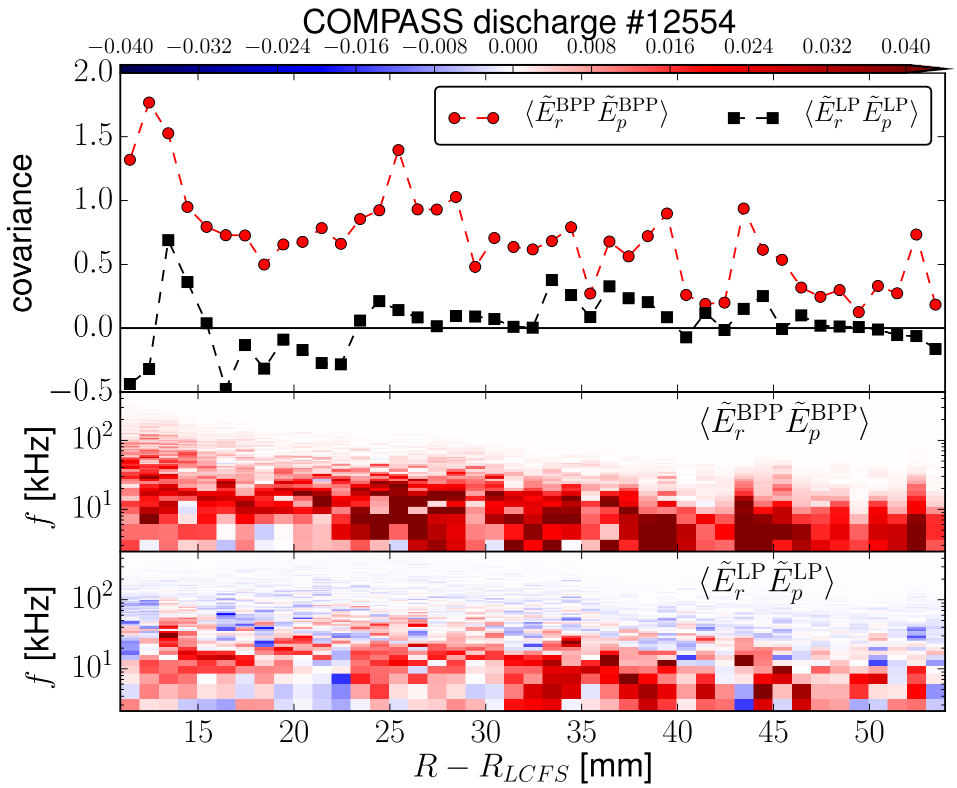

Figure 5.2: Radial profiles of the covariance of electric field fluctuation in COMPASS discharge #12554 and the spectral composition of the covariance.

In Figure 5.2 the correlations of electric field fluctuations for either probe type calculated for each radial position are decomposed into cross-spectral density frequency components. The data points are essentially the same as in Figure 5.1, but without the $1/B_\phi^2$ factor which would complicate the interpretation of the spectral contributions. For BPP the positive cross-correlation comes from lower frequencies ($f < 200$ kHz) and there appears little contribution for higher frequencies. In the case of LP the positive cross-correlation contributions also come from lower frequencies ($f < 50$ kHz) but are lower than in the case of BPP. However, higher frequencies represent negative contributions. Even though they are small, they are spread over a large frequency range (due to the logarithmic frequency axes in the figure) $f < 500$ kHz and thus represent a contribution comparable to the positive contributions which results in the much smaller and at some positions negative Reynolds stress estimate for LP in comparison with BPP.

Under the assumption of $\alpha_{\text{BPP}} \approx 0.6$ and $\alpha_{\text{LP}} \approx 2.8$ as used in [43] the radial and poloidal gradients of electron temperature and the plasma potential fluctuations $\tilde{T}_e$, $\tilde{\phi}$ can be approximated as linear combinations of the electric fields for both probe types, i.e. by applying gradients to (3.4) to obtain ∇T_e and then calculating $\nabla\phi = \nabla\phi^{\text{BPP}} + 0.6\nabla T_e$. Such estimation of the $\nabla\tilde{\phi}$ and $\nabla\tilde{T}_e$ can offer only a limited frequency resolution due to the finite distances between the probes. The dispersion relation of potential fluctuations was calculated for each probe type using Beal's method [51] and the high frequency limit was found to be ~ 300 kHz for BPP and ~ 500 kHz for LP. This estimation then enables a comparison of the correlation terms contributing to the Reynolds stress estimate obtained with LP

$$
\begin{aligned}
\langle \tilde{E}_r^{\text{LP}} \tilde{E}_p^{\text{LP}} \rangle &= \langle \partial_r(\tilde{\phi} - \alpha\tilde{T}_e)\partial_p(\tilde{\phi} - \alpha\tilde{T}_e)\rangle = \\
=&\langle \partial_r\tilde{\phi}\partial_p\tilde{\phi}\rangle - \alpha\langle \partial_r\tilde{T}_e\partial_p\tilde{\phi}\rangle - \alpha\langle \partial_r\tilde{\phi}\partial_p\tilde{T}_e\rangle + \alpha^2\langle \partial_r\tilde{T}_e\partial_p\tilde{T}_e\rangle
\end{aligned}
$$

The four terms and their spectral decomposition are shown in Figure 5.3. The $\langle \partial_r\tilde{\phi}\partial_p\tilde{\phi}\rangle$ term is essentially the same as $\langle \tilde{E}_r^{\text{BPP}} \tilde{E}_p^{\text{BPP}} \rangle$ but is a little smaller, the frequency composition is also similar. This is due to the calculated true plasma potential ϕ being close to the potential measured with BPPs ϕ^{BPP} since the $\alpha_{\text{BPP}} = 0.6$ coefficient is quite small. The other terms have significantly different contributions in the outside and inside of $\Delta R \approx 17$ mm. Outwards for $\Delta R > 17$ mm the negative $-\alpha\langle \partial_r\tilde{T}_e\partial_p\tilde{\phi}\rangle$ term mostly cancels out with the $\alpha^2\langle \partial_r\tilde{T}_e\partial_p\tilde{T}_e\rangle$ terms, in both cases these major contributions come from lower frequencies, but the higher frequencies also have negative contributions, especially in the latter case. The $-\alpha\langle \partial_r\tilde{\phi}\partial_p\tilde{T}_e\rangle$ term has a smaller negative contribution stemming mostly from lower frequencies.

Further inwards $\Delta R < 17$ mm the two terms $-\alpha\langle \partial_r\tilde{T}_e\partial_p\tilde{\phi}\rangle$ and $\alpha^2\langle \partial_r\tilde{T}_e\partial_p\tilde{T}_e\rangle$ again have opposite contributions, but with the opposite polarity. However, the $-\alpha\langle \partial_r\tilde{\phi}\partial_p\tilde{T}_e\rangle$ term represents a large negative contribution. The major contributions come also from slightly higher frequencies ($f < 200$ kHz) in this region. The negative contributions from higher frequencies are most powerful in the $\alpha^2\langle \partial_r\tilde{T}_e\partial_p\tilde{T}_e\rangle$ term.

All the significant frequency contributions in all terms are consistent with the frequency limit estimated by Beal's method.

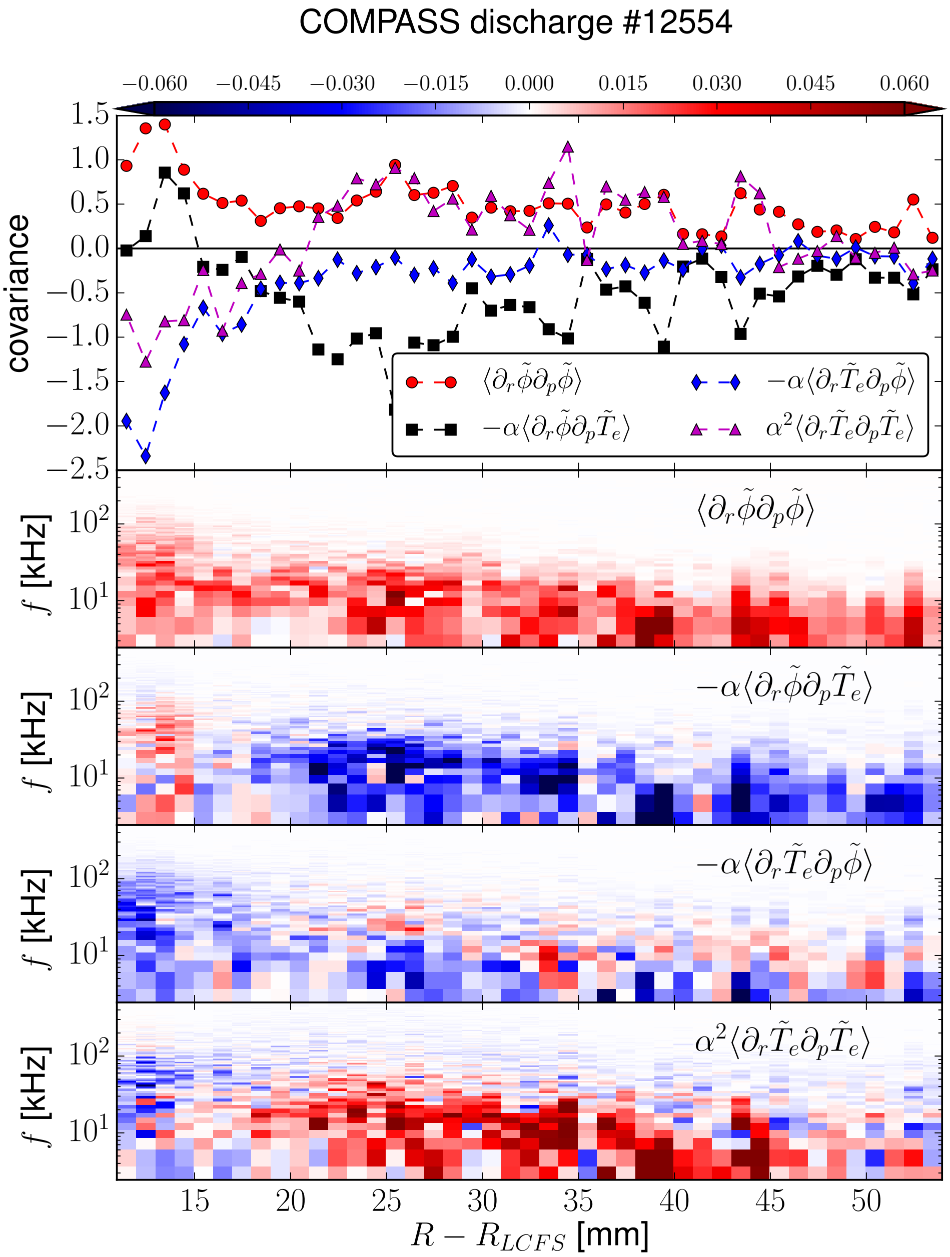

Figure 5.3: Radial profiles of the covariance contributions of radial and poloidal derivatives of temperature $\tilde{T}_e$ and potential $\tilde{\phi}$ fluctuations to the covariance of LP electric fields in COMPASS discharge #12554 and the spectral composition of the covariance.

Chapter 6

Oscillation measurements close to the L-H transition

The modified Reynolds stress probe head described in subsection 3.2.4 was used to investigate 3-5 kHz oscillations often observed during the L-H transition on the COMPASS tokamak. These oscillations are visible on the H_α signal evolution, but have a distinct signature on many other diagnostics as well, including magnetics, electrostatic probes positioned on either reciprocating probe heads or embedded in divertor tiles. Their quite high frequency and lower H_α amplitude in comparison to typically observed ELMs and their occurrence only during the L-H transition suggests that this phenomena may be LCO as described in section 2.4. Therefore, this mode was given a working title cLCO for "candidate limit cycle oscillations". Other possible hypotheses are that these either are type-III ELMs, or that that these two phenomena are driven by similar mechanisms as was suggested by recent LCO investigations on ASDEX Upgrade [31].

The purpose of this study was to measure the evolution of turbulence intensity, temperature, density and electric fields during these oscillations. The radial electric field E_r and its radial gradient was of particular interest, because the associated poloidal $E \times B$ velocity is expected to be responsible for shearing poloidal flows.

6.1 Scenario development and experiment plan

Two experimental campaigns were performed in order to investigate this phenomena. The first campaign `CC16.08` was partially successful in demonstrating the possibility of developing a discharge scenario where these oscillations were sustained with quite a stable frequency during the whole plasma current flat-top. The scenario development was conducted during the first week of the campaign and optimal discharge parameters were found, i.e. plasma shape and position, density and plasma current set-points. However, the following week the second part of the campaign it was discovered that the vessel wall conditions have changed significantly and the previously developed scenario did not deliver results seen in the first week. Furthermore, the initial reciprocation tests with the original Reynolds stress probe head (described in subsection 3.2.3) showed that the plasma was significantly perturbed by the probe, often leading to disruptions or to the mitigation of cLCO. Additionally, another mode with a similar frequency ~ 6 kHz appeared to be also modulating various signals which further complicated the analysis.

Therefore, another experimental campaign `CC17.11` was conducted with several key modifications to the campaign plan: Firstly, the vessel wall was boronized a day before the campaign started in order to reduce the out-gassing of impurities from the wall and thereby stabilize its effect on the L-H transition threshold. Secondly, the X-point height was set rather low ~ 1 cm above the divertor, because experiments in preceding campaigns showed that the other ~ 6 kHz mode did not appear when the X-point was low. Finally, the modified Reynolds stress probe head described in subsection 3.2.4 was used which was expected to reduce the rate of impurity out-gassing from the probe perturbing the plasma due to the different type of boron nitride.

These key changes were successful in enabling the development of a stable and well reproducible discharge scenario with the cLCO mode clearly observable during the whole flat-top phase of the discharge. This scenario was developed during the first day of the campaign with the standard toroidal magnetic field $B_\phi = 1.15$ T and plasma current $I_{pl} = 190\,\mathrm{kA}$ and density set-point $n = 5.5 \times 10^{19}\,\mathrm{m}^{-3}$. The only difficulty was the density feedback control system which resulted in slightly oscillating plasma density. This was likely caused by the radial plasma position oscillating which changed the interferometer chord length and led to oscillating density measurements to which the feedback system reacted with a certain time delay by changing the gas-puff rate. This issue was partially corrected by setting limits for the gas-puff rate at certain time intervals.

During the second day the modified Reynolds stress probe head mounted on the midplane horizontal reciprocating manipulator (HRCP) was used to measure the cLCO dynamics in terms of plasma and floating potential and ion saturation current inside the LCFS. The Langmuir probe `LP1` was used to measure the ion saturation current and was biased to $-270\,\mathrm{V}$, all the other probes were in floating regime. Unfortunately, the electronics measuring the radial location of the reciprocating manipulator head exhibited significant noise and the starting position was known only with an accuracy of ~ 0.5 cm. This greatly complicated the preparation of the reciprocation trajectory and often led to the probe head not reaching the LCFS or going too far beyond it which led to arcs on the Langmuir pins measuring ion saturation current and mitigated the cLCO mode. Nevertheless, it was possible to execute 2 discharges #13925 and #13926 where the HRCP was only ~ 5 mm inside the LCFS and no arcs developed and the cLCO mode was sustained.

The third day of the experimental campaign a slow L-H transition scenario was developed from the original scenario by slowly ramping up the plasma current from ~ 170 kA to ~ 250 kA. Due to the complicated HRCP position setting it was quite hard to achieve proper timing and depth of the reciprocating trajectory which would catch the plasma at the L-H transition while the probe head was inside the LCFS without arcs mitigating the L-H transition.

In the end, only one discharge #13963 was successful in fully achieving this very time and position sensitive goal.

Altogether, the number of fully successful discharges may seem rather small, but in the light of the complicated experimental goals and the sensitivity of the experiment to slight changes in conditions it is a big achievement and opens doors for future experiments extending this topic of research.

6.2 Conditionally averaged dynamics of oscillations

The cLCO oscillations were quite stable (in terms of frequency) in discharges #13925 and #13926 and this presents an opportunity to gather statistics on the evolution of various quantities during the oscillations. However, the oscillations are not completely periodic, their frequency and phase shift slightly fluctuate, and therefore they cannot be simply averaged over successive periods. Instead, the conditional averaging method was used to gather periods of these oscillations for statistical analysis.

In general, the conditional averaging method assigns a phase of the underlying oscillating process to each data point in the measured signals. This results in a statistical ensemble of points for each phase of the oscillation. Then the average, standard deviation and other statistical moments can be taken over the ensembles in order to estimate the average value and dispersion of various quantities at each phase of the oscillation.

A simple way to assign such phase coordinates to each data point is to select fixed-width periods of each signal around specified “trigger” points and align them according to their relative position with respect to the trigger points. The trigger points should represent a fixed phase of the oscillation in order to assign a specific phase to the surrounding points. This approach is viable when the period of the oscillations does not change very much, but their starting time is not clear. This is likely the case of the observed cLCO.

For the analysis presented here the maximum of the H_α signal was chosen as the trigger signal, because it is believed to be independent of the radial position of the probe head and is undoubtedly correlated with the oscillations observed by the probes. There is a little time delay $\sim 50\,\mu\mathrm{s}$ between the maxima on the H_α signal and the apparent maxima on the measured I_{sat}^+ signal. This is probably due to the radial propagation of the turbulent structures from the probe head to the wall where they may cause the peak in light emission, and possibly also due to the diagnostic measuring this light emission being located on the HFS whereas the HRCP is located on the LFS. Nevertheless, the time delay should not be an issue as long as the light emission maxima correspond to some fixed phase of the oscillation, which is assumed. The fixed window length of 0.2 ms around the trigger points was used, because the power spectral density of the v_r, n and H_α signal oscillations exhibited a peak around ~ 5 kHz. The H_α signal was lowpass-filtered to 50 kHz in order to remove high-frequency noise which could complicate finding the maxima.

Before averaging all the signals were decimated (i.e. lowpass-filtered to new Nyquist frequency and then downsampled) to a sampling frequency of 1 MHz, because the power spectral density of the above mentioned signals showed a drop-off above 500 kHz and no significant physical fluctuations are expected beyond these frequencies. This step also reduces the noise which the averaging attempts to smooth out and which might be too strong otherwise for the limited statistic to fully mitigate.

The density n was estimated from the measured ion saturation current $I_{sat}^{+,\mathrm{LP1}}$ using formula (3.1) with the assumption $T_e \approx T_i$ and $Z = 1$. The probe area A was taken to be the whole surface of the Langmuir probe exposed to the plasma, i.e. $A = \pi h d + 0.25\pi d^2$ where $h = 1.5\,\mathrm{mm}$ is the height of the part of the probe protruding into the plasma and $d = 0.9\,\mathrm{mm}$ is its diameter. This density estimate gives only a very crude estimate of the density as the assumptions used could not be easily verified. The radial and poloidal electric fields E_r and E_p were calculated using combinations of probes described in subsection 3.2.4. The corresponding poloidal and radial $E \times B$ drift velocities, respectively, were calculated as the ratio of the respective electric field component to the toroidal magnetic field taken from the magnetic reconstruction at the radial probe head position at each given time. Since the radial position of the probe head was not known very accurately, the used magnetic field may have been inaccurate as well, however, on the LFS the toroidal magnetic field varies little over ~ 0.5 cm and this issue is likely negligible.

The radial distance of the reciprocating probe head from the LCFS $\Delta R = R - R_{\mathrm{LCFS}}$ could not be simply calculated by only subtracting subtracting the radial position of the LCFS given by the magnetic reconstruction, because the radial position of probe head at any given time had very low accuracy due to the position measurement noise. However, it was assumed that the measurement noise result only in a constant offset of the initial reciprocation position. Therefore, the LCFS position given by the magnetic reconstruction was first subtracted from the radial reciprocating position to get $\Delta\hat{R}$ and then the profile of the plasma potential measured by `BPP2` was plotted and the $\Delta\hat{R}$ position of the maximum of the plasma potential was subtracted from $\Delta\hat{R}$ in order to get the corrected ΔR.

The conditional averaging was performed over a timespan from 1160.5 to 1196.8 ms when the probe head was inside the LCFS. There were about 170 cLCO events during that timespan. This timespan was further divided into two sub-intervals, each corresponding to a different average radial position $\Delta R = -1.5 \pm 0.6$ mm and $\Delta R = -3.4 \pm 0.6$ mm. Each of these regions included about $N \sim 80$ cLCO events. The result of averaging several quantities over the conditionally selected periods is shown in Figure 6.1. The line-plotted waveforms represent the conditional average (mean) value and the semi-transparent filling around represents the standard error of the mean as defined in [52], i.e. the standard deviation divided by $\sqrt{N}$.

The left plots show from top to bottom the evolution of the standard deviation of the density std(n), the poloidal velocity v_p, the Reynolds stress $\langle\tilde{v}_p\tilde{v}_r\rangle$, the density n, the electron temperature T_e and the electron pressure p_e. The fluctuations of the velocities were obtained by a 10 kHz lowpass filter (in order to remove the cLCO trends) of the raw v_r, v_p signals and the averaging $\langle\rangle$ was performed through the conditional averaging under the assumption of ergodicity. The electron pressure was estimated as $p_e \approx \frac{3}{2}k_B T_e n$ and its standard deviation was estimated through the sum of relative deviations of T_e and n. The obtained values of T_e, n and p_e are within the orders of magnitude observed by the Thomson scattering system just inside the LCFS.

The right plots with the exception of the exception of the top one show the negative of the radial gradient of the quantities to the left. The negative of the radial gradient $-\partial_r$ is shown because most of these quantities have a negative radial gradient inside the LCFS and this manner of display is easier to comprehend in terms of the gradient becoming steeper or flattening. The radial gradient was estimated from the difference of the waveforms on the left plots and was divided by their average radial distance. The standard deviation was again estimated through the sum of relative deviations rule. The first plot shows the turbulent flux $\Gamma = \langle\tilde{n}\tilde{v}_r\rangle$ where the fluctuations and averaging was performed in the same way as with the Reynolds stress. The second plot shows the shear of the poloidal velocity $-\partial_r v_p$, the third plot shows the Reynolds stress force $-\partial_r\langle\tilde{v}_p\tilde{v}_r\rangle$. The fourth to sixth plots show the negative radial gradients of the density, electron temperature and pressure, respectively. From the radial gradient of the electron pressure and the average density the electron diamagnetic drift velocity v_{*e} was estimated using formula (2.6) and it was plotted in the second plot from the top on the left side. The large error filling around this velocity is due to the combination of the standard error estimates of the density and the electron pressure.

Figure 6.2 shows the result of the same procedure for COMPASS discharge #13926 for the timespan from 1158.9 to 1200.4 ms. The resulting averaged waveforms correspond to those in Figure 6.1 very well.

Interpretation of the conditionally averaged oscillation dynamics

Within the conditionally averaged window of 200 µs, the dynamics of the conditionally averaged quantities show significant oscillations during the cLCO cycle and radial variation for both analyzed discharges.

The displayed waveforms start at a relative cycle time scale $t = 0$ µs in a state of relatively low turbulence intensity quantified by std(n). The turbulence intensity is higher closer to the LCFS than deeper inside. This may be due to the poloidal velocity shear $-\partial_r v_p$ being quite large at this point only deeper inside the LCFS where it decorrelates turbulent structures at a higher rate. The Reynolds stress is quite small and the radial gradients of v_p, n, T_e and p_e are quite large and mostly stationary. In discharge #13925 in Figure 6.1 there is a hint of the gradients slowly decreasing, in discharge #13926 in Figure 6.2 this is not clearly visible. However, in both discharges these quantities are apparently slowly decreasing at this phase, mostly deeper inside the LCFS. This may be caused by the finite level of turbulence.

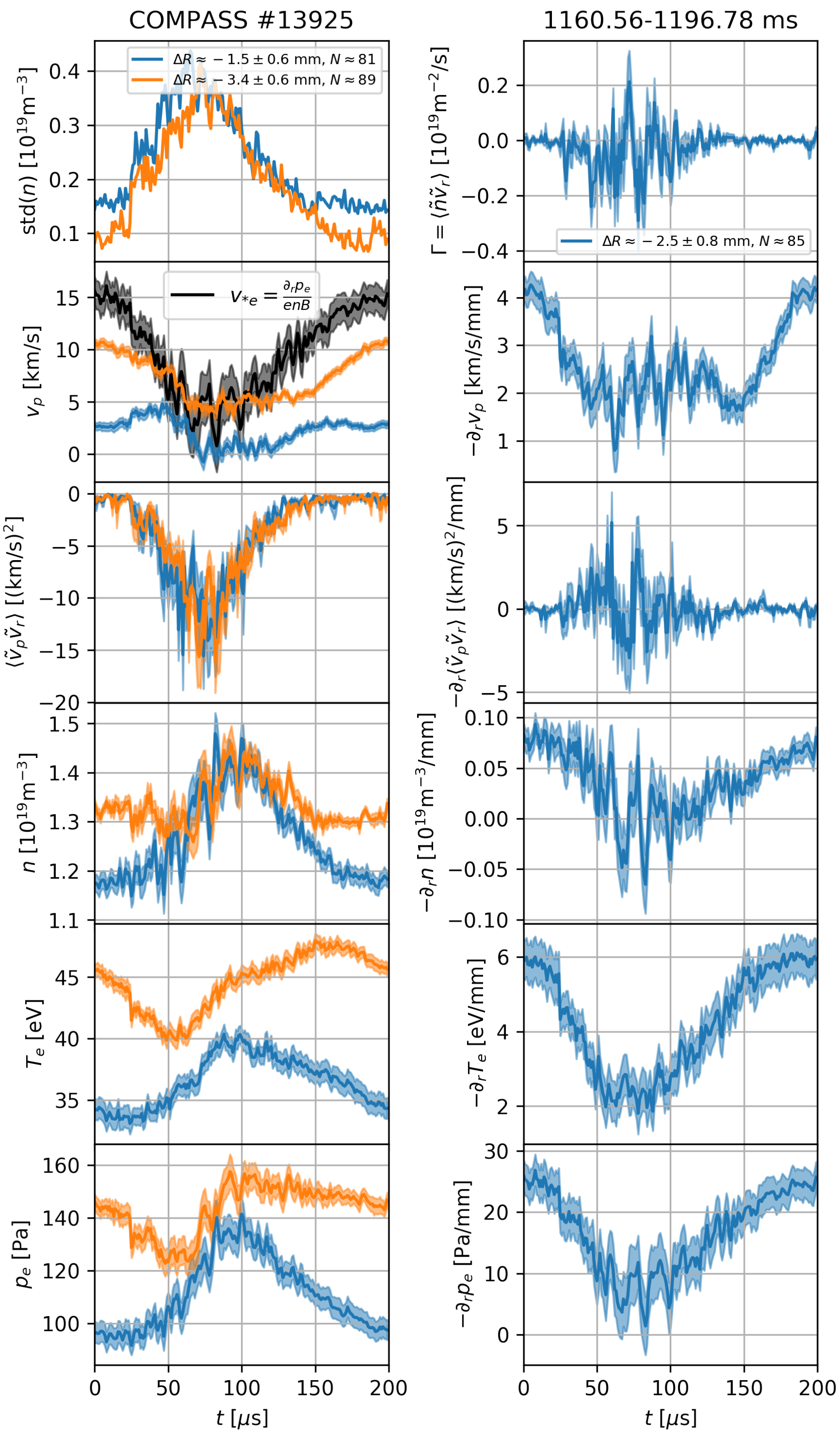

Figure 6.1: Conditionally averaged dynamics of various quantities during cLCO in COMPASS discharge #13925. The waveforms represent the conditionally averaged mean values and the semi-transparent filling around them represents the standard error of the mean. The orange waveforms on the left correspond to the evolution deeper inside the LCFS (ΔR is the distance from the LCFS) and the blue ones closer to the LCFS. t is the relative time scale of the averaged cLCO cycle.

Then around $t \sim 25\,\mu s$ the turbulence intensity quickly increases and all the previously mentioned radial gradients quickly fall which is apparently caused by the quantities deeper inside the LCFS decreasing while they increase closer to the LCFS. This could be interpreted as the radial profiles flattening from the core towards the edge. The Reynolds stress begins to increase (in absolute value) during this phase. The turbulence intensity is still slightly larger closer to the LCFS and in #13925 it appears the intensity remains constant up to $t \sim 40\,\mu s$. Until this time the radial gradients gradually become flatter as the values of the quantities closer to the LCFS and further away from the LCFS approach some value in between.

Around $t \sim 55\,\mu s$ the quantities and their radial gradients reach their lowest values while the turbulence intensity continues to grow. The density gradient becomes almost completely flat as the density at both radial locations approaches similar values. After this time the n, T_e and p_e begin to grow at similar rates both deeper and closer to the LCFS which results in the radial gradients remaining at the low values. This suggests that the core plasma is being "ejected" into the edge while the profile is further flattened. The poloidal velocities instead begin to decrease at similar rates, maintaining the low value of their shear. The Reynolds stress force appears to be slowing down v_p in discharge #13926. Unfortunately, in discharge #13925 the Reynolds stress values are too close for their radial gradient to be reliable.

At $t \sim 70\,\mu s$ the turbulence intensity and the Reynolds stress reach their largest (absolute) values at both radial locations and start decreasing afterwards. The turbulence intensity is the same at both radial locations, suggesting that this is the fully turbulent state. The poloidal velocities reach their lowest values at both radial locations and so does their shear. The low shearing rate appears to be correlated with this fully turbulent state.

After $t \sim 90\,\mu s$ the quantities n, T_e and p_e stop increasing closer to the LCFS and start decreasing. Their values deeper inside the LCFS also start decreasing at a lower rate with the exception of T_e, which continues to increase. This results in their radial gradients beginning to increase. This suggests that the profiles begin to recover with the gradient in the core increasing after being flattened in the previous phases. The value of v_p deeper inside the LCFS appears to slightly rise after this time which leads to a slight increase in the $-\partial_r v_p$ shear, but it is not entirely clear due to the large error.

After $t \sim 110\,\mu s$ the value of v_p begins to increase also closer to the LCFS at a similar rate as inside the LCFS. Around $t \sim 130\,\mu s$ the rate of the v_p rise closer to the LCFS appears to temporarily exceed the v_p rise rate deeper inside the LCFS, resulting in a temporary dip of the v_p shear. The negative Reynolds stress force in both discharges at this phase may be the cause of this temporary dip, but its estimate is not very reliable due to the large error. After $t \sim 140\,\mu s$ the value of v_p begins to increase at an even higher rate deeper inside the LCFS while the value closer to the LCFS stagnates. This leads to a sustained growth of the velocity shear up to the end of the cycle window. The Reynolds stress is almost 0 at this point and likely has no effect on this rise. The electron temperature T_e reaches its maximum deeper inside the LCFS around $t \sim 160\,\mu$s and begins to decrease and its radial gradient stagnates at its maximum value.

The electron diamagnetic drift velocity estimate v_{*e} appears to correspond well to the v_p waveform deeper inside the LCFS. This suggests that the radial electric field is determined mostly by the pressure gradient as predicted by the radial force balance (2.12).

Altogether, the averaged waveforms suggest that the fall of the radial electric field E_r and the associated v_p velocity and its shear is caused by the flattening of the pressure profile due to the turbulence and later also by the ejection of the core plasma into the edge. The turbulence level begins to decrease before the velocity shear begins to significantly increase and there is little evidence that the Reynolds stress force significantly contributes, even though the Reynolds stress does rise to substantial values and some zonal flow excitation is possible. However, the poor accuracy of the relevant waveforms obtained through this method prevents a conclusive interpretation. Furthermore, the poloidal velocity v_p and its shear reach their lowest (absolute) values when the turbulence intensity reaches its maximum, which points towards a π phase shift between the two, rather that the $\pi/2$ typical for LCO as explained in section 2.4. Instead, the observed dynamics is more consistent with the ELM dynamics, where the pressure profile collapses and plasma is ejected into the edge, after which the pressure profile pedestal begins to recover. Alternatively, the dynamics could be compared to that of type-J LCO observed on HL-2A [32] where the E_r modulation seemed to be related more to the pressure gradient.

Possible future improvements to the conditional averaging method by spline-fitting radial profiles

Due to the significant radial variation of the conditionally averaged waveforms in the preceding section 6.2 it is possible that a more general conditional averaging approach is necessary which would not average all oscillations within some radial location interval, but instead would fit the whole radial profile of quantities at each phase of the oscillation. This more general approach could also use the generalized instantaneous phase of the oscillation obtained by the Hilbert transform in order to account for fluctuations in both frequency and phase.

For this purpose the instantaneous phase could be calculated as the angle of the complex analytic signal of the bandpass-filtered H_α signal to 2-6 kHz using the Hilbert transform [50]. The quantities measured by the probes at each time and oscillation phase could then fitted with 2D B-splines with the H_α instantaneous phase and immediate radial location of the probe at the time of the measurement as the x and y coordinates, respectively. The fitted splines could then be interpolated on a rectangular grid and displayed along with the radial derivative of the fitted splines.

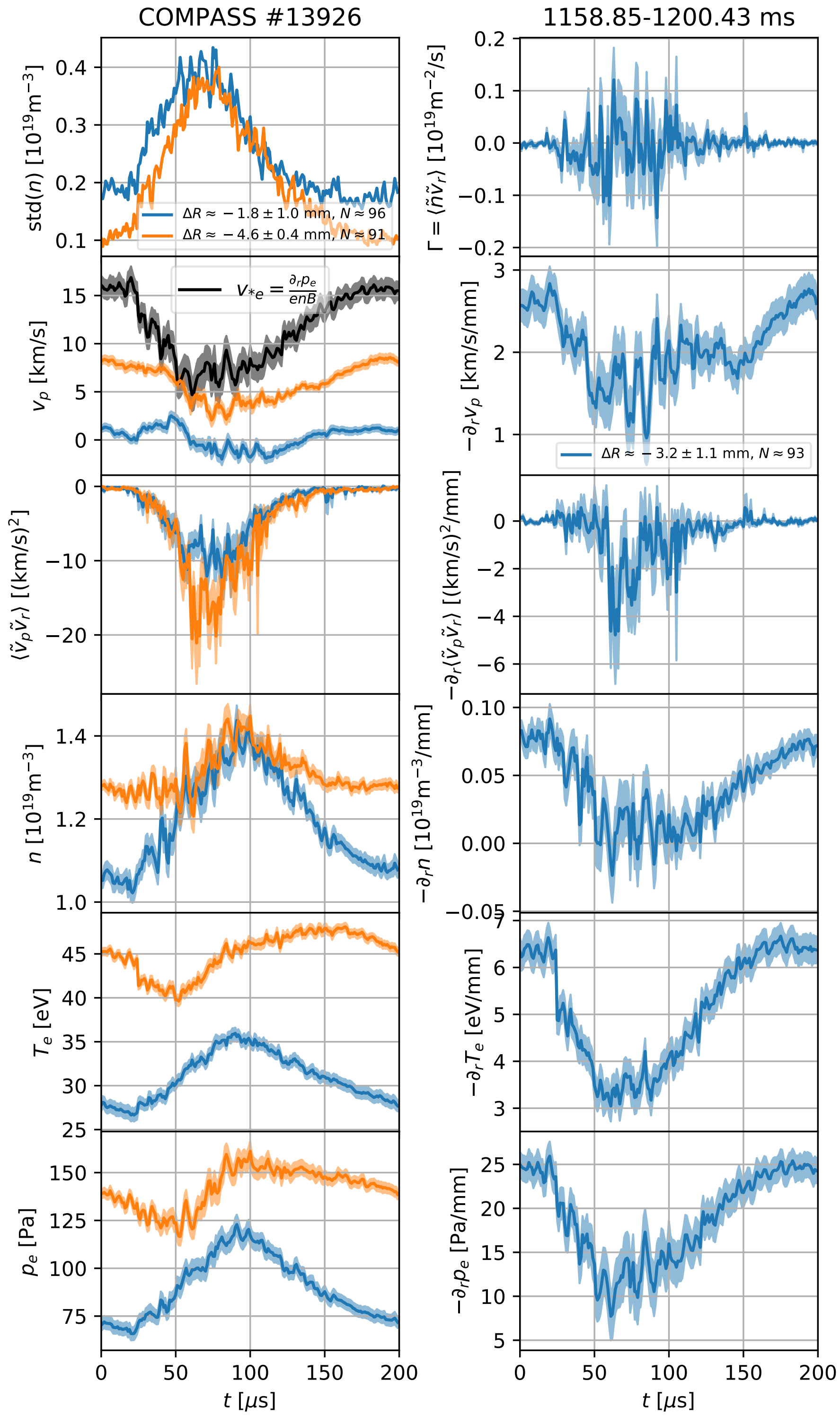

Figure 6.2: Conditionally averaged dynamics of various quantities during cLCO in COMPASS discharge #13926. The waveforms represent the conditionally averaged mean values and the semi-transparent filling around them represents the standard error of the mean. The orange waveforms on the left correspond to the evolution deeper inside the LCFS (ΔR is the distance from the LCFS) and the blue ones closer to the LCFS. t is the relative time scale of the averaged cLCO cycle.

6.3 Cross-phase analysis of the density fluctuations envelope and electric field oscillations

The phase between the cLCO oscillations of the density n and the radial electric field E_r was investigated using the Hilbert transform in a similar manner as done on HL-2A [30]. The analysis was performed only for the timespan during which the probe head was inside the LCFS. The Hilbert transform is used to construct a so called complex analytic signal $a(t) = A(t)\exp(i\varphi(t))$ which represents oscillations with an instantaneous phase $\varphi(t)$ with a slowly varying envelope amplitude of the signals $A(t)$. The analytic signal has good meaning only if the oscillations have a sufficiently narrow frequency band for the instantaneous phase to be meaningful. Therefore, the E_r signal was low-passed to 6 kHz in order to represent the phase of the general trend of the E_r strength corresponding to the poloidal velocity v_p. The envelope of the density fluctuations corresponding to the turbulence intensity was estimated by applying a similar 6 kHz low-pass filter to the absolute value of highpass-filtered above 50 kHz density fluctuations δn. Then the analytic signal was calculated for both signals and the difference of their instantaneous phases was plotted in Figure 6.3.

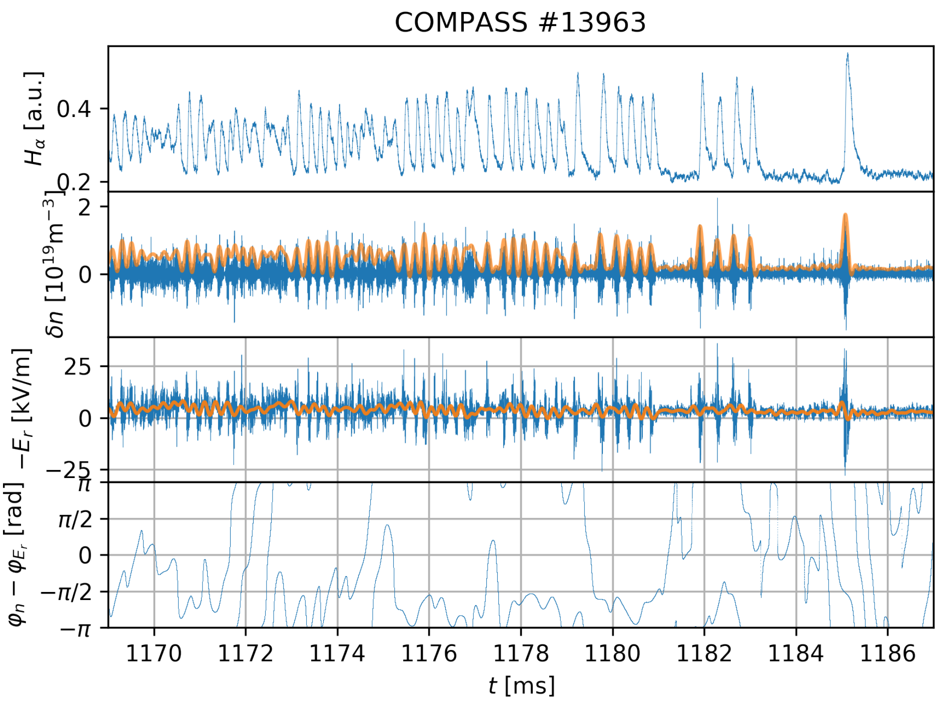

Figure 6.3: Evolution of the H_α signal, density fluctuations δn and radial electric field E_r and the cross-phase between the slow E_r component (orange in E_r plot) and the envelope of the density fluctuations (orange in δn plot) during the L-H transition in discharge #13963.

The cross-phase displayed in that figure between the density fluctuations envelope and E_r is in the range of $-\pi$ to $-\pi/2$ during periods of clear cLCO oscillations. This suggests that the turbulence intensity rises in response to the E_r strength decreasing and may even be anti-correlated which corresponds to the cross-phase $-\pi$, i.e. the density fluctuates the most when the radial electric field is closest to 0 kV/m. This can be seen in greater detail in Figure 6.4 where E_r visibly decreases and then the density fluctuation intensity rises. Once the fluctuation intensity decreases, the E_r field begins to recover. This is in line with the observations in section 6.2 where E_r seemed to fall due to the collapse of the pressure gradient due to an outburst of turbulent structures.

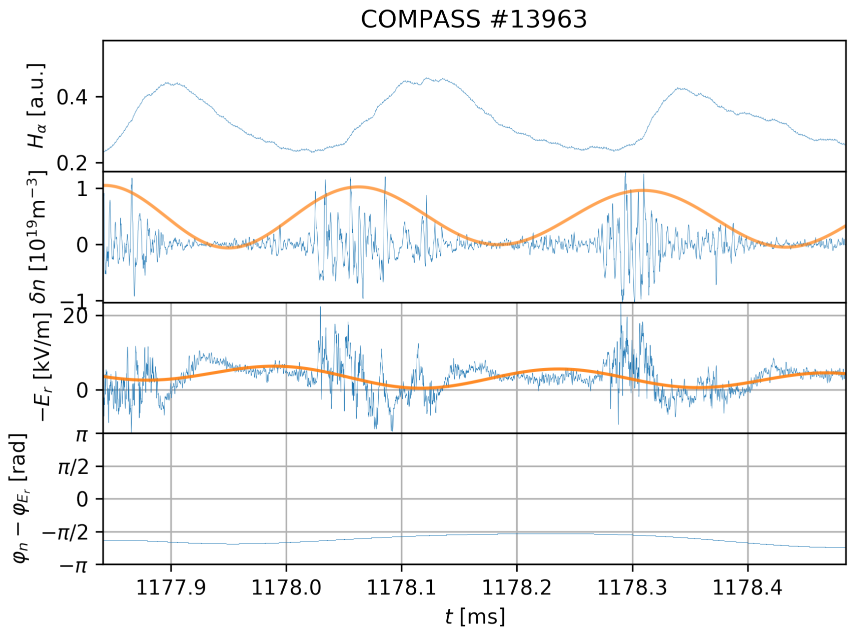

Figure 6.4: Detail of the H_α signal, density fluctuations δn and radial electric field E_r and the cross-phase between the slow E_r component (orange in E_r plot) and the envelope of the density fluctuations (orange in δn plot) during several cLCO cycles in discharge #13963.

It is also clear from Figure 6.4 that this simplified, low-frequency analysis does not fully capture the complicated patterns of oscillations of E_r and δn. For example, the large oscillations of δn while the fluctuation envelope is the largest appear to be correlated with E_r oscillations on a similar time scale. These could be filamentary structures passing over the probe.

The corresponding cycle-like behavior is illustrated in Figure 6.5 as a Lissajous curve of the envelope of δn versus the low-frequency component of E_r. The cycles progress in a counter-clockwise fashion because of the $\approx -\pi/2$ phase shift, i.e. the $\delta n \sim \sin(t)$ envelope lags behind $E_r \sim \cos(t)$ by $\approx \pi/2$ which gives rise to the almost circular motion.

The timespan around the last large peak on the H_α signal shown in Figure 6.3 which likely is an ELM is also shown in detail in Figure 6.6. The high-frequency patterns appear to be similar in some respects to those of cLCO shown in Figure 6.4, but the ELM appears to have a quite long pre-

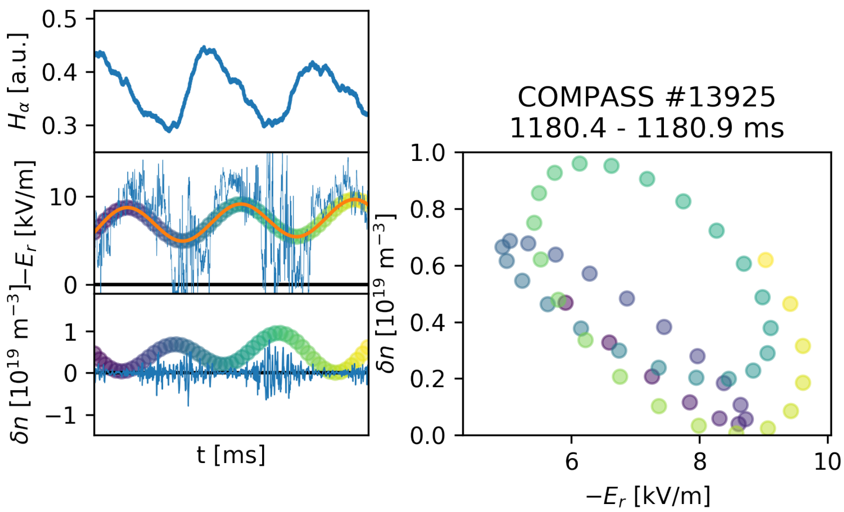

Figure 6.5: Evolution of the H_α signal, radial electric field E_r and density fluctuations δn and their envelope during several cycles of cLCO. The color-coded (time progresses from darker to lighter colors) low-frequency component of E_r and of the δn envelope in the left plots shown as a Lissajous curve in the right plot.

cursor phase of periodic δn oscillations before the large fluctuations take place. The E_r field also drops to much lower values than in the case of cLCO. Altogether, the cLCO seem to have some dynamics in common with ELMs, but fluctuation amplitudes are smaller.

6.4 Bicoherence analysis of plasma potential oscillations

The plasma potential measured by `BPP2` (i.e. neglecting T_e fluctuations) was analyzed using the method of bicoherence. The purpose of this method is to detect three-wave interaction, i.e. energy transfer between frequency modes f_1, f_2 and $f_1 + f_2$ which can occur due to nonlinear processes. The motivation for this analysis is the predicted nonlinear three-wave interaction leading to the generation of zonal flows by turbulence as was explained in subsection 2.2.2. Such interaction should result in the phases of these modes being locked $\varphi_1 + \varphi_2 - \varphi_{1+2} = const$. Since two modes with a locked phase (i.e. a constant phase shift) are called coherent, three modes with locked phases are called bi-coherent.

Therefore, the bicoherence analysis method is an extension of the standard cross-coherence method which attempts to detect coherent (i.e. with a constant phase shift) frequency modes in two distinct signals. The cross-coherence squared $\gamma(f)^2$ between modes at frequency f in signals x and y is defined as the ratio of the squared magnitude of the cross-spectral density $|C_{xy}(f)|^2$ defined in [50] and used in subsection 5.1.1 and the product of the

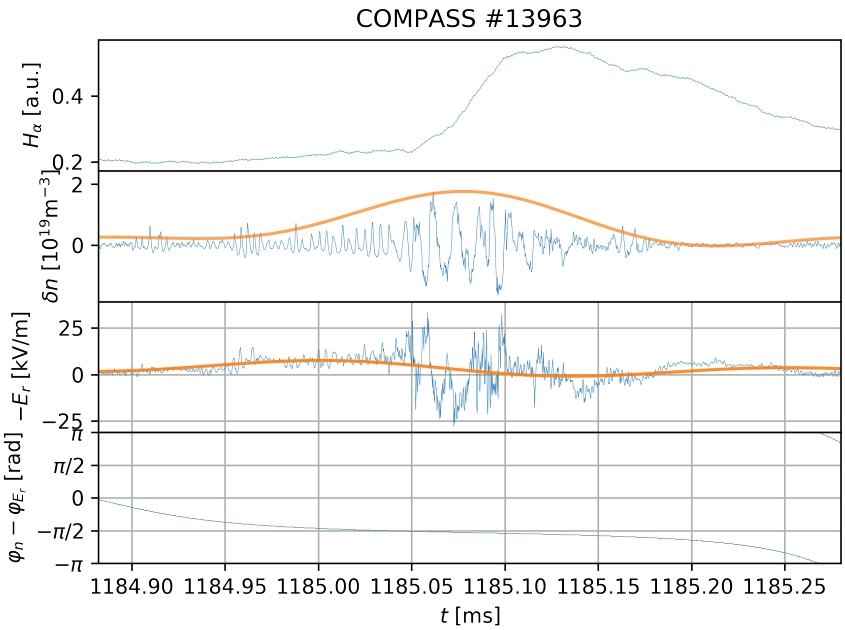

Figure 6.6: Detail of the H_α signal, density fluctuations δn and radial electric field E_r and the cross-phase between the slow E_r component (orange in E_r plot) and the envelope of the density fluctuations (orange in δn plot) during an ELM-like peak in discharge #13963.

auto-spectral densities of either signal $C_{xx}(f)C_{yy}(f)$ which are both real. The cross- and auto-spectral densities are estimated by averaging sample cross- and auto-spectra over an ensemble of such spectra usually obtained by a short-time discrete Fourier transform. The averaging reduces non-coherent spectral components with a random phase shift to 0, while the coherent components with a constant phase shift stand out and the division by the auto-spectral densities normalizes them to the interval $(0, 1)$.

Bicoherence extends this by using the bispectrum $B(f_1, f_2)_{xy} = \langle \bar{Y}(f_1 + f_2)X(f_1)X(f_2)\rangle$ where $X(f)$ and $Y(f)$ are the sample spectra of signals x and y and $\langle\rangle$ denotes the average over the ensemble of the spectra samples. Bicoherence squared $b^2(f_1, f_2)$ is then analogously defined as the magnitude squared bicoherence $|B(f_1, f_2)|^2$ normalized by the auto-spectral density of the frequency-sum mode $\langle|Y(f_1 + f_2)|^2\rangle$ and the power spectral density of the component frequency modes $\langle|X(f_1)X(f_2)|^2\rangle$

$$b^2(f_1, f_2) = \frac{|B(f_1, f_2)|^2}{\langle|Y(f_1 + f_2)|^2\rangle\langle|X(f_1)X(f_2)|^2\rangle} \tag{6.1}$$

The normalization results in $b(f_1, f_2)^2$ always being in the range $< 0, 1 >$ and also means that the squared bicoherence expresses the fraction of the power at frequency $f_1 + f_2$ due to the three-wave coupling [53]. The frequencies can be in principal negative, which corresponds to a complex conjugate of the spectra. While this means that one three-wave interaction will be represented by several possible combinations of positive and negative frequencies, any difference in the bicoherence or bispectrum between these different combinations may point to an asymmetry in the time domain, e.g. a preferred flow of the energy.

The bicoherence is symmetrical with respect to the $f_1 = f_2$ line, i.e. the axis of the first and third quadrant. Furthermore, the bicoherence for sum frequency $f_1 + f_2$ can be only calculated for signals with a finite Nyquist frequency f_{Nyq}. Therefore, the squared bicoherence is by convention displayed only for frequencies $f_1 \geq 0$, $f_2 < f_1$ and $|f_1 + f_2| < f_{Nyq}$. If the two frequency modes f_1 and f_2 are bi-coherent with the mode $f_1 + f_2$ there will be a high level of bicoherence displayed at the points $[f_1, f_2]$, $[f_1 + f_2, -f_1]$ and $[f_1 + f_2, -f_2]$.

For the easier interpretation of the level of bi-coherent power for a given frequency sum mode the summed squared bicoherence at frequency f is defined as the average squared bicoherence over all the component frequencies as $\bar{b}^2(f) = \frac{1}{N_f} \sum\limits_{f=f_1+f_2} b^2(f_1, f_2)$ where N_f is the number of terms in the sum for the given sum frequency f.

Due to the cLCO frequency being in the order of $\sim$ 1kHz conventional spectra estimation via a short-time Fourier transform was not a viable option as such approach requires an ensemble of several ms in order to estimate the signal spectra with such a precision. This could not be done as the probe head changes its radial position significantly within that time scale. Therefore, the spectra were estimated using wavelet decomposition as outlined in [54] which decomposes the signals into the basis of Gaussian-window-delimited complex exponentials $\exp(-2\pi f(t - t_0)^2 + i2\pi ft)$ instead of the simple complex exponentials $\exp(i2\pi ft)$ used in the conventional Fourier transform. This method provides the spectra estimated at a very high frequency and time precision. Additionally, the wavelet decomposition can resolve even intermittent high frequency events due to the small Gaussian window for high frequencies which is especially of great use for the analysis of plasma turbulence as was argued in [54].

The result of calculating the squared summed auto-bicoherence (i.e. the signal served as both x and y) over 5 ms windows of the plasma potential measured by `BPP2` in discharge #13925 during the reciprocation trajectory of the probe head is shown in Figure 6.7. Clear bicoherence of the plasma potential at the $\sim$ 5 kHz cLCO frequency is observed only when the probe head is inside the LCFS. This indicates that nonlinear transfer of energy to or from the cLCO frequency scale is happening only inside the LCFS. This justifies the selection of the time-span to be analyzed in section 6.2 to the time when the probe head was inside the LCFS.

A detailed view of the calculated squared bicoherence in the timepsan 1170-1180 ms in that discharge is shown in Figure 6.8 where the quite strong bicoherence along the lines $f_2 \sim 5$ kHz $f_2 \sim -5$ kHz and $f_2 \sim 5\text{kHz} - f_1$ indicates that a broad range of higher frequencies is interacting with the cLCO frequency $\sim$ 5 kHz. In particular, the bicoherence on the horizontal lines suggests that the highest level of interaction is with frequencies in the range 30-150 kHz and extends to at least 250 kHz. This higher frequency range is also faintly visible in Figure 6.7. This observation is in line with the

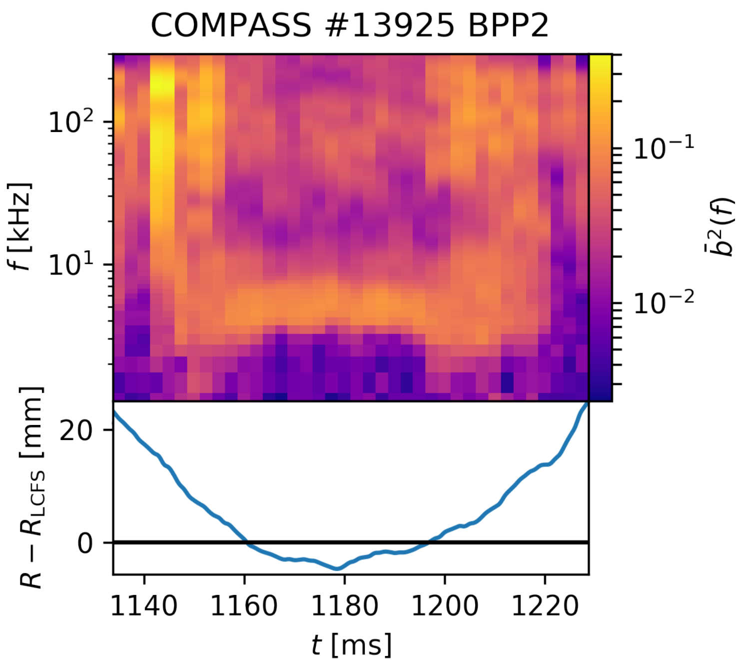

Figure 6.7: Summed squared bicoherence $\bar{b}^2(f)$ evolution along the reciprocation trajectory shown in the bottom plot as the radial distance of the probe head R to the radial location of the LCFS. The bicoherence was calculated over 5 ms windows to obtain good statistics. It is evident that high summed squared bicoherence at the frequency ~ 5 kHz is present only when the probe is inside the LCFS.

hypothesis that higher frequency scales corresponding to turbulent structures interact with lower frequency scales of zonal flows.

A similar analysis was performed for discharge #13963 during the slow L-H transition. The bicoherence was calculated over 2 ms windows in order to obtain reasonable statistics while accounting for the cLCO frequency slowly decreasing towards the H-mode. The evolution of summed squared bicoherence is shown in Figure 6.9. The cLCO frequency visibly decreases as the H-mode approaches. The interaction with higher-frequency scales appears to become stronger as well. The last peak in the H_α signal corresponds to a very different bicoherence signature, which suggests that is differs from the cLCO and is an actual ELM.

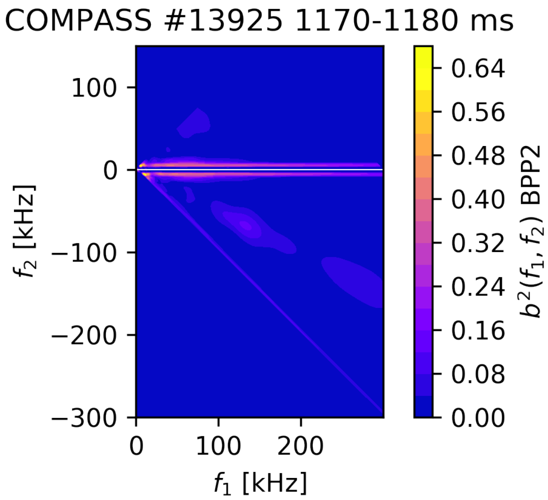

Figure 6.8: Squared bicoherence $b^2(f_1, f_2)$ calculated in the timespan 1170-1180 ms from the plasma potential measured by BPP2 in discharge #13925. There is a clear interaction of the ~ 5 kHz cLCO frequency with a broad range of higher frequencies, particularly in the range 30-150 kHz.

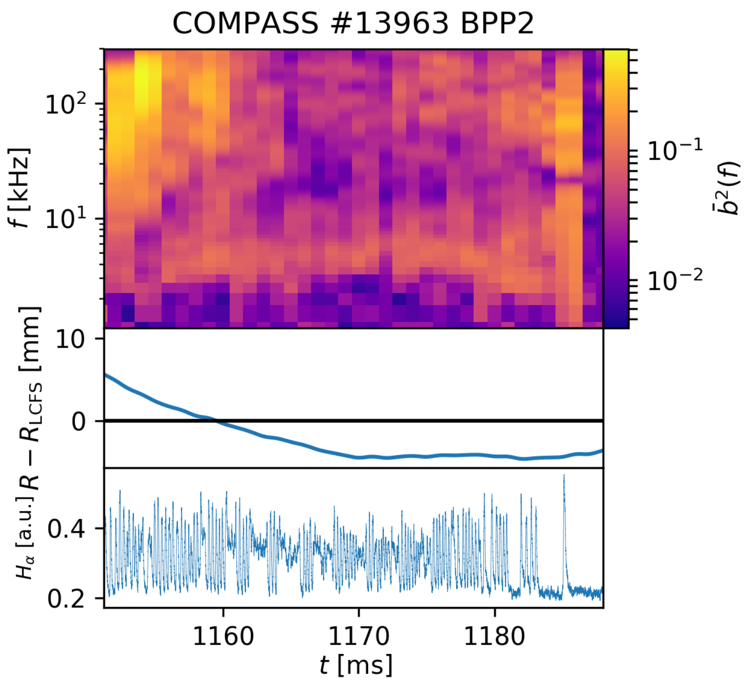

Figure 6.9: Summed squared bicoherence $\bar{b}^2(f)$ evolution in discharge #13963 along the reciprocation trajectory shown in the second plot from the top as the radial distance of the probe head R to the radial location of the LCFS. The bottom plot shows the H_α signal as an indication of the L-H transition phase.

Chapter 7

Search for stationary zonal flow structures during deep reciprocations

The ability to measure the radial electric field E_r with high temporal and spatial accuracy of the original Reynolds stress probe head and its modified version described in subsection 3.2.3 and subsection 3.2.4, respectively, presented an opportunity to search for stationary structures on the radial E_r profile in the E_r well corresponding to stationary zonal flows as explained in section 2.3 and observed in JET [24]. However, the original Reynolds stress probe head could not penetrate deep enough inside the LCFS without significantly cooling and perturbing the plasma as was discussed in subsection 4.1.1. Therefore, the modified Reynolds stress probe head had to be used as it had at least some chance of success. Due to its construction and availability only at the end of the diploma thesis work in the experimental campaign `CC17.11` used also for cLCO investigation detailed in chapter 6, only a limited number of discharges had the necessary properties needed for this type of measurement. The discharges with cLCO oscillations proved to be of little use due to the strong modulation of the electric field by cLCO.

Some discharges from that campaign did not have cLCO while the probe head was deep enough inside the LCFS in order to observe the E_r well. Only the discharges with a stationary flat-top plasma current and density were considered. In such discharges usually there was an arc on `LP1` which mitigated the cLCO. However, it also perturbed the plasma enough to significantly change the E_r radial profiles from the inward reciprocation to the outward motion. Furthermore, saw-teeth crashes appear to also strongly module E_r in the well and prevented the observation of any stationary structures. This is illustrated Figure 7.1 where during the inwards reciprocation motion the E_r profile is modulated by cLCO up to $t \sim 1155\,\mathrm{ms}$. Once the probe passed far inside the LCFS an arc on `LP1` developed and the plasma conditions changed considerably as can be seen on the evolution of the H_α signal. During the outwards reciprocation the E_r profile is significantly different and is modulated by saw-teeth crashes. The radial location of $E_r = 0\,\mathrm{kV/m}$ agrees well with the radial location of the LCFS estimated from the radial location of the plasma potential maximum. Altogether, this demonstrates that this probe head is capable of measuring the radial profile of E_r including the E_r well with a high radial resolution as well as the evolution of the radial profile which would enable the identification of stationary structures. However, the discharge scenario would have to be better optimized for such measurements.

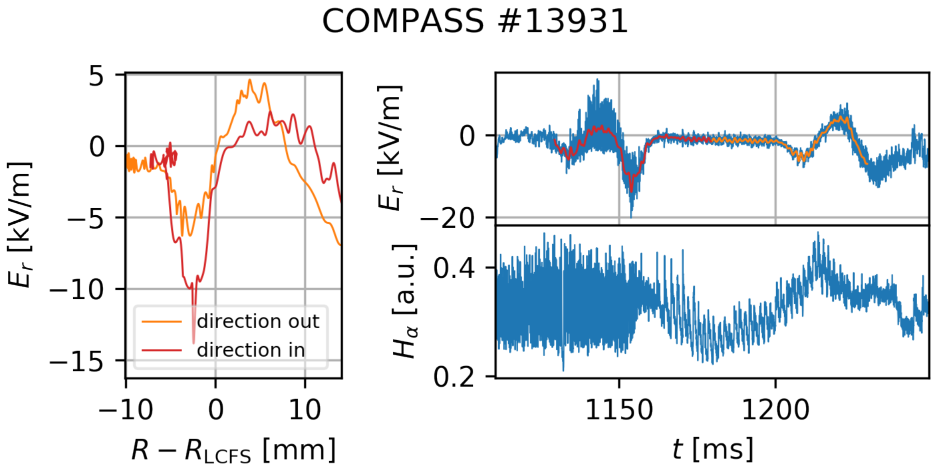

Figure 7.1: Radial profile of the radial electric field E_r measured deep inside the LCFS (the radial distance from the LCFS $R - R_{\mathrm{LCFS}}$ is shown on the x-axis) with ball-pen probes in COMPASS discharge #13931 (left plot). The **in**wards and **out**wards directions of the reciprocation motion are plotted in different colors to distinguish these different phases of measurement. The right two plots show the temporal evolution of $E_r(R,t)$ (measured at different radial locations along the reciprocation trajectory) and the H_α signal to illustrate the measurement of E_r in different phases of the discharge.

Therefore, future measurements aiming to search for such stationary structures will require a specially optimized scenario which will minimize the effect of saw-teeth crashes on E_r. The scenario developed for the Reynolds stress profiles measurements in L-mode showed that the saw-teeth intensity can be reduced by decreasing the plasma current to $I_{pl} \sim 150\,\mathrm{kA}$ and increasing the density to $n > 5 \times 10^{19}\,\mathrm{m}^{-3}$. However, that scenario was quite far from the L-H transition threshold and is unlikely to show any zonal flow structures. The target scenario will also have to be far enough from the L-H transition in order to prevent cLCO modulating E_r. Another promising change to the experimental setup might be the exclusion of the ion saturation current measurement. While this will mean that the local density will not be measured, it may limit the perturbation of the plasma by the probe head and prevent any degradation of the stationary conditions.

Conclusions

The two multi-pin Reynolds stress probe heads used in the scope of this thesis have proven to be a highly useful diagnostic for the investigation of the L-H transition and plasma turbulence in the edge plasma of the COMPASS tokamak. In particular, they enable simultaneous, local measurements of electric fields by both ball-pen and Langmuir probes, thereby enabling the investigation of the influence of the electron temperature fluctuations in associated physical quantities like the Reynolds stress, a key quantity for the investigation of zonal flow generation by turbulence. The geometry and setup of the probe heads as well as the possibilities of measuring electric fields with the two slightly different probe head configurations were described.

The newly tested 2 mm ball-pen probe used in these probe heads performs comparably with the conventional, larger ball-pen probes. In particular, the floating potential measured by the 2 mm ball-pen probe has the same relation to the plasma potential and electron temperature quantifiable by a low coefficient $\alpha_{\mathrm{BPP}} \approx 0.6$. Good agreement between the electron temperature calculated from the difference of potentials measured by neighboring ball-pen and Langmuir probes and the temperature measured by the Thomson scattering system has been found. However, the original Reynolds stress probe head was observed to significantly cool the plasma when reciprocating beyond the last closed flux surface, likely because of out-gassing and impurity release due to the less pure type of boron nitride used for the bulk of the probe head.

The twin-floor probe head design enables fast, simultaneous measurements of the radial electric field with both ball-pen and Langmuir probes. Good agreement has been found between this probe-difference method and the approximate radial electric field calculated from the profile of the plasma potential. The fluctuation levels of the radial electric fields obtained by the probe-difference method are nearly the same for ball-pen and Langmuir probes. However, for the poloidal electric field the fluctuation level is significantly higher for Langmuir probes and the difference increases further inside the plasma.

Radial profiles of the Reynolds stress simultaneously measured with ball-pen and Langmuir probes were obtained with the original Reynolds stress probe head. The measured Reynolds stress profiles are significantly different for either probe type, although they have some similarity in their general shape. The Reynolds stress obtained with ball-pen probes is generally higher than from Langmuir probes. The spectral composition of the Reynolds stress suggests that the lower or even negative values for Langmuir probes originate from negative contributions of higher frequency ($f > 100$ kHz) fluctuations which may be related to temperature fluctuations. This is further supported by separating the Reynolds stress from Langmuir probes into terms containing combinations of plasma potential and temperature fluctuations. The Reynolds stress profiles measured with Langmuir probes have been found to be in good qualitative agreement with similar measurements on the TEXTOR, TJ-II, ISTTOK and IR-T1 devices.

The modified Reynolds stress probe head was used to investigate $3-5$ kHz oscillations often appearing during the L-H transition in the COMPASS tokamak. These oscillations were suspected of being limit cycle oscillations (LCO) between states of reduced and high turbulence due to the predator-prey-like interaction of zonal flows and turbulence. The measurements were performed in specifically developed discharge scenarios with these candidate limit cycle oscillations (cLCO) either sustained during the whole plasma current flat-top at a stable frequency or during a slowly progressing L-H transition. The different type of purer boron nitride used for this modified probe head proved to be a better choice, because the insertion of the probe head up to 5 mm inside the last closed flux surface appeared to have little effect on the plasma and the L-H transition.

These ~ 5 kHz cLCO oscillations were observed to modulate the intensity of density fluctuations related to the turbulence intensity and also the radial electric field related to the poloidal flows decorrelating turbulent structures. The modulation of these quantities was measured using the probe head while it was inside the last close flux surface. The low-frequency cross-phase Hilbert analysis of the oscillations of the turbulence intensity and the strength of the radial electric field shows a $-\pi$ to $-\frac{\pi}{2}$ phase delay, i.e. the turbulence intensity rises after the radial electric field strength decreases. This is similar to type-J LCO observed on the HL-2A tokamak where the electric field was observed to decrease due to the plasma pressure gradient decreasing, after which the turbulence intensity began to rise. An observed edge-localized mode (ELM) appears to have similar low-frequency dynamics, but the high-frequency patterns of density and radial electric field fluctuations, namely a precursor phase, suggest that it is different than the cLCO dynamics.

The identification of the cLCO as type-J LCO is further supported by the analysis of conditionally-averaged waveforms of several quantities measured by the probe head. The conditional average method enabled a detailed analysis of the temporal evolution of key quantities on a broader range of time scales during the cLCO cycle, which the low-frequency cross-phase analysis could not resolve. The poloidal velocity appears to be strongly correlated with the radial pressure gradient and decreases in response to the flattening of the pressure profile. Once the pressure profile flattens below a certain level the turbulence intensity quickly rises and the pressure profile and the velocity shear begin to rapidly decrease. The evolution of the density, electron temperature and pressure profiles suggests that the core plasma is ejected into the edge as the turbulence intensity approaches its maximum level. These profiles begin the recover as the turbulence intensity begins to decrease. The poloidal velocity shear likely slowly increases at this stage, but large errors prevent a clear interpretation. Once the turbulence intensity and the pressure profile have nearly reached the levels at the beginning of the cycle, the velocity shear begins to quickly recover to the values at the start of the cycle. Unfortunately, the role of the Reynolds stress force is not clear, because the large error of its estimate is comparable to its estimated value. There are hints that it may be actually slowing down the flows in the late stages of the turbulence intensity rise. Altogether, the oscillations appear to be mostly driven by the modulation of the pressure gradient. However, some influence of the Reynolds stress force cannot be ruled out. A more sophisticated analysis based on fitting values in a 2D radial location and oscillation phase space may offer a better understanding.

Wavelet-based bicoherence analysis was used to detect non-linear interaction and possible energy transfer between different frequency scales in the plasma potential during the observed oscillations. Clear bicoherence between the cLCO frequency and a broad range of presumably turbulent fluctuations 50-250 kHz was observed only when the probe head was inside the last close flux surface. The bicoherence analysis was also able to resolve the changing frequency of the cLCO during a slow L-H transition and showed a significantly different bicoherence signature for an ELM event preceding an ELM-free H-mode, during which no bicoherence was observed. This further suggests that these cLCO are not ELMs.

While the probe head has demonstrated the capability of measuring deep enough inside the last closed flux surface to observe the radial electric field well, stationary zonal flow structures on the profile of the radial electric field could not be conclusively observed. This was in part due to the discharge scenario not being sufficiently optimized for this type of measurement as cLCO and saw-teeth modulated the electric field too much, and in part by the arcs on the ion saturation current measurement changing the plasma conditions. In future experiments the optimization of the scenario for better saw-teeth mitigation and exclusion of the ion saturation current measurement may enable a better investigation of such stationary structures.

All the data analysis presented in this thesis was performed by the author. The design of the probe heads and their connection and integration into the data acquisition system was done in collaboration with Mgr. Jiří Adámek, Ph.D. The cLCO investigation scenario development and measurement was performed in collaboration with Mgr. Jakub Seidl, Ph.D.

Large parts of the sections of this thesis on the design of the original Reynolds stress probe head (subsection 3.2.3), its measurement properties (chapter 4) and the Reynolds stress profiles obtained with it and their analysis (chapter 5) have been used in an article submitted to the journal Review of Scientific Instruments of the American Institute of Physics with the author of this thesis as the first author. The cLCO results and Reynolds stress profile measurements will be presented by the author as a poster presentation at the 44^{th} European Physical Society Conference on Plasma Physics.

Index

Bibliography

[1] J. Wesson. *Tokamaks*. 4th ed. New York: Oxford University Press, 2011.

[2] F. F. Chen. *Introduction to Plasma Physics and Controlled Fusion*. 3rd ed. Springer International Publishing Switzerland: Springer, 2016. ISBN: 978-3-319-22308-7.

[3] K. Miyamoto. *Plasma Physics for Controlled Fusion (Springer Series on Atomic, Optical, and Plasma Physics)*. Springer, 2016. ISBN: 978-3-662-49781-4.

[4] K. Crombe, ed. *12th Carolus Magnus Summer School on Plasma and Fusion Energy Physics*. Vol. 298. Schriften des Forschungszentrums Jülich Reihe Energie & Umwelt / Energy & Environment. Online-Publikation. Jülich: Forschungszentrum Jülich GmbH Zentralbibliothek, Verlag, 2015, 468 pp. ISBN: 978-3-95806-107-1. URL: `http://juser.fz-juelich.de/record/283582`.

[5] M. Kikuchi and K. Lackner. *Fusion physics*. Vienna: International Atomic Energy Agency, 2012. ISBN: 978-920-1304-100.

[6] M. Kikuchi. *Frontiers in Fusion Research: Physics and Fusion*. Springer, 2011. ISBN: 978-1-84996-411-1.

[7] K. Ikeda. "Progress in the ITER Physics Basis". In: *Nuclear Fusion* 47.6 (2007). URL: `http://stacks.iop.org/0029-5515/47/i=6/a=E01`.

[8] T. S. Pedersen et al. "Confirmation of the topology of the Wendelstein 7-X magnetic field to better than 1:100,000". eng. In: *Nature Communications* 7, 13493 (2016). ISSN: 2041-1723. DOI: `10.1038/ncomms13493`.

[9] EFDA. *Fusion Electricity. A roadmap to the realisation of fusion energy.* 2013.

[10] F. Wagner et al. "Regime of Improved Confinement and High Beta in Neutral-Beam-Heated Divertor Discharges of the ASDEX Tokamak". In: *Phys. Rev. Lett.* 49 (19 Nov. 1982), pp. 1408–1412. DOI: `10.1103/PhysRevLett.49.1408`. URL: `http://link.aps.org/doi/10.1103/PhysRevLett.49.1408`.

[11] ASDEX Team. "The H-Mode of ASDEX". In: *Nuclear Fusion* 29.11 (1989), p. 1959. URL: `http://stacks.iop.org/0029-5515/29/i=11/a=010`.

[12] R. Pánek et al. "Status of the COMPASS tokamak and characterization of the first H-mode". In: *Plasma Physics and Controlled Fusion* 58.1 (2016), p. 014015. URL: `http://stacks.iop.org/0741-3335/58/i=1/a=014015`.

[13] G. Verdoolaege and J-M. Noterdaeme. "Robust scaling in fusion science: case study for the L-H power threshold". In: *Nuclear Fusion* 55.11 (2015), p. 113019. URL: `http://stacks.iop.org/0029-5515/55/i=11/a=113019`.

[14] A. Dinklage et al., eds. *Plasma Physics: Confinement, Transport and Collective Effects*. Berlin Heidelberg: Springer-Verlag, 2005. ISBN: 978-3-540-25274-0. DOI: `10.1007/b103882`. URL: `https://doi.org/10.1007/b103882`.

[15] P. Kulhánek. *Úvod do teorie plazmatu*. Vyd. 1. Praha: AGA, 2011. ISBN: 978-80-904582-2-2.

[16] O. E. Garcia et al. "Turbulence and intermittent transport at the boundary of magnetized plasmas". In: *Physics of Plasmas* 12.6 (2005), p. 062309. DOI: `10.1063/1.1925617`. URL: `http://dx.doi.org/10.1063/1.1925617`.

[17] P. H. Diamond, S.-I. Itoh, and K. Itoh. *Modern Plasma Physics: Volume 1, Physical Kinetics of Turbulent Plasmas*. Cambridge University Press, 2010. ISBN: 9781139489362. URL: `https://books.google.cz/books?id=RZvHxqcpvSUC`.

[18] J. P. Gunn et al. "Evidence for a poloidally localized enhancement of radial transport in the scrape-off layer of the Tore Supra tokamak". In: *Journal of Nuclear Materials* 363–365 (2007). Plasma-Surface Interactions-17, pp. 484–490. ISSN: 0022-3115. DOI: `http://dx.doi.org/10.1016/j.jnucmat.2007.01.195`. URL: `http://www.sciencedirect.com/science/article/pii/S0022311507000943`.

[19] Justin R Angus, Maxim V Umansky, and Sergei I Krasheninnikov. "Effect of drift waves on plasma blob dynamics". In: *Physical review letters* 108.21 (2012), p. 215002.

[20] D. A. D'Ippolito, J. R. Myra, and S. J. Zweben. "Convective transport by intermittent blob-filaments: Comparison of theory and experiment". In: *Physics of Plasmas* 18.6 (2011), p. 060501. DOI: `10.1063/1.3594609`. URL: `http://dx.doi.org/10.1063/1.3594609`.

[21] H. Biglari, P. H. Diamond, and P. W. Terry. "Influence of sheared poloidal rotation on edge turbulence". In: *Physics of Fluids B Plasma Physics* 2 (1990). DOI: `10.1063/1.859529`.

[22] P. H. Diamond et al. "Zonal flows in plasma—a review". In: *Plasma Physics and Controlled Fusion* 47.5 (2005), R35. URL: `http://stacks.iop.org/0741-3335/47/i=5/a=R01`.

[23] A. Fujisawa. "A review of zonal flow experiments". In: *Nuclear Fusion* 49.1 (2009), p. 013001. URL: http://stacks.iop.org/0029-5515/49/i=1/a=013001.

[24] J. C. Hillesheim et al. "Stationary Zonal Flows during the Formation of the Edge Transport Barrier in the JET Tokamak". In: *Phys. Rev. Lett.* 116 (6 Feb. 2016), p. 065002. DOI: 10.1103/PhysRevLett.116.065002. URL: https://link.aps.org/doi/10.1103/PhysRevLett.116.065002.

[25] P. C. Stangeby. *The Plasma Boundary of Magnetic Fusion Devices*. Series in Plasma Physics and Fluid Dynamics. Taylor & Francis, 2000. ISBN: 9780750305594. URL: https://books.google.cz/books?id=qOliQgAACAAJ.

[26] J. Adámek et al. "Profile measurements of the electron temperature on the ASDEX Upgrade, COMPASS, and ISTTOK tokamak using Thomson scattering, triple, and ball-pen probes". In: *Review of Scientific Instruments* 87.4, 043510 (2016). DOI: http://dx.doi.org/10.1063/1.4945797. URL: http://scitation.aip.org/content/aip/journal/rsi/87/4/10.1063/1.4945797.

[27] P. H. Diamond and Y.-B. Kim. "Theory of mean poloidal flow generation by turbulence". In: *Physics of Fluids B: Plasma Physics* 3.7 (1991), pp. 1626–1633.

[28] M. Kikuchi and M. Azumi. *Frontiers in Fusion Research II: Introduction to Modern Tokamak Physics*. Springer International Publishing, 2015. ISBN: 9783319189055. URL: https://books.google.cz/books?id=AHyBCgAAQBAJ.

[29] E.-J. Kim and P. H. Diamond. "Zonal Flows and Transient Dynamics of the L-H Transition". In: *Phys. Rev. Lett.* 90 (18 May 2003), p. 185006. DOI: 10.1103/PhysRevLett.90.185006. URL: http://link.aps.org/doi/10.1103/PhysRevLett.90.185006.

[30] Y. Xu et al. "Dynamics of low–intermediate–high-confinement transitions in the HL-2A tokamak". In: *Plasma Physics and Controlled Fusion* 57.1 (2015), p. 014028. URL: http://stacks.iop.org/0741-3335/57/i=1/a=014028.

[31] G. Birkenmeier et al. "Magnetic structure and frequency scaling of limit-cycle oscillations close to L- to H-mode transitions". In: *Nuclear Fusion* 56.8 (2016), p. 086009. URL: http://stacks.iop.org/0029-5515/56/i=8/a=086009.

[32] J. Cheng et al. "Low–intermediate–high confinement transition in HL-2A tokamak plasmas". In: *Nuclear Fusion* 54.11 (2014-11-01). ISSN: 0029-5515. DOI: 10.1088/0029-5515/54/11/114004. URL: http://stacks.iop.org/0029-5515/54/i=11/a=114004?key=crossref.f37b6a1d0052f5eda573db228e502124.

[33] V. Weinzettl et al. “Overview of the COMPASS diagnostics”. In: *Fusion Engineering and Design* 86.6-8 (2011), pp. 1227–1231. ISSN: 09203796. URL: http://linkinghub.elsevier.com/retrieve/pii/S0920379610005594.

[34] C. H. Skinner et al. “Tritium diagnostics by Balmer-alpha emission”. In: *Plasma Physics Laboratory, Princeton University, Technical report* (1993).

[35] M. Hron et al. “Overview of the COMPASS CODAC system”. In: *Fusion Engineering and Design* 89.3 (2014), pp. 177–185. ISSN: 09203796. URL: http://linkinghub.elsevier.com/retrieve/pii/S0920379613006613.

[36] J. Urban et al. “Integrated data acquisition, storage, retrieval and processing using the COMPASS DataBase (CDB)”. In: *Fusion Engineering and Design* 89.5 (2014), pp. 712–716.

[37] F. Janky et al. “Upgrade of the COMPASS tokamak real-time control system”. In: *Fusion Engineering and Design* 89.3 (2014). Design and implementation of real-time systems for magnetic confined fusion devices, pp. 186–194. ISSN: 0920-3796. DOI: http://dx.doi.org/10.1016/j.fusengdes.2013.12.042. URL: http://www.sciencedirect.com/science/article/pii/S0920379613007564.

[38] R. L. Merlino. “Understanding Langmuir probe current-voltage characteristics”. In: *American Journal of Physics* 75.12 (2007), pp. 1078–1085. DOI: 10.1119/1.2772282. eprint: http://dx.doi.org/10.1119/1.2772282. URL: http://dx.doi.org/10.1119/1.2772282.

[39] J. Adámek et al. “A novel approach to direct measurement of the plasma potential”. English. In: *Czechoslovak Journal of Physics* 54.3 (2004), pp. C95–C99. ISSN: 0011-4626. DOI: 10.1007/BF03166386. URL: http://dx.doi.org/10.1007/BF03166386.

[40] J. Adámek et al. “Direct measurements of the plasma potential in ELMy H-mode plasma with ball-pen probes on ASDEX Upgrade tokamak”. In: *Journal of Nuclear Materials* 390–391 (2009), pp. 1114–1117. ISSN: 0022-3115. URL: http://dx.doi.org/10.1016/j.jnucmat.2009.01.286.

[41] S. Murphy-Sugrue et al. “Improved understanding of the ball-pen probe through particle-in-cell simulations”. In: *Plasma Physics and Controlled Fusion* 59.5 (2017), p. 055007. URL: http://stacks.iop.org/0741-3335/59/i=5/a=055007.

[42] C. Silva et al. “Comparison of fluctuations properties measured by Langmuir and ball-pen probes in the ISTTOK boundary plasma”. In: *Plasma Physics and Controlled Fusion* 57.2 (2015), p. 025003. URL: http://stacks.iop.org/0741-3335/57/i=2/a=025003.

[43] J. Adámek et al. “Fast measurements of the electron temperature and parallel heat flux in ELMy H-mode on the COMPASS tokamak”. In: *Nuclear Fusion* 57.2 (2017), p. 022010. URL: http://stacks.iop.org/0029-5515/57/i=2/a=022010.

[44] Y. Xu et al. “Measurements of Reynolds stress and turbulent transport in the plasma boundary during the static dynamic ergodic divertor operation on TEXTOR”. In: *Journal of Nuclear Materials* 363–365 (2007). Plasma-Surface Interactions-17, pp. 718–722. ISSN: 0022-3115. URL: http://doi.org/10.1016/j.jnucmat.2007.01.059.

[45] M. Lafouti and M. Ghoranneviss. “Bias Effects on the Reynolds Stress Using the Multi-Purpose Probe in IR-T1 Tokamak”. In: *Chinese Physics Letters* 33.1 (2016), p. 015203. URL: http://stacks.iop.org/0256-307X/33/i=1/a=015203.

[46] C. Silva et al. “Reciprocating probe measurements of ELM filaments on JET”. In: *Plasma Physics and Controlled Fusion* 51.10 (2009), p. 105001. URL: http://stacks.iop.org/0741-3335/51/i=10/a=105001.

[47] X. Guosheng and W. Baonian. “Measurement of Zonal Flows in a Tokamak Using Langmuir Probe Array”. In: *Plasma Science and Technology* 8.1 (2006), p. 10. URL: http://stacks.iop.org/1009-0630/8/i=1/a=3.

[48] C. Hidalgo et al. “Generation of sheared poloidal flows via Reynolds stress and transport barrier physics”. In: *Plasma Physics and Controlled Fusion* 42 (2000), A153. URL: http://stacks.iop.org/0741-3335/42/i=5A/a=316.

[49] H. W. Müller et al. “Latest investigations on fluctuations, ELM filaments and turbulent transport in the SOL of ASDEX Upgrade”. In: *Nuclear Fusion* 51.7 (2011), p. 073023. URL: http://stacks.iop.org/0029-5515/51/i=7/a=073023.

[50] J. S. Bendat and A. G. Piersol. *Random Data: Analysis and Measurement Procedures*. 4th ed. Wiley, Feb. 2010. ISBN: 9780470248775.

[51] J. M. Beall, Y. C. Kim, and E. J. Powers. “Estimation of wavenumber and frequency spectra using fixed probe pairs”. In: *Journal of Applied Physics* 53.6 (1982), pp. 3933–3940. DOI: 10.1063/1.331279. eprint: http://dx.doi.org/10.1063/1.331279. URL: http://dx.doi.org/10.1063/1.331279.

[52] B. Everitt. *The Cambridge Dictionary of Statistics*. Cambridge, UK New York: Cambridge University Press, 2002. ISBN: 052181099X.

[53] Y. C. Kim and E. J. Powers. “Digital Bispectral Analysis and Its Applications to Nonlinear Wave Interactions”. In: *IEEE Transactions on Plasma Science* 7.2 (June 1979), pp. 120–131. ISSN: 0093-3813. DOI: 10.1109/TPS.1979.4317207.

[54] B. Ph. van Milligen et al. “Wavelet bicoherence: A new turbulence analysis tool”. In: *Physics of Plasmas* 2.8 (1995), pp. 3017–3032. DOI: http://dx.doi.org/10.1063/1.871199. URL: http://scitation.aip.org/content/aip/journal/pop/2/8/10.1063/1.871199.